

UNCLASSIFIED

Final Report

UNDAS-FR-2025

**Aerodynamics of Low Aspect Ratio
Wings at Low Reynolds Numbers With
Applications to Micro Air Vehicle Design
and Optimization**

Thomas J. Mueller and Gabriel E. Torres
*Hessert Center for Aerospace Research
Department of Aerospace and Mechanical Engineering
University of Notre Dame
Notre Dame, Indiana*

Prepared for
Naval Research Laboratory
Under Contract No.: N00173-98-C-2025

DISTRIBUTION STATEMENT A
Approved for Public Release
Distribution Unlimited

November 2001



University of Notre Dame
Hessert Center for Aerospace Research
Department of Aerospace and
Mechanical Engineering
Notre Dame, Indiana 46556

UNCLASSIFIED

20011221 033

REPORT DOCUMENTATION PAGE

Form Approved
OMB No. 0704-0188

The public reporting burden for this collection of information is estimated to average 1 hour per response, including the time for reviewing instructions, searching existing data sources, gathering and maintaining the data needed, and completing and reviewing the collection of information. Send comments regarding this burden estimate or any other aspect of this collection of information, including suggestions for reducing the burden, to Department of Defense, Washington Headquarters Services, Directorate for Information Operations and Reports (0704-0188), 1215 Jefferson Davis Highway, Suite 1204, Arlington, VA 22202-4302. Respondents should be aware that notwithstanding any other provision of law, no person shall be subject to any penalty for failing to comply with a collection of information if it does not display a currently valid OMB control number.

PLEASE DO NOT RETURN YOUR FORM TO THE ABOVE ADDRESS.

1. REPORT DATE (DD-MM-YYYY) 30-11-2001		2. REPORT TYPE Final Contractor Report		3. DATES COVERED (From - To) 20 May 1998 - 30 September 2001	
4. TITLE AND SUBTITLE Aerodynamics of Low Aspect Ratio Wings at Low Reynolds Numbers With Applications to Micro Air Vehicle Design and Optimization				5a. CONTRACT NUMBER N00173-98-C-2025	
				5b. GRANT NUMBER	
				5c. PROGRAM ELEMENT NUMBER	
				5d. PROJECT NUMBER 57-1005-58	
6. AUTHOR(S) Thomas J. Mueller and Gabriel E. Torres				5e. TASK NUMBER	
				5f. WORK UNIT NUMBER	
7. PERFORMING ORGANIZATION NAME(S) AND ADDRESS(ES) University of Notre Dame Office of Research The Graduate School 602 Grace Hall Notre Dame, IN 46556				8. PERFORMING ORGANIZATION REPORT NUMBER UNDAS-FR-2025	
9. SPONSORING/MONITORING AGENCY NAME(S) AND ADDRESS(ES) Richard J. Foch; COR/TM Naval Research Observatory; Code 5712 4555 Overlook Ave. S.W. Washington, D.C. 20375-5320				10. SPONSOR/MONITOR'S ACRONYM(S) NRL	
				11. SPONSOR/MONITOR'S REPORT NUMBER(S)	
12. DISTRIBUTION/AVAILABILITY STATEMENT Unclassified and Unlimited					
13. SUPPLEMENTARY NOTES					
14. ABSTRACT The recent interest in the development of small UAVs and micro air vehicles has revealed a need for a more thorough understanding of the aerodynamics of small airplanes flying at low speeds. In response to this need, the present work provides a comprehensive study of the lift, drag, and pitching moment characteristics of wings of low aspect ratio operating at low Reynolds numbers. Wind tunnel tests of wings with aspect ratios between 0.5 and 2.0 and with four distinct wing planforms have been conducted at chord-Reynolds numbers in the range of 70,000 to 200,000. In addition, the effect of leading edge shape and fuselage bodies has been studied. As an example of an application of this wind tunnel data, the experimental results are used as part of an aerodynamic analysis procedure. This procedure is incorporated into a genetic algorithm optimization program that generates optimum MAV configurations given certain requirements and constraints. Results obtained by use of this optimization procedure have revealed that useful and accurate design-optimization tools can be developed based on the experimental data presented within this report.					
15. SUBJECT TERMS Micro air vehicle, micro aerial vehicle, MAV, small unmanned aerial vehicle, UAV, low aspect ratio wing, low Reynolds number, flat-plate wings, aerodynamic measurements, finite wings, design and optimization.					
16. SECURITY CLASSIFICATION OF:			17. LIMITATION OF ABSTRACT UU	18. NUMBER OF PAGES 125	19a. NAME OF RESPONSIBLE PERSON Thomas J. Mueller
a. REPORT Unclassified	b. ABSTRACT Unclassified	c. THIS PAGE Unclassified			19b. TELEPHONE NUMBER (Include area code) (219) 631-7073

Abstract

The recent interest in the development of small UAVs and micro air vehicles has revealed a need for a more thorough understanding of the aerodynamics of small airplanes flying at low speeds. In response to this need, the present work provides a comprehensive study of the lift, drag, and pitching moment characteristics of wings of low aspect ratio operating at low Reynolds numbers. Wind tunnel tests of wings with aspect ratios between 0.5 and 2.0 and with four distinct wing planforms have been conducted at chord-Reynolds numbers in the range of 70,000 to 200,000. In addition, the effect of leading edge shape and fuselage bodies has been studied.

As an example of an application of this wind tunnel data, the experimental results are used as part of an aerodynamic analysis procedure. This procedure is incorporated into a genetic algorithm optimization program that generates optimum MAV configurations given certain requirements and constraints. Results obtained by use of this optimization procedure have revealed that useful and accurate design-optimization tools can be developed based on the experimental data presented within this report.

Acknowledgments

This research was sponsored by the U. S. Navy, Naval Research Laboratory, Washington, D. C. under Contract No. N00173-98-C-2025 and the Department of Aerospace and Mechanical Engineering at the University of Notre Dame. The authors would like to thank Mr. Joel Preston and Mr. Michael Swadener for their invaluable assistance in supporting the experimental facilities and electronic components used in this work.

Contents

Abstract	iii
Acknowledgments	iv
List of Figures	viii
List of Symbols	xii
Chapter 1. Introduction	1
1.1 Motivation for Research: Small UAVs and MAVs	1
1.2 A Short Discussion of LAR Wings at Low Re	2
1.3 Scope of Present Work	3
1.3.1 Aerodynamic Data and Analysis	3
1.3.2 Optimization Code and Analysis Procedure	3
Chapter 2. Experimental Setup	4
2.1 Wing Models	4
2.2 Wind Tunnel	7
2.3 Force Balance and Sting Balance	7
2.3.1 Platform Force Balance	7
2.3.2 Five-Component Sting Balance	9
2.4 Signal Conditioning and Data Acquisition	10
2.5 Experimental Procedures	10
2.6 Uncertainty	11
Chapter 3. Analysis of Experimental Data	13
3.1 Discussion of Aerodynamic Results	13
3.1.1 Lift Performance Related to Tip Vortices	14
3.2 Maximum Lift Coefficient and Stall Angle of Attack	17
3.3 Aerodynamic Center	19
3.3.1 Background	19

3.3.2	Methods for Calculating the Location of the Aerodynamic Center	19
3.3.3	Final Method Used for Calculating h_{AC}	23
3.3.4	Discussion of Aerodynamic Center Results	25
3.4	Effect of Reynolds Number	31
3.5	Effects of Camber	31
3.6	Effects of Leading Edge Shape	36
Chapter 4.	Design-Optimization Part I: Design Variables and Optimization Algorithm	39
4.1	Introduction to MAV Design-Optimization	39
4.2	Design Problem Statement	40
4.2.1	Summary of Design Optimization Problem	40
4.2.2	Detailed Mission Requirements	40
4.2.3	Restrictions	41
4.3	Design Variables, Design Parameters, and Aircraft States	42
4.3.1	Design Variables	42
4.3.2	Design Parameters	43
4.3.3	Aircraft States (Performance)	43
4.4	Optimization Problem	44
4.4.1	Statement of Optimization Problem	44
4.4.2	Design Variable Constraints	44
4.4.3	Genetic Algorithm	45
4.4.3.1	Summary of Genetic Algorithm	45
4.4.3.2	Penalty Functions	47
4.4.3.3	Statement of Optimization Problem in GA Form	48
4.5	Results and Discussion	49
4.5.1	Test of Genetic Algorithm Code	49
4.5.2	Preliminary Results: Problems With Discrete Variables	50
4.5.3	Results of Modified Optimization Problem	51
4.5.3.1	Design Variables of Optimum Design (Converged Solution)	51
4.6	Conclusions and Recommendations of MAV Optimization	54
Chapter 5.	Design-Optimization Part II: Aerodynamic Analysis	55
5.1	Interpolation of Aerodynamic Coefficients and Stall Angle Analysis	55
5.1.1	Determination of Lift and Drag Coefficients for Wing and Tail	56
5.1.2	Determination of Stall Angle for Wing and Tail	59
5.2	Drag Analysis and Cruise Speed	60
5.2.1	Total Drag Force	60
5.2.2	Thrust Force and Cruise Speed	62
5.3	Center of Gravity Analysis	64
5.4	Pitching Moment Analysis	66
5.4.1	Moment About the CG	66
5.4.2	Aerodynamic Center	68
5.4.3	Longitudinal Stability Analysis	70

5.5	Maximum Dimension and Penalty Functions	71
5.6	Conclusions for Aerodynamic Analysis Procedure	72
 Chapter 6. Overall Conclusions and Recommendations		73
 References		74
 Appendix A. Aerodynamic Results		76
A.1	Aerodynamic Results: Constant Aspect Ratio	76
A.2	Aerodynamic Results: Constant Wing Planform	98
 Appendix B. Components		111

List of Figures

1.1	Linear Lift of LAR Wings Due to Circulation	2
1.2	Nonlinear Lift of LAR Wings Due to Wingtip and Leading Edge Vortices . . .	3
2.1	Formation of the Zimmerman Planforms	4
2.2	Wing Planforms Used in Experiments	5
2.3	Leading Edge Geometry: 5-to-1 Elliptical L.E.	6
2.4	Leading Edge Geometry: 10° Tapered	6
2.5	Leading Edge Geometry: 20° Tapered	6
2.6	Fuselage Bodies	6
2.7	Schematic of the Low-Speed Wind Tunnel	7
2.8	Platform Force Balance	8
2.9	Mounting of Wing Models with Platform Force Balance	8
2.10	Aerotech Five-Component Sting Balance and Mounting Sleeve	9
2.11	Mounting of Wing Models with Sting Balance	9
2.12	Uncertainty in C_L , Rectangular Wing of $AR=1.00$, $Re=100,000$	11
2.13	Uncertainty in C_D , Rectangular Wing of $AR=1.00$, $Re=100,000$	12
2.14	Uncertainty in C_M , Rectangular Wing of $AR=1.00$, $Re=100,000$	12
3.1	Separation of Wingtip Vortices Schematic and Comparison with Flow Visual- ization of Three Planforms ($AR=1.0$, $Re \approx 70,000$, $\alpha=15^\circ$)	15
3.2	Flow Visualization of Wingtip Vortices ($AR=1.0$, $Re \approx 70,000$, $\alpha=15^\circ$) . .	16
3.3	Lift Curve Slope, C_{L_α} vs. $x_{\max \text{ span}}$ for $Re=100,000$	16
3.4	Lift Curve of Rectangular Wing, $AR=0.5$, $Re=100,000$	17
3.5	Lift Curve of Inverse Zimmerman Wing, $AR=0.5$, $Re=100,000$	17
3.6	$C_{L_{\max}}$ of Four Wing Planforms and All Aspect Ratios ($Re=100,000$)	18
3.7	Stall Angle of Four Wing Planforms and All Aspect Ratios ($Re=100,000$) . .	18
3.8	Aerodynamic Center Analysis	20
3.9	Calculation of h_{AC} using Eqns. 3.3 and 3.5, $AR=1.0$ Rectangular Planform . .	21
3.10	Calculation of h_{AC} using Eqns. 3.3 and 3.9, $AR=1.0$ Rectangular Planform . .	22
3.11	Polynomial Approximations to C_N and C_M , $AR=1.0$ Rectangular Planform . .	23
3.12	Calculation of h_{AC} Using a Combination of Eqns. 3.3 and 3.9	24
3.13	h_{AC} vs. α , $AR=0.75$, $Re_c=140,000$	26
3.14	h_{AC} vs. α , $AR=1.00$, $Re_c=140,000$	26
3.15	h_{AC} vs. α , $AR=1.25$, $Re_c=140,000$	27
3.16	h_{AC} vs. α , $AR=1.50$, $Re_c=140,000$	27
3.17	h_{AC} vs. α , $AR=1.75$, $Re_c=140,000$	28

3.18	h_{AC} vs. α , $AR=2.00$, $Re_c=140,000$	28
3.19	h_{AC} vs. α , rectangular planform, $Re_c=140,000$	29
3.20	h_{AC} vs. α , Zimmerman planform, $Re_c=140,000$	29
3.21	h_{AC} vs. α , Inverse Zimmerman planform, $Re_c=140,000$	30
3.22	h_{AC} vs. α , Elliptical planform, $Re_c=140,000$	30
3.23	C_L vs. α , Rectangular Planform, Effect of Re	31
3.24	C_D vs. α , Rectangular Planform, Effect of Re	32
3.25	C_L vs. C_D , Rectangular Planform, Effect of Re	33
3.26	L/D vs. α , Rectangular Planform, Effect of Re	33
3.27	C_L vs. α , $AR=1.00$, Effect of Camber	34
3.28	C_L vs. C_D , $AR=1.00$, Effect of Camber	34
3.29	C_L vs. α , $AR=0.50$ and 2.00 , Effect of Camber	35
3.30	C_L vs. C_D , $AR=0.50$ and 2.00 , Effect of Camber	35
3.31	Leading Edge Geometries	36
3.32	Effect of Leading Edge Shape on C_N , Rectangular Planform $AR=2.0$	38
3.33	Effect of Leading Edge Shape on C_M , Rectangular Planform $AR=2.0$	38
4.1	Convergence History of GA Test Case	50
4.2	Convergence History of Genetic Algorithm	52
4.3	Top View of Optimized MAV Design	53
5.1	Analysis Procedure:	56
5.2	Example of Interpolation of C_L : Interpolate α	58
5.3	Example of Interpolation of C_L : Interpolate AR	58
5.4	Average Stall Angle of Attack for All Planforms	59
5.5	Analysis Procedure: Cruise Speed and Lift and Drag Forces	60
5.6	Increment of Drag due to Fuselage, Rectangular Wing of $AR=1.0$	61
5.7	Increment of Drag due to Fuselage, Rectangular Wing of $AR=1.5$	61
5.8	Increment of Drag due to Fuselage, Rectangular Wing of $AR=2.0$	62
5.9	Experimental Determination of Thrust of MAV Engine as a Function of V_∞	63
5.10	Analysis Procedure: Center of Gravity Analysis	64
5.11	Dimensions of MAV	65
5.12	Analysis Procedure: Pitching Moment About the CG	66
5.13	Pitching Moment About the Center of Gravity	67
5.14	Geometry Parameters for Ellipse-Based Wings	69
5.15	Analysis Procedure: Longitudinal Stability Requirement	70
5.16	Analysis Procedure: Pitching Moment About the CG	71
5.17	Dimensions of MAV	72
A.1	C_L vs. α , $AR=0.50$, $Re_c=100,000$	78
A.2	C_D vs. α , $AR=0.50$, $Re_c=100,000$	78
A.3	C_L vs. C_D , $AR=0.50$, $Re_c=100,000$	79
A.4	L/D vs. α , $AR=0.50$, $Re_c=100,000$	79
A.5	C_L vs. α , $AR=0.75$, $Re_c=100,000$	80
A.6	C_D vs. α , $AR=0.75$, $Re_c=100,000$	80

A.7	C_L vs. C_D , $AR=0.75$, $Re_c=100,000$	81
A.8	L/D vs. α , $AR=0.75$, $Re_c=100,000$	81
A.9	C_M vs. $=\alpha$, $AR=0.75$, $Re_c=140,000$	82
A.10	h_{AC} vs. α , $AR=0.75$, $Re_c=140,000$	82
A.11	C_L vs. α , $AR=1.00$, $Re_c=100,000$	83
A.12	C_D vs. α , $AR=1.00$, $Re_c=100,000$	83
A.13	C_L vs. C_D , $AR=1.00$, $Re_c=100,000$	84
A.14	L/D vs. α , $AR=1.00$, $Re_c=100,000$	84
A.15	C_M vs. $=\alpha$, $AR=1.00$, $Re_c=140,000$	85
A.16	h_{AC} vs. α , $AR=1.00$, $Re_c=140,000$	85
A.17	C_L vs. α , $AR=1.25$, $Re_c=100,000$	86
A.18	C_D vs. α , $AR=1.25$, $Re_c=100,000$	86
A.19	C_L vs. C_D , $AR=1.25$, $Re_c=100,000$	87
A.20	L/D vs. α , $AR=1.25$, $Re_c=100,000$	87
A.21	C_M vs. $=\alpha$, $AR=1.25$, $Re_c=140,000$	88
A.22	h_{AC} vs. α , $AR=1.25$, $Re_c=140,000$	88
A.23	C_L vs. α , $AR=1.50$, $Re_c=100,000$	89
A.24	C_D vs. α , $AR=1.50$, $Re_c=100,000$	89
A.25	C_L vs. C_D , $AR=1.50$, $Re_c=100,000$	90
A.26	L/D vs. α , $AR=1.50$, $Re_c=100,000$	90
A.27	C_M vs. $=\alpha$, $AR=1.50$, $Re_c=140,000$	91
A.28	h_{AC} vs. α , $AR=1.50$, $Re_c=140,000$	91
A.29	C_L vs. α , $AR=1.75$, $Re_c=100,000$	92
A.30	C_D vs. α , $AR=1.75$, $Re_c=100,000$	92
A.31	C_L vs. C_D , $AR=1.75$, $Re_c=100,000$	93
A.32	L/D vs. α , $AR=1.75$, $Re_c=100,000$	93
A.33	C_M vs. $=\alpha$, $AR=1.75$, $Re_c=140,000$	94
A.34	h_{AC} vs. α , $AR=1.75$, $Re_c=140,000$	94
A.35	C_L vs. α , $AR=2.00$, $Re_c=100,000$	95
A.36	C_D vs. α , $AR=2.00$, $Re_c=100,000$	95
A.37	C_L vs. C_D , $AR=2.00$, $Re_c=100,000$	96
A.38	L/D vs. α , $AR=2.00$, $Re_c=100,000$	96
A.39	C_M vs. $=\alpha$, $AR=2.00$, $Re_c=140,000$	97
A.40	h_{AC} vs. α , $AR=2.00$, $Re_c=140,000$	97
A.41	C_L vs. α , rectangular planform, $Re_c=100,000$	99
A.42	C_D vs. α , rectangular planform, $Re_c=100,000$	99
A.43	C_L vs. C_D , rectangular planform, $Re_c=100,000$	100
A.44	L/D vs. α , rectangular planform, $Re_c=100,000$	100
A.45	C_M vs. $=\alpha$, rectangular planform, $Re_c=140,000$	101
A.46	h_{AC} vs. α , rectangular planform, $Re_c=140,000$	101
A.47	C_L vs. α , Zimmerman planform, $Re_c=100,000$	102
A.48	C_D vs. α , Zimmerman planform, $Re_c=100,000$	102
A.49	C_L vs. C_D , Zimmerman planform, $Re_c=100,000$	103
A.50	L/D vs. α , Zimmerman planform, $Re_c=100,000$	103
A.51	C_M vs. $=\alpha$, Zimmerman planform, $Re_c=140,000$	104

A.52	h_{AC} vs. α , Zimmerman planform, $Re_c = 140,000$	104
A.53	C_L vs. α , inverse Zimmerman planform, $Re_c = 100,000$	105
A.54	C_D vs. α , inverse Zimmerman planform, $Re_c = 100,000$	105
A.55	C_L vs. C_D , inverse Zimmerman planform, $Re_c = 100,000$	106
A.56	L/D vs. α , inverse Zimmerman planform, $Re_c = 100,000$	106
A.57	C_M vs. $= \alpha$, inverse Zimmerman planform, $Re_c = 140,000$	107
A.58	h_{AC} vs. α , inverse Zimmerman planform, $Re_c = 140,000$	107
A.59	C_L vs. α , elliptical planform, $Re_c = 100,000$	108
A.60	C_D vs. α , elliptical planform, $Re_c = 100,000$	108
A.61	C_L vs. C_D , elliptical planform, $Re_c = 100,000$	109
A.62	L/D vs. α , elliptical planform, $Re_c = 100,000$	109
A.63	C_M vs. $= \alpha$, elliptical planform, $Re_c = 140,000$	110
A.64	h_{AC} vs. α , elliptical planform, $Re_c = 140,000$	110

List of Symbols

Symbols

English Symbols

a_1, a_2, a_3	Geometry parameters for ellipse-based wings
AR	Aspect ratio $\left(\frac{b^2}{S}\right)$
AR_T	Aspect ratio of tail
AR_W	Aspect ratio of wing
b	Span of wing or tail
b_p	Probability of mutation
C_D	Drag coefficient $\left(\frac{D}{\frac{1}{2}\rho V_\infty^2 S}\right)$
C_{DT}	Drag coefficient of tail
C_{DW}	Drag coefficient of wing
$C_{D_{total}}$	Total aircraft drag coefficient
C_L	Lift coefficient $\left(\frac{L}{\frac{1}{2}\rho V_\infty^2 S}\right)$
C_{L_α}	Lift-curve slope $\left(\frac{1}{\text{degree}}\right)$
$C_{L_{max}}$	Maximum lift coefficient
C_{LT}	Lift coefficient of tail
C_{LW}	Lift coefficient of wing
C_M	Pitching moment coefficient about the quarter-chord with respect to the MAC
C_{MAC}	Pitching moment coefficient about the aerodynamic center
$C_{M_{CG}}$	Pitching moment coefficient about the center of gravity
C_{M_α}	Slope of pitching moment coefficient curve
C_N	Normal force coefficient
C_{N_α}	Slope of normal force coefficient curve
C_{root}	Root chord of wing or tail
D	Drag force
D_T	Drag of tail
D_W	Drag of wing
D_{total}	Total aircraft drag force
D_{max}	Maximum dimension
d_{T_1}	Distance between tip of propeller and trailing edge of tail's tip chord
d_{T_2}	Distance between tip of propeller and trailing edge of tail's root chord
d_{W_1}	Distance between tip of propeller and trailing edge of wing's tip chord
d_{W_2}	Distance between tip of propeller and trailing edge of wing's root chord
$f(\underline{x})$	Function value for optimization
h_{CP}	Nondimensional location of center of pressure

h_{AC}	Nondimensional location of aerodynamic center
H_T	Diagonal of tail
H_W	Diagonal of wing
H_{W-T_1}	Distance between leading edge of wing's tip chord and trailing edge of tail's tip chord
H_{W-T_2}	Distance between leading edge of wing's tip chord and trailing edge of tail's root chord
i_T	Incidence angle of tail
i_W	Incidence angle of wing
L	Lift force
L_T	Lift of tail
L_W	Lift of wing
L_{total}	Total aircraft lift force
L/D	Lift to drag ratio
MAC or \bar{c}	Mean aerodynamic chord of wing or tail
m_1	Number of bits used in GA discretization of discrete variables
m_2	Number of bits used in GA discretization of continuous variables
M_{AC}	Pitching moment about the aerodynamic center
M_{CG}	Pitching moment about the center of gravity
$M_{\bar{c}/4}$	Pitching moment about the quarter-chord with respect to the MAC
$\frac{\partial M_{CG}}{\partial \alpha}$	Pitching moment derivative with respect to aircraft angle of attack
N	Number of design variables
N_P	Propeller normal force
N_{best}	Number of members of a generation kept automatically in mating pool for GA optimization
N_{bits}	Total number of bits in a member of a GA population
N_{GEN}	Number of GA generations
P_T	Tail planform
P_W	Wing planform
$P_1, P_2, P_3 \dots$	Penalty functions
$r_1, r_2, r_3 \dots$	Penalty function multipliers
Re	Reynolds number based on wing root chord ($\frac{\rho V_{\infty} C_{root}}{\nu}$)
S	Wing Area
S_T	Tail area
S_W	Wing area
t	Wing thickness
T	Thrust force
V_{∞}	Freestream velocity or cruise speed
W	Aircraft weight
\underline{x}	Design variable vector
x_{ACT}	Location of aerodynamic center of tail
x_{ACW}	Location of aerodynamic center of wing
x_{CG}	Location of center of gravity of aircraft
x_{CP}	Location of center of pressure
x_{AC}	Location of aerodynamic center
$x_{max \text{ span}}$	Chordwise location of maximum wingspan normalized by root chord
x_{prop}	Location of propeller

x_T	Location of tail
y_{MAC}	Spanwise location of MAC
Z	Number of members in a GA population
z_T	Height of tail below fuselage centerline
z_W	Height of wing above fuselage centerline

Greek Symbols

α	Angle of attack in degrees
$\tilde{\alpha}$	Angle of attack of aircraft
α_{eff}	Effective angle of attack
α_{peak}	Angle of attack at which pitching moment reaches local maximum
α_{stall}	Stall angle of attack
α_{safety}	Safety margin for stall angle of attack
$\Delta\alpha$	Step in angle of attack for integration of h_{AC}
$\Delta\tilde{\alpha}$	Angle of attack increment used in longitudinal stability check
ϵ_1	Tolerance of lift constraint
ϵ_2	Tolerance of trim constraint
ν	Viscosity
ρ	Air density

Abbreviations

AC	Aerodynamic center
CG	Center of gravity
CP	Center of pressure
DV	Design variable
KPH	Kilometers per hour
LAR	Low aspect ratio
L.E.	Leading edge
MPH	Miles per hour
MAV	Micro air vehicle

Chapter 1

Introduction

1.1 Motivation for Research: Small UAVs and MAVs

A great deal of interest has emerged during the last half-decade for a totally new kind of unmanned aerial vehicle. Although large unmanned aircraft such as the Hunter, Pioneer, and Predator have been successful for many years as theater-level military reconnaissance platforms, a need for a smaller, platoon-level unmanned aircraft exists. Small UAVs such as the Pointer, Sender, and more recently, the DragonEye, have arisen to fulfill this need. An even smaller alternative is the micro air vehicle (MAV). MAVs are expected to be carried by soldiers in the field and to be deployed for the purpose of answering the question: "what's over the next hill?". For this purpose, MAVs are envisioned to be small, semi-autonomous airplanes with limited but versatile performance characteristics. One proposed set of requirements [1] suggests that MAVs should have a maximum dimension of approximately 15 *cm* (5.9 *in*), be easily controlled by soldiers, and be able to operate at short to medium ranges in the order of 10 *Km* (6.2 *mi*), with an endurance of approximately 30 minutes. In addition, MAVs should be capable of carrying a variety of sensing and/or surveillance payloads with a typical payload of 18 *g* (0.63 *oz*). Successful operational MAVs meeting some of these proposed requirements include AeroVironment's Black Widow, BAE/Lockheed Martin's MicroSTAR, and the Naval Research Laboratory's Mite and Mite II.

The design of efficient MAVs is hindered, however, by the lack of a thorough understanding of the aerodynamics associated with small airplanes flying at low speeds. The operating cruise speed of MAVs is typically between 16 and 80 *KPH* (10 and 50 *MPH*), yielding an operating Reynolds numbers range between roughly 70,000 and 200,000. Furthermore, the requirement of smallness and compactness dictates the use of very low aspect ratio (LAR) wings (approximately $AR = 1$). A need exists for detailed aerodynamic analysis tools that are applicable to the Reynolds number and aspect ratio operating conditions found in MAVs and in some small UAVs.

The present work provides comprehensive aerodynamic data for low aspect ratio wings operating at low Reynolds numbers. The data is based on wind tunnel experiments of wing models with aspect ratios between 0.5 and 2.0 at Reynolds numbers between 70,000 and 200,000. The effect of wing planform is also studied as part of this project. Four distinct planforms are used for all aspect ratios and Reynolds numbers. In addition to this basic set of data, experimental results are also included that provide general information about other aerodynamic effects, including the increase of drag due to a fuselage body and the influence of leading edge shape on lift and pitching moment.

1.2 A Short Discussion of LAR Wings at Low Re

The aerodynamics of low aspect ratio wings at low Reynolds numbers have essentially not been studied. Investigations of the two-dimensional aerodynamic characteristics of airfoils at low Reynolds number have been conducted at the University of Notre Dame by Pelletier and Mueller [2]. Three-dimensional LAR wings have been extensively researched at higher Reynolds numbers in the form of delta wings at subsonic, transonic, and supersonic speeds. Many of these studies have focused on the high-angle-of-attack aerodynamics of delta and other types of pointed LAR wings. For MAVs, delta wing planforms are not ideal because for a given maximum dimension, delta wings offer less lifting area (and therefore less payload capability) than a rectangular or circular wing of the same maximum dimension.

Some information is available, however, regarding non-delta LAR wings, with much of the research having been done between 1930 and 1950. Zimmerman [3], Bartlett and Vidal [4], and Wadlin [5] performed experiments of LAR wings, although at significantly greater Reynolds numbers. Theoretical and analytical treatises of LAR wing aerodynamics were considered by Bollay [6], Weinig [7], Bera and Suresh [8], Polhamus [9, 10], and Rajan and Shashidhar [11].

Perhaps the most complete analysis and review of LAR wings was performed by Hoerner in his two-volume series on lift and drag [12, 13]. Hoerner reviewed many of the theories developed for LAR wings of non-delta planforms. A variety of correlations as well as analytical methods were presented and compared with the available experimental data of the time. Although the information presented by Hoerner corresponds to higher Reynolds numbers than the ones considered in the present work, the aerodynamic theory still holds.

This theory correctly predicts that as a finite wing of a given aspect ratio generates lift, counter-rotating vortical structures form near the wingtips. These vortices strengthen as the angle of attack increases. For a low aspect ratio wing, the tip vortices may be present over most of the wing area and therefore exert great influence over its aerodynamic characteristics. Wings of AR less than or equal to 1 can be considered to have two sources of lift: linear and nonlinear [13]. The linear lift is created by circulation around the airfoil and is what is typically thought of as lift in higher AR wings (Figure 1.1). The nonlinear lift is created by the formation of low pressure cells on the wing's top surface by the tip vortices, such as that observed in delta wings at high angles of attack [14]. This nonlinear effect increases the lift-curve slope as α increases and it is considered to be responsible for the high value of α_{stall} (Figure 1.2).

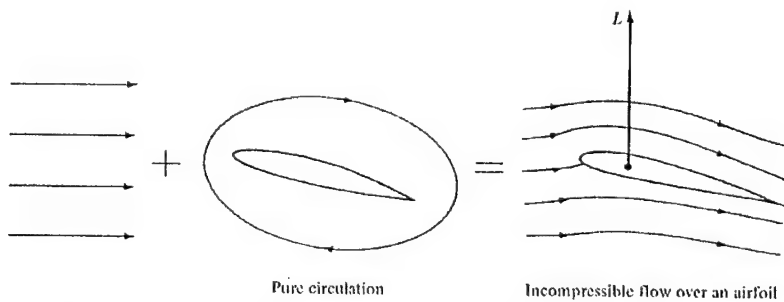


Figure 1.1: Linear Lift of LAR Wings Due to Circulation

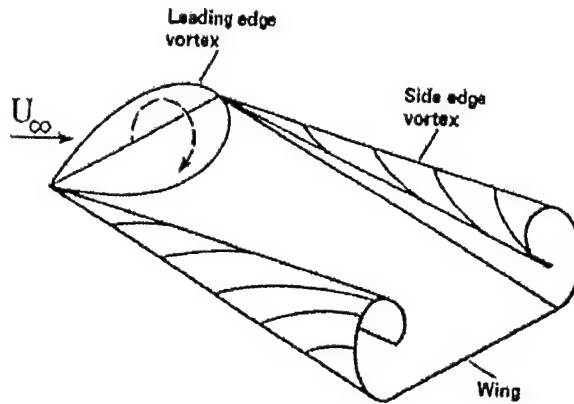


Figure 1.2: Nonlinear Lift of LAR Wings Due to Wingtip and Leading Edge Vortices

1.3 Scope of Present Work

1.3.1 Aerodynamic Data and Analysis

The first section of this report provides a summary of wind tunnel data corresponding to wings of low aspect ratio and various planforms at low Reynolds numbers. This set of data includes aspect ratios between 0.5 and 2.0, four distinct wing planforms, and Reynolds numbers in the range of 70,000 to 200,000. The results consists of lift, drag, and pitching moment coefficients as a function of angle of attack. Analysis of this experimental data reveals important characteristics of LAR wings at low Re , including definite nonlinearities, high stall angles of attack, and a great influence of aspect ratio and wing planform on aerodynamic performance.

1.3.2 Optimization Code and Analysis Procedure

The second section of this report presents one of many possible real-world applications of the experiment results for the current research. The data of force and moment coefficients versus angle of attack for each of the planforms and aspect ratios is implemented into an aerodynamic analysis program, which itself is part of a design-optimization procedure applicable to small unmanned aerial vehicles and micro air vehicles. The definition of an example design problem is presented first, as well as identification of design variables and aircraft performance measures of merit. A design-optimization procedure based on genetic algorithms is discussed next. Finally, the aerodynamic analysis code that determines the performance of a given set of design variables is presented. This analysis procedure makes use of both empirical relations based on wind tunnel data and also applies conventional aerodynamic analysis tools.

Chapter 2

Experimental Setup

2.1 Wing Models

The main objective of the present study is to determine the aerodynamic characteristics of LAR wings as influenced by the following three principal factors:

1. Wing planform.
2. Aspect ratio.
3. Reynolds number.

In order to study the effect of wing planform, four distinct geometries were chosen. The planforms used were rectangular, Zimmerman, inverse Zimmerman, and elliptical. The Zimmerman and inverse Zimmerman planforms are based on the wingtip shapes designed by Zimmerman in the early 1930's (Zimmerman [15]) and consist of two half-ellipses joined at either the quarter-root-chord location (in the case of the Zimmerman planform) or at the three-quarter-root-chord location (in the case of the inverse Zimmerman). Figure 2.1 shows an illustration of how the Zimmerman planform geometries are generated. In this diagram, two half-ellipses are joined at the quarter-root-chord location. One ellipse has semi-major axis a_3 and semi-minor axis a_1 while the other has semi-major axis a_2 and semi-minor axis a_3 .

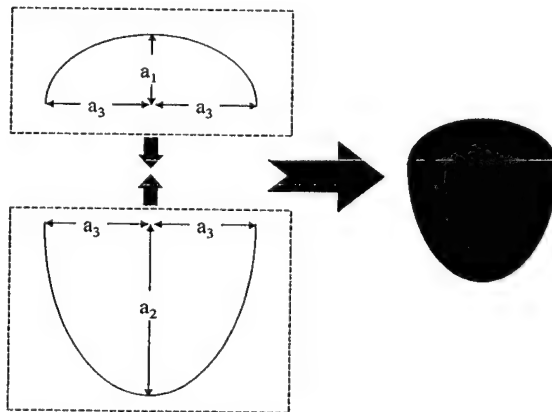


Figure 2.1: Formation of the Zimmerman Planforms

For each of the four planforms, a total of seven aspect ratio values were tested varying from 0.50 to 2.00 in increments of 0.25. Figure 2.2 shows the planform of the wings tested in wind tunnel experiments.





























AR	Rectangular	Zimmerman	Inv. Zimmerman	Elliptical
0.50				
0.75				
1.00				
1.25				
1.50				
1.75				
2.00				

Figure 2.2: Wing Planforms Used in Experiments

All models have a thickness-to-chord ratio of 1.96% and 5-to-1 elliptical leading and trailing edges (see Figure 2.3). The rectangular planforms have flat side edges and elliptical leading and trailing edges while the non-rectangular planforms have elliptical edges around the entire model.

For the rectangular wing of aspect ratio 2.00, two additional leading edge shapes were studied. These were a 10° and a 20° tapered leading edge shape, as shown in Figure 2.4 and 2.5. Each of these tapered shapes is actually two distinct L.E. geometries depending on the orientation of the wing in the tunnel. More details of how orientation yields different L.E. flow geometries are given in Section 3.6. The trailing edges of these modified models are still 5-to-1 elliptical in shape.

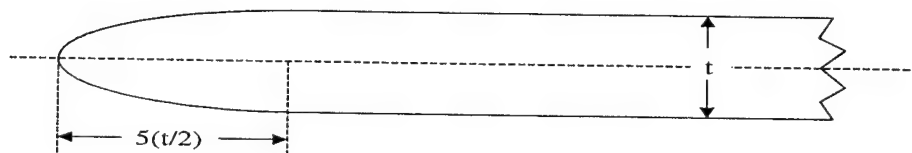


Figure 2.3: Leading Edge Geometry: 5-to-1 Elliptical L.E.

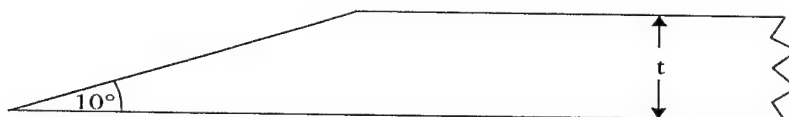


Figure 2.4: Leading Edge Geometry: 10° Tapered

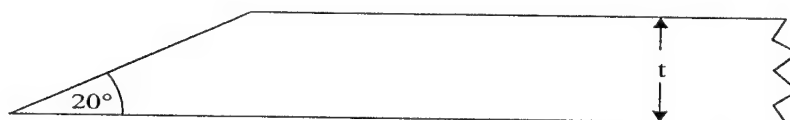


Figure 2.5: Leading Edge Geometry: 20° Tapered

Finally, two fuselage body models were used to determine the increase in drag coefficient generated by the presence of a fuselage. The fuselages were designed to be similar in shape and fineness ratio to the type of fuselages usually found in MAVs and small UAVs. The two models have fineness ratios of 7.0 and 8.5. Both models have a square cross-section with rounded corners, and a nose cone which simulates the shape of a typical MAV front section. Figure 2.6 shows a picture of the fuselage bodies attached to rectangular and inverse Zimmerman wings.

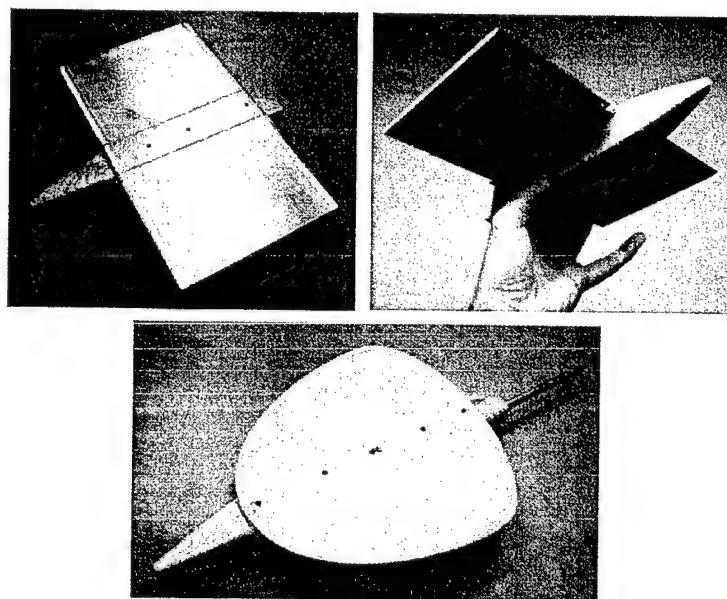


Figure 2.6: Fuselage Bodies

2.2 Wind Tunnel

Wind tunnel experiments were performed using a low-turbulence, indraft, open-circuit wind tunnel located at the University of Notre Dame's Hessert Center for Aerospace Research. This wind tunnel has a contraction ratio of 20.6 to 1, a rectangular inlet contraction cone designed for low turbulence intensities, and a 2 ft by 2 ft test section (61 cm by 61 cm). Over the speed range used for most experiments, the turbulence intensity in the test section has been determined to be less than 0.05%. More details of this wind tunnel are available in Mueller [16]. A schematic of the tunnel is shown in Figure 2.7.

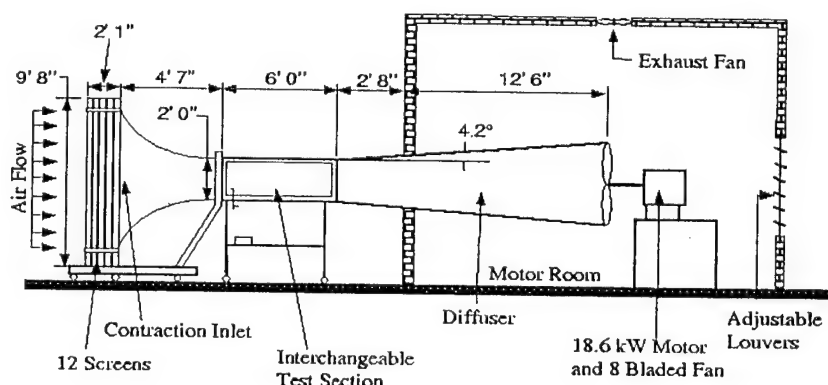


Figure 2.7: Schematic of the Low-Speed Wind Tunnel

2.3 Force Balance and Sting Balance

2.3.1 Platform Force Balance

All lift and drag measurements were made using a specially designed two-component platform force balance. The balance is mounted externally on top of the wind tunnel test section. A sting and sting arm connect the balance to the model. The forces are measured through two independent platforms (one for lift and one for drag). The platforms are attached to two flexures on which strain gages are mounted in a full Wheatstone bridge configuration. The flexures are sized to allow a resolution of 1 gram, which allows the balance to measure lift and drag forces of wings models down to a Reynolds number of approximately 20,000. A computer-controlled stepper motor and associated gearing system is used for changing the angle of attack of the model. Figure 2.8 shows a picture of the platform force balance.

The models were mounted vertically and attached to the force balance sting through a sting arm in the trailing edge of the model (see Figure 2.9). A streamlined sting covering protected the sting from the freestream velocity, such that the only forces experienced by the force balance were the forces on the model.

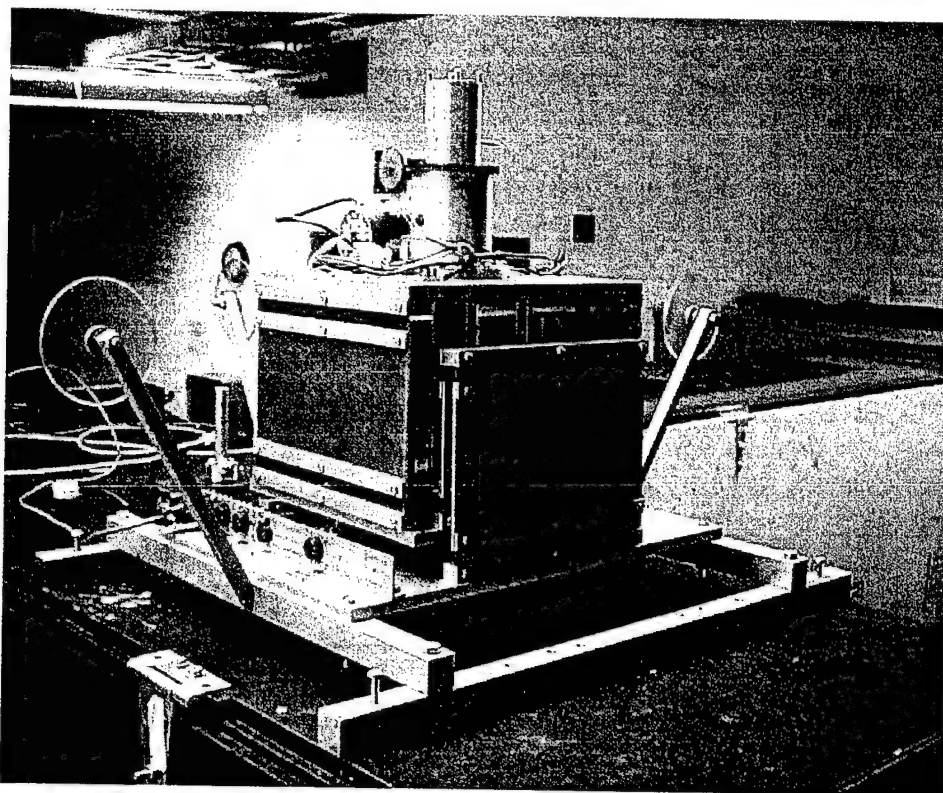


Figure 2.8: Platform Force Balance

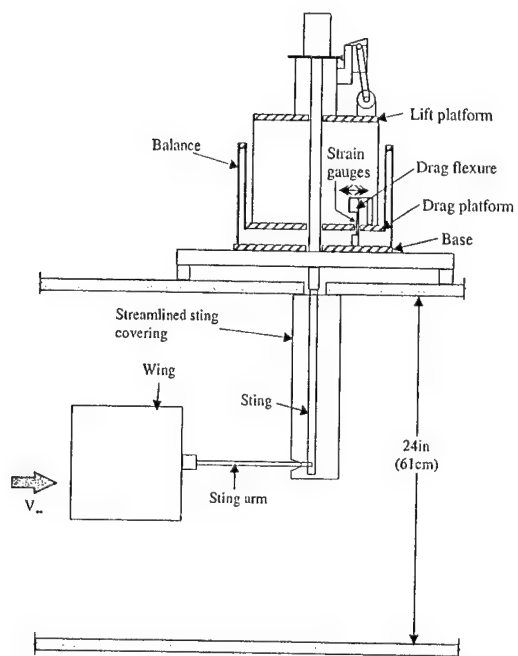


Figure 2.9: Mounting of Wing Models with Platform Force Balance

2.3.2 Five-Component Sting Balance

A five-component internal sting balance made by Aerotech ATE was used to measure normal force and pitching moment. This balance has strain gages arranged in full-Wheatstone-bridge configurations and is capable of measuring normal and side forces as well as pitching, rolling, and yawing moments. A picture of the balance and its mounting sleeve (used to secure the wings to the balance) is shown in Figure 2.10.

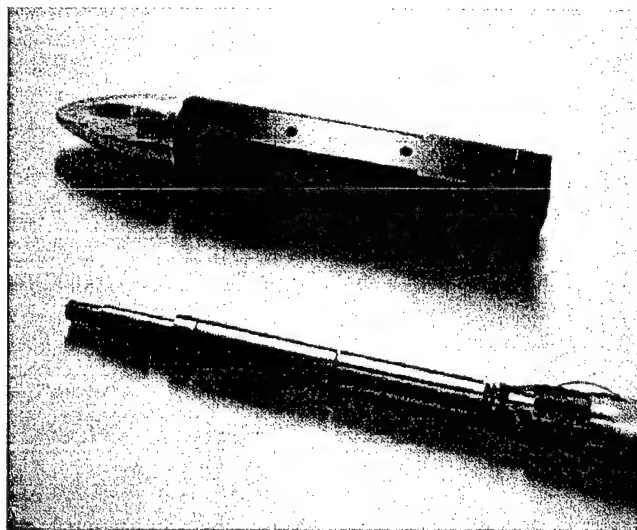


Figure 2.10: Aerotech Five-Component Sting Balance and Mounting Sleeve

The wing models were mounted vertically and attached directly to the sting balance mounting sleeve. A machined nose cone was attached to the front of the sleeve to minimize the disturbance to the flow. A computer-controlled stepper motor was used to change the angle of attack of the wings. Figure 2.11 shows a typical mounting arrangement for measurements with the sting balance (Zimmerman model of aspect ratio 2.00 is pictured).

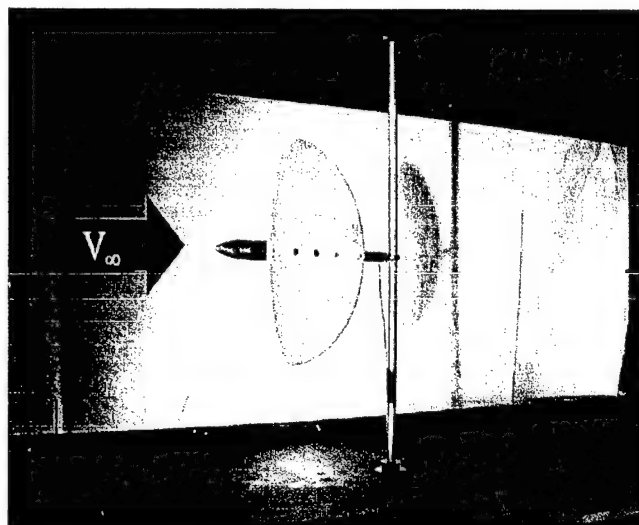


Figure 2.11: Mounting of Wing Models with Sting Balance

2.4 Signal Conditioning and Data Acquisition

The voltage output from each of the strain gages of either the platform force balance or the sting balance was processed using a strain-gage conditioning, low-noise amplifier with a 10 Hz low-pass filter. Typical gains used for the platform force balance were in the order of 2,000 while for the sting balance, the gains were closer to 4,000. All data was acquired using a PC-based data acquisition system running the LABVIEW® 5 graphical programming language. A *United Electronics Industries* 12-bit A/D card was used. Throughout the experiments, 8,000 data samples were acquired quasi-simultaneously per input channel at a frequency of 1000 Hz. Both mean and standard deviation were calculated from these 8,000 samples per channel. The standard deviation is used in the uncertainty analysis.

2.5 Experimental Procedures

The angle of attack of the wing models was varied from $\alpha = -10^\circ$ to a large positive angle between $\alpha = 30^\circ$ and $\alpha = 50^\circ$, in increments of 1° . Smaller increments of angle of attack were used near $\alpha = 0^\circ$. The wing was then brought back to $\alpha = 0^\circ$ to determine whether hysteresis was present or not. No hysteresis was observed in any of the measurements. At each angle of attack, the voltage of an electronic manometer connected to a pitot-static probe in the tunnel was also measured in order to determine the dynamic pressure to be used for non-dimensionalization of the forces and moments.

For all of the experiments involving the force balance or the sting balance, an offset and drift measurement was made at the beginning and end of all experiments. The drift was assumed to vary linearly throughout the experiment.

The chord Reynolds numbers presented are all *nominal* values (not corrected). For the experiments of lift, drag, and moment versus angle of attack, the freestream velocity V_∞ in the test section was always adjusted with the model at $\alpha = 0^\circ$ to yield the desired nominal Reynolds number. The force and moment coefficients presented in this report have all been corrected for wind tunnel blockage (solid blockage, wake blockage and streamline curvature) according to the techniques presented by Pankhurst and Holder [17]. Their techniques are equivalent to techniques described by Rae and Pope [18].

2.6 Uncertainty

The two main sources of uncertainty for the force and moment coefficients are the quantization error of the data acquisition card and the uncertainty arising from the standard deviation of a given mean strain gage output voltage. The Kline-McClintock [19] technique for error propagation was used to evaluate all uncertainties in the aerodynamic coefficients. This procedure can yield very large percentage uncertainties for small coefficients approaching zero. For larger coefficients (at $\alpha > 10^\circ$), these percentage uncertainties are in the order of 6% for C_L , C_D and C_M . As an example of typical error bounds for the wind tunnel data presented in this report, curves of C_L , C_D , and C_M (along with error bars corresponding to the 95% uncertainty bounds of each data point) are plotted in Figures 2.12, 2.13, and 2.14 versus angle of attack. The rectangular wing of $AR = 1.00$ at a Reynolds number of 100,000 is used as the example since it represents typical values for the worse-case conditions of uncertainty. As the Reynolds number or aspect ratio increases, the relative uncertainty values decrease due to the larger forces involved. The uncertainty in the angle of attack was determined to be of the order of $0.5^\circ - 0.7^\circ$ for most test cases.

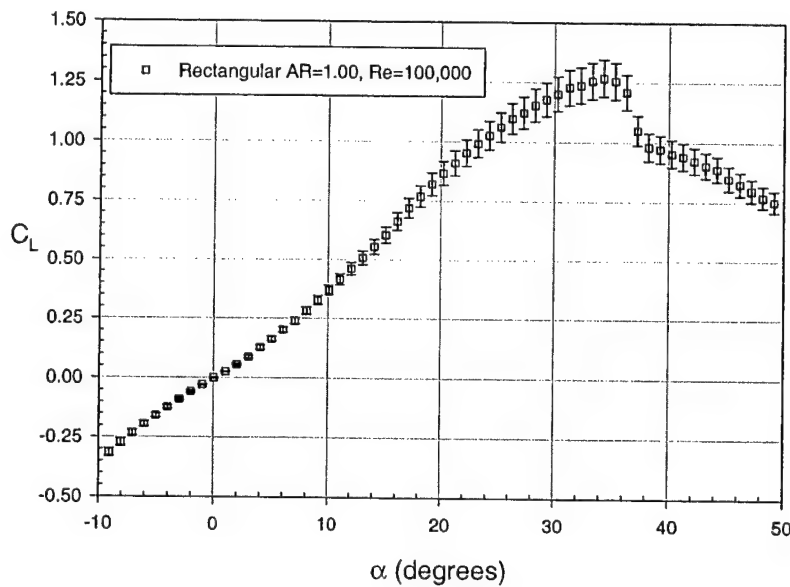


Figure 2.12: Uncertainty in C_L , Rectangular Wing of $AR = 1.00$, $Re = 100,000$

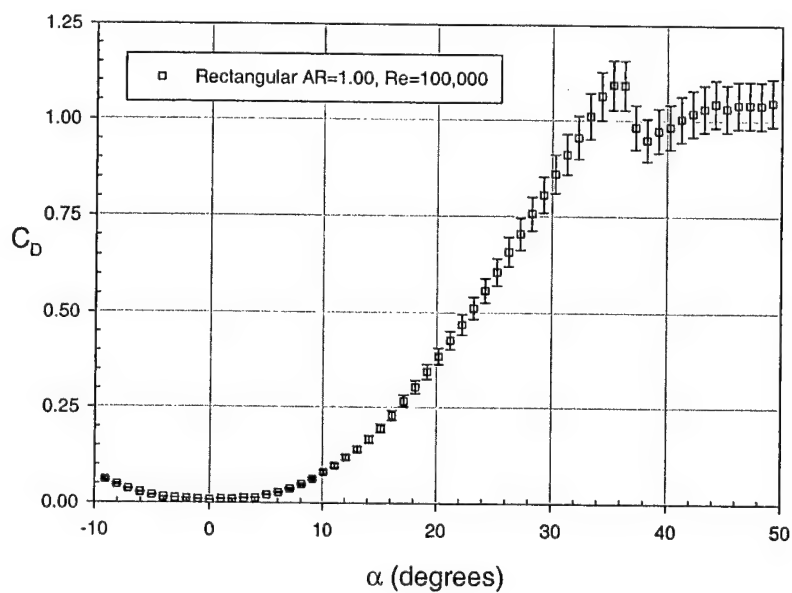


Figure 2.13: Uncertainty in C_D , Rectangular Wing of $AR = 1.00$, $Re = 100,000$

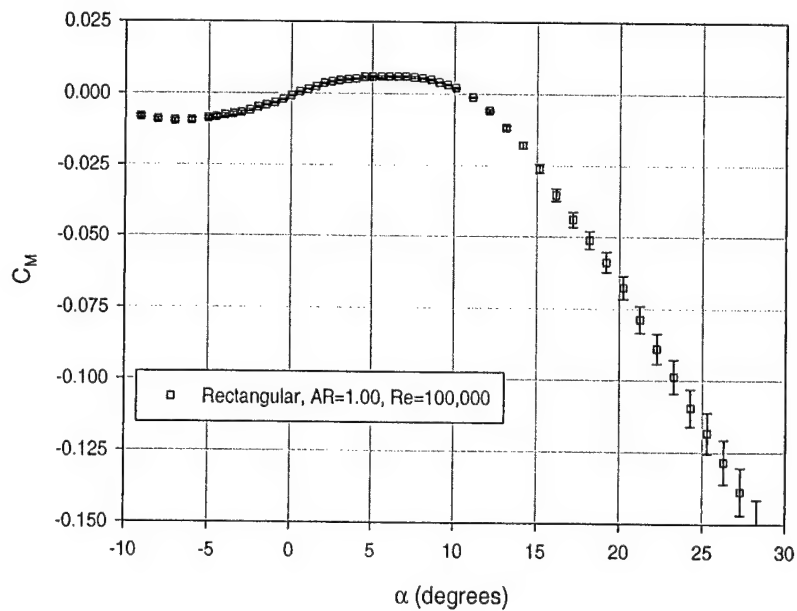


Figure 2.14: Uncertainty in C_M , Rectangular Wing of $AR = 1.00$, $Re = 100,000$

Chapter 3

Analysis of Experimental Data

3.1 Discussion of Aerodynamic Results

Appendix A contains plots of the experimental results. The data is arranged into two categories: grouped by aspect ratio and grouped by wing planform. In this manner, the first grouping is appropriate for determining the effect of planform for wings of the same aspect ratio while the second grouping is appropriate for determining the effect of aspect ratio for the same planform. Some observations about the data are:

1. Wings of aspect ratio below 1.25 have highly nonlinear lift curves that are characterized by high stall angles of attack and non-constant lift-curve slopes in the pre-stall region.
2. Above an aspect ratio of 1.25, most of the planforms exhibit lift curves that are more linear. As predicted by theory, the higher the aspect ratio, the more linear the relationship between lift and angle of attack.
3. For aspect ratios below 1.50, a definite performance advantage is seen for the inverse Zimmerman and rectangular planforms over the elliptical and Zimmerman planforms. This is particularly noticeable when comparing the C_L versus C_D plots for constant aspect ratio (Figures A.3, A.7, A.13, and A.19). This observation is further discussed in Section 3.1.1.
4. Above an aspect ratio of 1.50, the difference between planforms becomes less clear and is only truly apparent at very high angles of attack beyond stall.
5. Aspect ratio is by far the most important parameter affecting the aerodynamic characteristics of LAR wings at low Re . Wing planform is the next most important factor, followed by Reynolds number. Leading edge shape (discussed in more detail in Section 3.6) is also critical. However, the present research has not included a comprehensive study of the effect of leading edge shape.

3.1.1 Lift Performance Related to Tip Vortices

The effect of wing planform on the lift characteristics of LAR wings for a given aspect ratio and Reynolds number can be further analyzed by introducing the parameter $x_{\max \text{ span}}$. $x_{\max \text{ span}}$ is the chordwise location (measured from the leading edge) of maximum wingspan, non-dimensionalized by the root chord of the model. For the Zimmerman, elliptical, and inverse Zimmerman wings, $x_{\max \text{ span}}$ is 0.25, 0.50, and 0.75, respectively. For the rectangular wings, $x_{\max \text{ span}}$ is taken to be 1.0 rather than 0. In essence, $x_{\max \text{ span}}$ provides an indirect measure of the distance between the wingtip vortices as they develop over the wing and travel downstream. It was determined from flow visualization experiments that the distance between the wingtip vortices varied proportionally with the chordwise location of maximum span.

This can best be described by use of the sketch and photographs of Figure 3.1. For wing shapes in which the maximum span is located upstream of the half-root-chord location ($x_{\max \text{ span}} \leq 0.5$), the tip vortices are seen to first develop at the location of maximum wingspan. The vortices then follow the outline of the wing up to a point and separate from the wing. In contrast, for wings with $x_{\max \text{ span}}$ greater than 0.5, the vortices are seen to separate from the wing at the location of maximum span. Thus the vortices of wings with $x_{\max \text{ span}} > 0.5$ are further apart than those of wings with $x_{\max \text{ span}} \leq 0.5$. Figure 3.2 shows another set of flow visualization photographs which outline the shape and relative distance of the wingtip vortices over low AR wings.

Hoerner [13] suggested that the lift performance of low aspect ratio wings improves as the distance between the wingtip vortices increases. One direct way to measure lift performance is to compare the lift-curve slope, $C_{L\alpha}$, for each wing and aspect ratio. The lift-curve slope is calculated through a least-squares linear regression procedure applied to the experimental data for $-10^\circ \leq \alpha \leq 10^\circ$. For this limited range of angles of attack, the lift curve is "linear enough" to allow a valid determination of $C_{L\alpha}$. As can be seen from the representative case at a Reynolds number of 100,000 (Figure 3.3), $C_{L\alpha}$ is seen to increase as $x_{\max \text{ span}}$ increases. A more detailed analysis of the lift and drag characteristics of LAR wings can be found in Torres and Mueller [20].

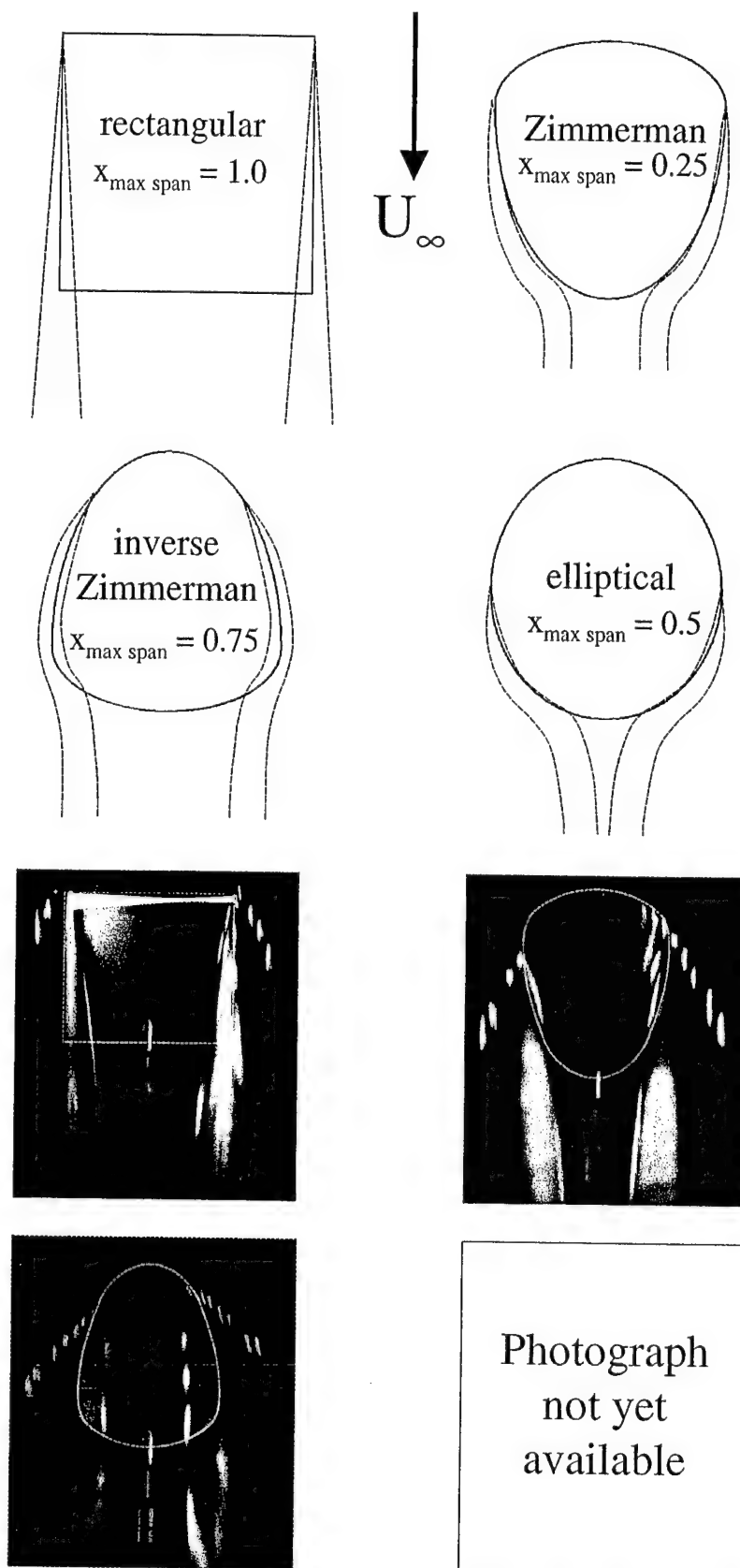


Figure 3.1: Separation of Wingtip Vortices Schematic and Comparison with Flow Visualization of Three Planforms ($AR = 1.0$, $Re \approx 70,000$, $\alpha = 15^\circ$)

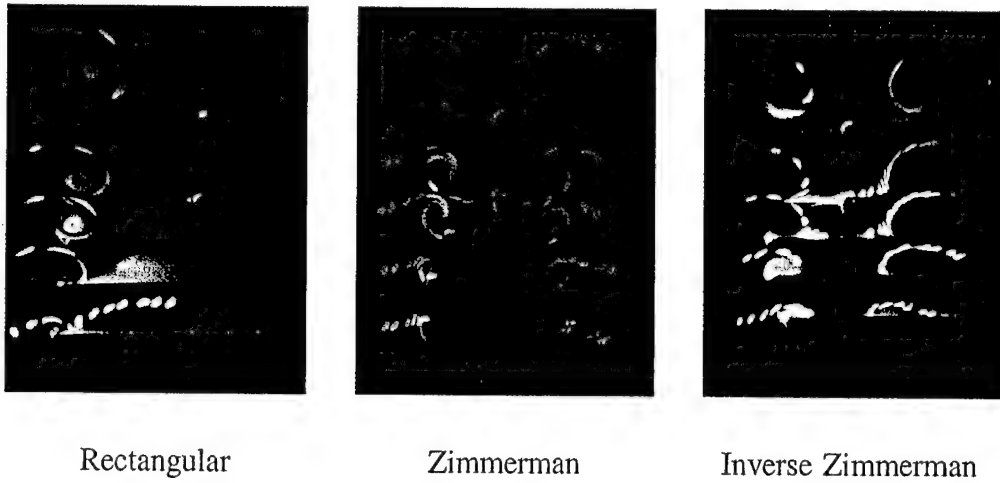


Figure 3.2: Flow Visualization of Wingtip Vortices ($AR = 1.0$, $Re \approx 70,000$, $\alpha = 15^\circ$)

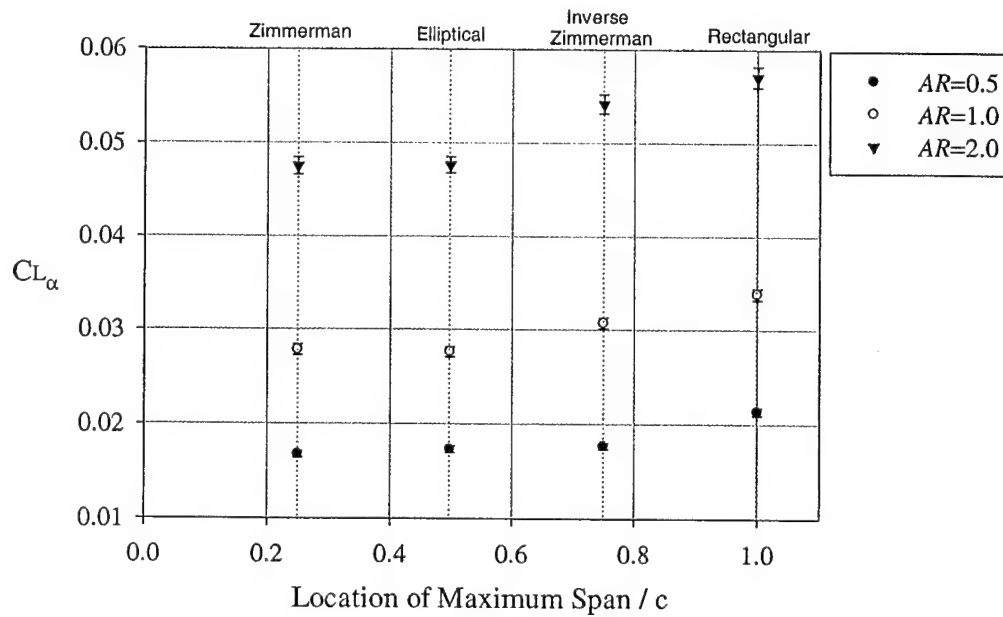


Figure 3.3: Lift Curve Slope, C_{L_α} vs. $x_{\max \text{ span}} / c$ for $Re = 100,000$

3.2 Maximum Lift Coefficient and Stall Angle of Attack

An important characteristic of LAR wing aerodynamics is their high stall angles of attack and relatively high maximum lift coefficients. The experimental data of Appendix A is used in this section to define $C_{L_{max}}$ and α_{stall} for all the planforms and all aspect ratios studied in this work. Before discussing the results, some issues regarding the selection of the maximum lift coefficient in experiment results should be addressed. In most cases, the maximum lift coefficient can easily be determined as the point when a clear stall of the wing is observed. This is particularly true for the wings of higher aspect ratios. However, the lower aspect ratio wings are characterized by highly nonlinear lift curves. In some cases, a point of inflection in the lift curve exists and the lift coefficient decreases slightly before increasing again, as exemplified in Figure 3.4 for the rectangular planform of $AR=0.5$. In other cases, the point of inflection is not present, and the lift coefficient increases continuously until stall at a very high angle of attack as seen in the inverse Zimmerman case of $AR=0.5$ shown in Figure 3.5.

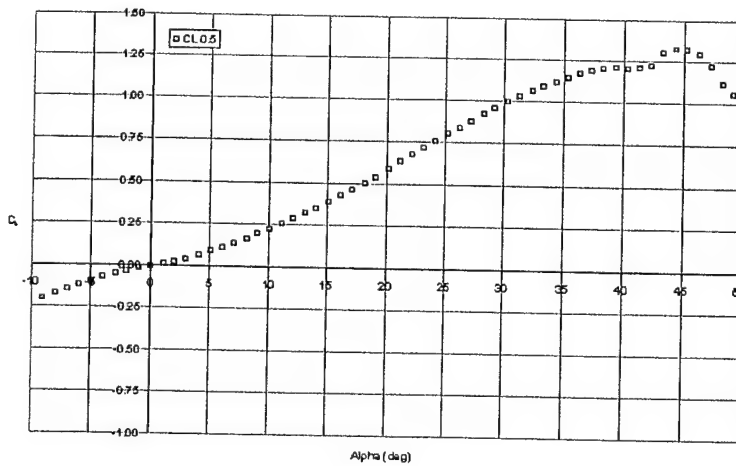


Figure 3.4: Lift Curve of Rectangular Wing, $AR=0.5$, $Re=100,000$

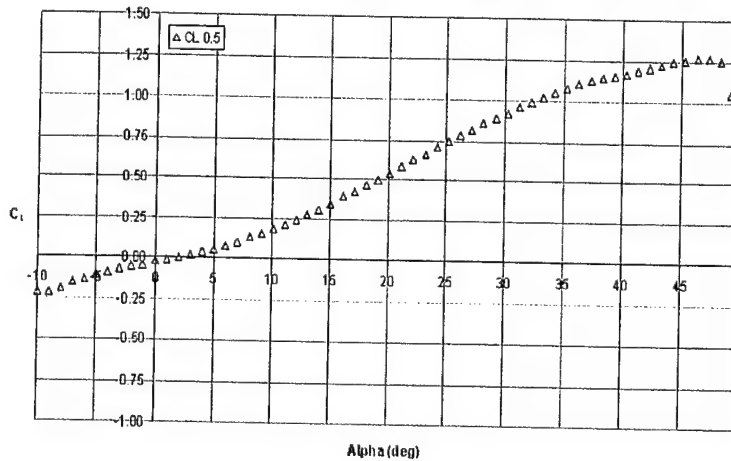


Figure 3.5: Lift Curve of Inverse Zimmerman Wing, $AR=0.5$, $Re=100,000$

In an effort to be consistent, the maximum lift coefficient is taken to be the point at which the lift coefficient reaches a local maximum and then decreases in value, even if it increases in value at higher angles of attack. If no decrease in C_L is observed, such as in Figure 3.5, the $C_{L_{\max}}$ is taken to be the maximum value of C_L (approximately 1.25 in the example of Fig. 3.5). It is suggested that Figures A.41, A.47, A.53, and A.59 be reviewed as references to what is considered $C_{L_{\max}}$ in each case.

Figures 3.6 and 3.7 plot the values of $C_{L_{\max}}$ and α_{stall} for each of the four planforms as a function of aspect ratio. It is evident from these graphs that wing planform has significant influence in the maximum lift characteristics of LAR wings. Specially noticeable is the difference between the rectangular and ellipse-based planforms.

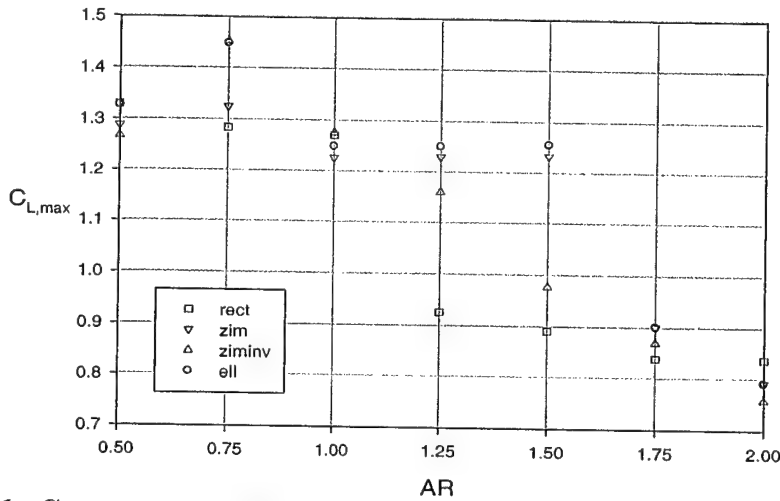


Figure 3.6: $C_{L_{\max}}$ of Four Wing Planforms and All Aspect Ratios ($Re = 100,000$)

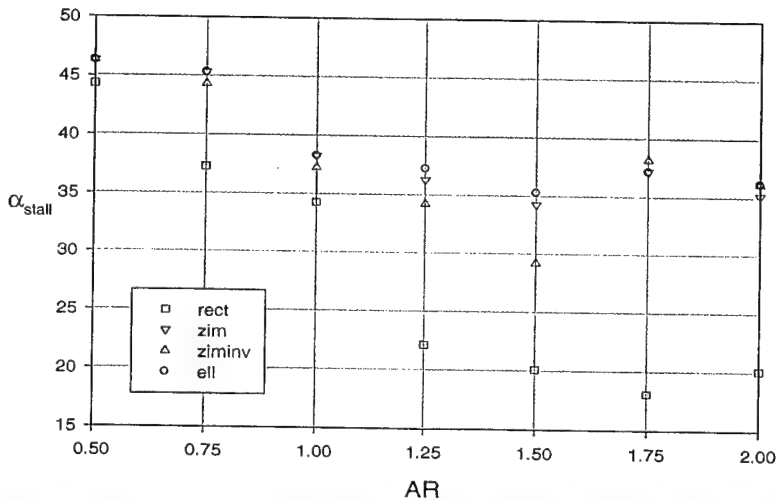


Figure 3.7: Stall Angle of Four Wing Planforms and All Aspect Ratios ($Re = 100,000$)

3.3 Aerodynamic Center

3.3.1 Background

One key aspect of low aspect ratio wing aerodynamics is the location of the aerodynamic center as a function of wing planform, aspect ratio, leading edge geometry, Reynolds number, and angle of attack. The AC location yields useful information about the structure of the flow around the wing, specially in the nonlinear lift regime.

The location of the AC can be calculated using sting balance data of normal force and pitching moment taken about the $\bar{c}/4$ location of each wing. Before continuing, however, a few definitions should be stated:

Center of Pressure: The center of pressure (x_{CP} or $h_{CP} = \frac{x_{CP}}{\bar{c}}$) is defined as the point along the chordwise direction of the wing at which the lift and drag forces can be assumed to be acting. In other words, the center of pressure is the location along the wing where the pitching moment is identically equal to zero. For symmetrical airfoils, the center of pressure is expected to lie close to the quarter-chord location (with respect to the wing's \bar{c}) and furthermore it is expected to be independent of angle of attack. For a cambered airfoil the center of pressure can shift significantly as the angle of attack changes.

Aerodynamic Center: The aerodynamic center (x_{AC} or $h_{AC} = \frac{x_{AC}}{\bar{c}}$) is defined as the point along the chordwise direction of the wing at which the pitching moment is independent of angle of attack, that is, $\frac{\partial C_{MAC}}{\partial \alpha} = 0$.

Neutral Point: The neutral point is similar to the aerodynamic center except that it applies to an entire aircraft. That is, the neutral point is the location along the length of an aircraft at which the pitching moment is independent of angle of attack.

Note that for a wing with no twist and with airfoil sections which are symmetric, the center of pressure and the aerodynamic center are one and the same. The assumption of an aerodynamic center that is independent of angle of attack and which lies near $\bar{c}/4$ is generally found to be valid for wings of high aspect ratio. As the aspect ratio decreases, h_{AC} can no longer be assumed to be independent of α .

3.3.2 Methods for Calculating the Location of the Aerodynamic Center

Results of wind tunnel experiments using the 5-component sting balance can be used to determine the location of the aerodynamic center. The applicable experimental data consists of normal force and pitching moment measured at the quarter-chord location with respect to the mean aerodynamic chord of the wing. Figure 3.8 shows a schematic of the forces and moments involved in AC analysis.

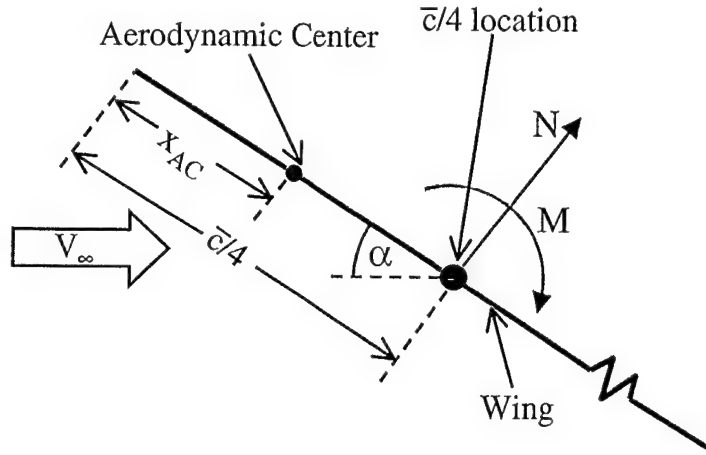


Figure 3.8: Aerodynamic Center Analysis

Transferring the forces and moments from the quarter-chord to a point x_{AC} located upstream of the quarter-chord location yields the following expression for the pitching moment about the AC:

$$M_{AC} = M_{\bar{c}/4} - (x_{\bar{c}/4} - x_{AC}) N. \quad (3.1)$$

Dividing both sides of this equation by $\frac{1}{2}\rho V_\infty^2 S \bar{c}$ leads to the nondimensional form of Eqn. 3.1:

$$C_{M_{AC}} = C_M - (0.25 - h_{AC}) C_N, \quad (3.2)$$

where $h_{AC} = \frac{x_{AC}}{\bar{c}}$ and where the subscript $\bar{c}/4$ has been dropped from the moment coefficient for simplicity. There are several ways in which the value of h_{AC} can be determined. The most straightforward method uses the knowledge that for a wing with no camber or twist, the aerodynamic center and the center of pressure (or center of lift) are one and the same. Furthermore, the moment at the AC is identically equal to zero. Setting Eqn. 3.2 equal to zero and solving for h_{AC} yields

$$h_{AC} = 0.25 - \frac{C_M}{C_N}. \quad (3.3)$$

This derivation is by far the simplest but it has the disadvantage that for angles of attack close to zero, the value of C_N goes to zero. Therefore, use of this equation yields a $1/x$ relationship as α goes to zero. It is expected to be accurate only for moderate to high angles of attack where the values of C_N and C_M are relatively large.

Another method for determining the location of the aerodynamic center is to differentiate Eqn. 3.2 with respect to angle of attack while assuming that h_{AC} is a constant with respect to α . By definition of the aerodynamic center, $\frac{\partial C_{MAC}}{\partial \alpha} = 0$. Thus,

$$\frac{\partial C_{MAC}}{\partial \alpha} = \frac{\partial C_M}{\partial \alpha} - (0.25 - h_{AC}) \frac{\partial C_N}{\partial \alpha} = 0. \quad (3.4)$$

Solving Eqn. 3.4 for h_{AC} yields

$$h_{AC} = 0.25 - \frac{C_{M_\alpha}}{C_{N_\alpha}} \quad (3.5)$$

This equation does not have a discontinuity near $\alpha = 0^\circ$ because the slope of the normal coefficient curve is not zero at zero angle of attack. If the assumption that h_{AC} is not a function of α is correct, this equation should yield a constant value for h_{AC} at all angles of attack before stall. Figure 3.9 shows plots of h_{AC} versus α obtained using Eqns. 3.3 and 3.5 for the rectangular wing of $AR = 1.0$ at $Re = 140,000$. The values of C_{N_α} and C_{M_α} were obtained by representing the curves of C_N and C_M versus α as polynomials of order 4 and 10 respectively. The slope was then calculated by differentiating the polynomials once with respect to α . More details of this polynomial slope method are presented in Section 3.3.3. As can be seen in the graph of Figure 3.9, neither equation for h_{AC} is accurate throughout the whole range of angles of attack. The curve obtained using Eqn. 3.3 has a large discontinuity for $\alpha \leq 3^\circ$, while the curve corresponding to Eqn. 3.5 is definitely not constant within the region of angles of attack before stall. Therefore, it can be concluded that the assumption of h_{AC} being independent of α is **not** accurate for LAR wings at low Re .

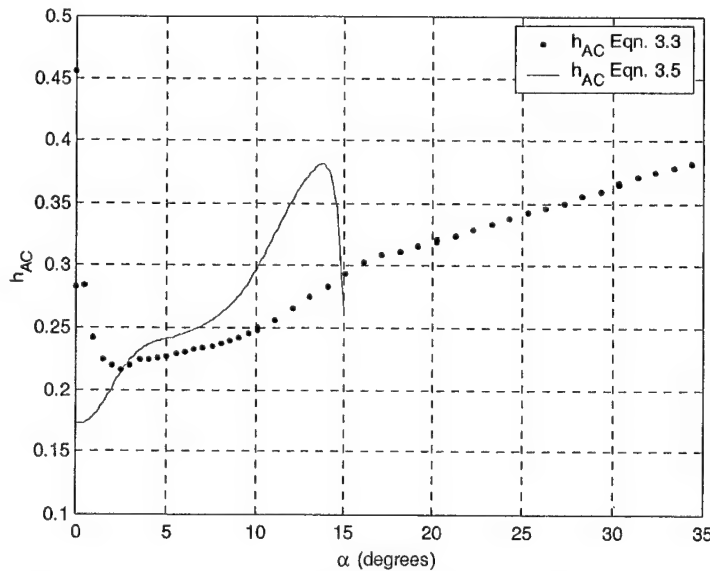


Figure 3.9: Calculation of h_{AC} using Eqns. 3.3 and 3.5, $AR = 1.0$ Rectangular Planform

Yet another approach that takes into account h_{AC} 's dependence on α is to differentiate Eqn. 3.2 with respect to α while assuming that h_{AC} is not a constant. This yields

$$\frac{\partial C_{MAC}}{\partial \alpha} = \frac{\partial C_M}{\partial \alpha} - (0.25 - h_{AC}) \frac{\partial C_N}{\partial \alpha} + C_N \frac{\partial h_{AC}}{\partial \alpha} = 0. \quad (3.6)$$

This equation can be solved for $\frac{\partial h_{AC}}{\partial \alpha}$:

$$\frac{\partial h_{AC}}{\partial \alpha} = \frac{1}{C_N} [(0.25 - h_{AC}) C_{N\alpha} - C_{M\alpha}]. \quad (3.7)$$

At $\alpha = 0^\circ$, $C_N = 0$ and the $\frac{\partial h_{AC}}{\partial \alpha}$ term in Eqn. 3.6 goes to zero. Thus a forward integration scheme can be used that uses the initial condition at $\alpha = 0^\circ$:

$$[h_{AC}]_{\alpha=0^\circ} = h_{AC}^{(0)} = 0.25 - \frac{[C_{M\alpha}]_{\alpha=0^\circ}}{[C_{N\alpha}]_{\alpha=0^\circ}} = 0.25 - \frac{C_{M\alpha}^{(0)}}{C_{N\alpha}^{(0)}}, \quad (3.8)$$

and the following first-order forward Euler method to integrate the angle of attack:

$$h_{AC}^{(i+1)} = h_{AC}^{(i)} + \frac{1}{C_N^{(i+1)}} \left[(0.25 - h_{AC}^{(i)}) C_{N\alpha}^{(i+1)} - C_{M\alpha}^{(i+1)} \right] \Delta\alpha, \quad i = 0, 1, 2, 3, \dots \quad (3.9)$$

Figure 3.10 plots the values of h_{AC} obtained through the use of Eqn. 3.9 as well as Eqn. 3.3. It can be concluded from this graph that the derivation of Eqn. 3.9 is accurate for low angles of attack and the one of Eqn. 3.3 is accurate at higher angles of attack. There is a region in which both methods overlap.

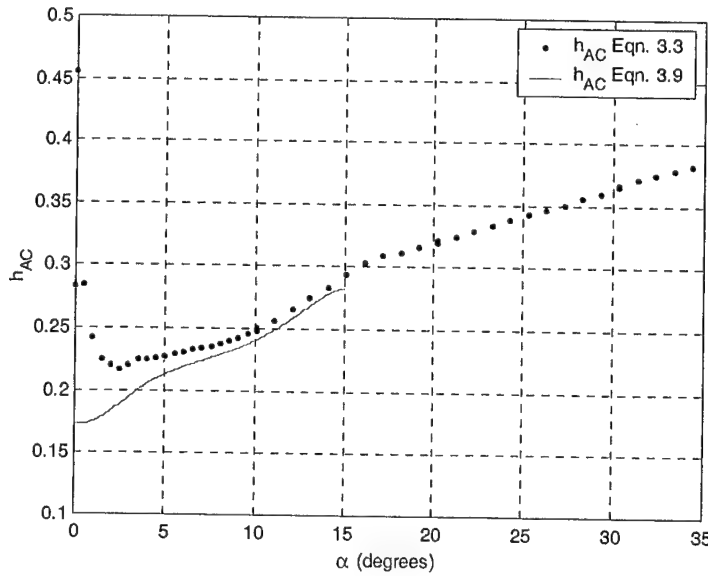


Figure 3.10: Calculation of h_{AC} using Eqs. 3.3 and 3.9, $AR = 1.0$ Rectangular Planform

3.3.3 Final Method Used for Calculating h_{AC}

The discussion of the previous section provides some insight into the complications associated with the calculation of the aerodynamic center for LAR wings at low Re . The method used for this report to determine h_{AC} is a combination of Eqns. 3.3 and 3.9. The procedure is as follows:

1. For a given wing planform, aspect ratio, and Reynolds number, wind tunnel data exists for C_N and C_M as a function of angle of attack. The range of α is typically between -10° and 40° with increments of 0.5° for $-5^\circ \leq \alpha \leq 10^\circ$ and of 1° for all other angles.
2. A polynomial of order 4 is fitted in a least squares sense to the data of C_N vs. α for $-3^\circ \leq \alpha \leq 15^\circ$. Similarly, a polynomial of order 12 is fitted to the data of C_M vs. α for $-3^\circ \leq \alpha \leq 15^\circ$. The reason for using polynomials instead of actual experimental data is that the natural scatter of the data generates changes in slope which are artificial in nature. The polynomial approximations of the data provide a smoothed curve and ease the task of calculating slopes since all that is required is to differentiate the polynomial once with respect to α . As an example, Figure 3.11 shows plots of C_N and C_M and their corresponding polynomial approximations for the rectangular planform of $AR = 1.0$ at $Re = 140,000$.

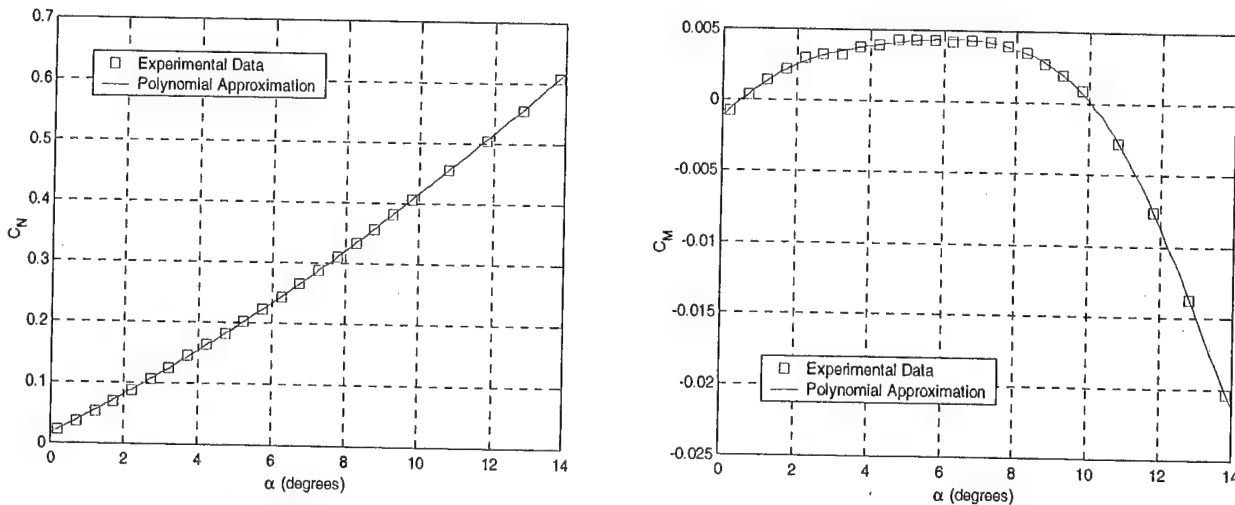


Figure 3.11: Polynomial Approximations to C_N and C_M , $AR = 1.0$ Rectangular Planform

3. The value of h_{AC} at $\alpha = 0^\circ$ is calculated using Eqn. 3.8. The values of the slopes of C_N and C_M are obtained by differentiation of the polynomials obtained in the previous step. The slopes are evaluated at $\alpha = 0^\circ$.
4. Eqn. 3.9 is used to integrate forward in α . The integration is carried out for $0^\circ < \alpha < 15^\circ$ in increments of 0.1° .
5. For angles of attack greater than 15° , Eqn. 3.3 is used. The values of C_N and C_M are taken directly from the actual experimental data (not the polynomial approximation).

6. For most of the wings tested, the transition from the differential approach of Eqn. 3.9 to the direct approach of Eqn. 3.3 at $\alpha = 15^\circ$ is seamless. In some cases, discontinuities do occur, but they are in general small and do not significantly affect the overall trend of the curve of h_{AC} versus α .

Figure 3.12 below plots the final result of this procedure for the rectangular wing of $AR = 1.0$ at $Re = 140,000$. The transition at $\alpha = 15^\circ$ is relatively smooth and the value of h_{AC} is considered valid for all angles of attack up to stall. All the graphs of h_{AC} versus α shown at the end of this section were obtained using the method outlined above.

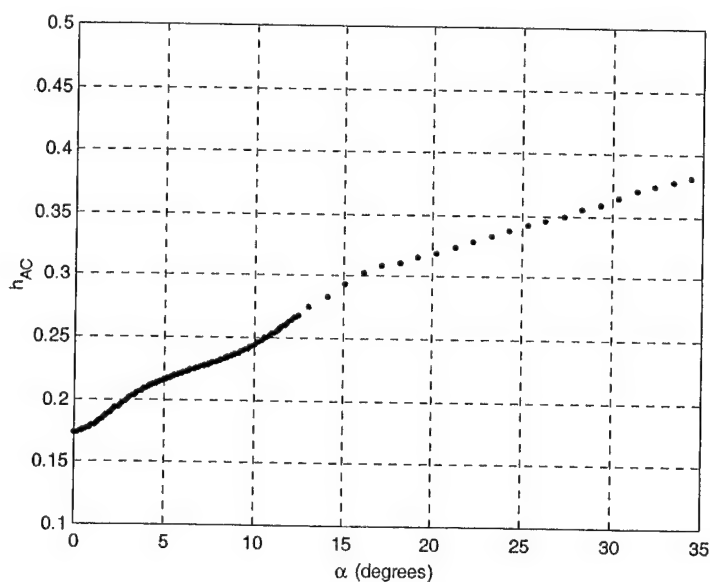


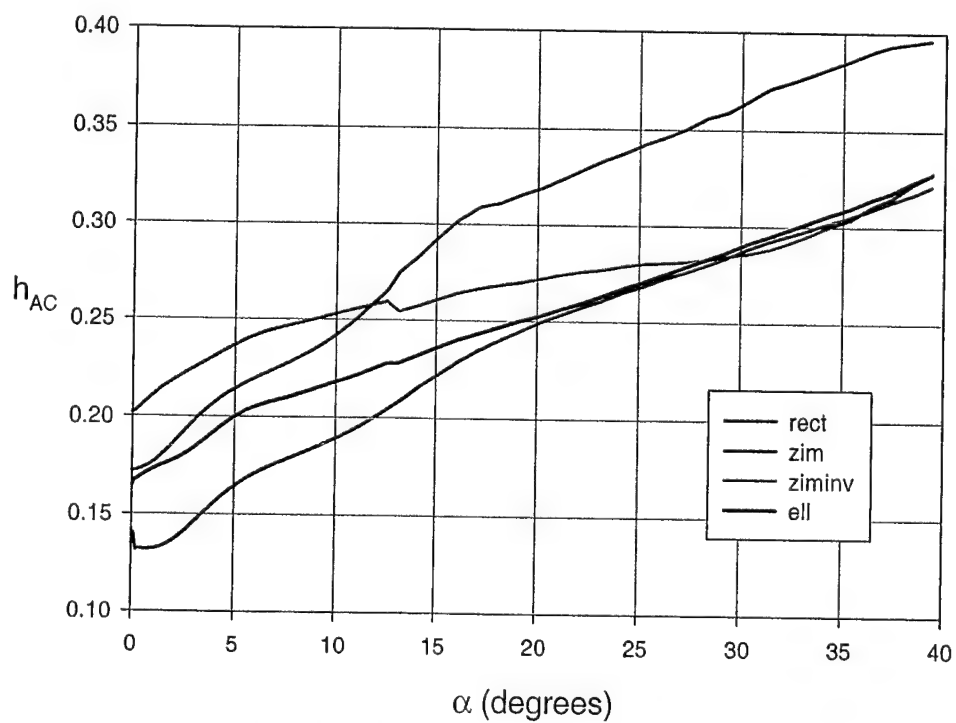
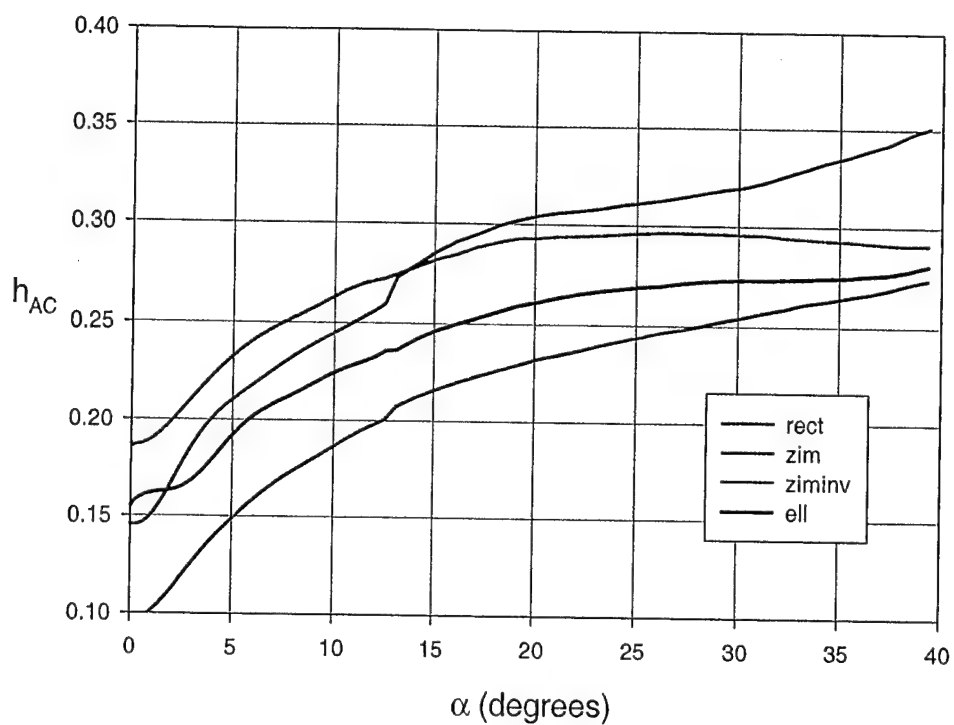
Figure 3.12: Calculation of h_{AC} Using a Combination of Eqns. 3.3 and 3.9

The uncertainty in the value of h_{AC} is difficult to calculate analytically as the procedure applied to determine the location of the AC involves polynomial curve fitting, forward Euler integration, and combinations of more than one technique. In lieu of an analytical uncertainty analysis, a computational one was used. That is, the computer program which implements the procedure outlined in this section was run repeatedly (1000 times). For each iteration, the values of the C_N , C_M and α were randomly varied by their known uncertainties. Thus 1000 graphs of h_{AC} vs. α were obtained. The mean and standard deviation of these curves provides an estimate of the uncertainty of the value of h_{AC} . The rectangular wing of $AR = 1.0$ at $Re = 100,000$ was used as a typical test case. The uncertainty in h_{AC} was found to vary between 2% for angles of attack close to 0° and 0.2% for angles of attack above 15° . In general, the maximum uncertainty of h_{AC} in the graphs presented in the next few pages is no larger than approximately 0.005 near $\alpha = 0^\circ$ and can be as small as 0.0005 for $\alpha \geq 15^\circ$. Figures 3.13 through 3.22 at the end of this section plot the value of h_{AC} versus angle of attack for all four planforms and six aspect ratios. The graphs group the data into either constant aspect ratio (useful to determine the effect of planform) or constant planform (useful to determine the effect of aspect ratio).

3.3.4 Discussion of Aerodynamic Center Results

The plots on the following pages provide great insight into the lift-generating mechanisms which operate in the regime of LAR wings at low Reynolds number. The most striking observation that should be made is the drastic shift in the location of the AC as angle of attack increases. As an example, consider the rectangular wing of $AR = 1.00$ shown in Figure 3.18. For this wing, h_{AC} is close to 0.17 at $\alpha = 0^\circ$ but increases to 0.40 at $\alpha = 40^\circ$. Since for uncambered wings, the aerodynamic center and the center of lift are one and the same, it can be concluded that the chordwise location at which the lift force is acting shifts downstream as the angle of attack increases. This is an expected trend based on the linear-nonlinear theory of LAR wings (see Section 1.2 for details). For low angles of attack, most of the lift generated by the wing is in the form of circulation lift, as seen in wings of high aspect ratio. Therefore, it is expected that the location of the AC will be close to 25% mark at these angles. However, as the angle of attack increases, the lift mechanism shifts to that generated by the wingtip vortices. These vortices generate lift by creating low-pressure sections on the upper surface of the wing, usually more on the downstream end of the wing (the wingtip vortices increase in size and strength as they travel downstream along the upper surface of the wing). It would be expected that because the lift generated at higher angles of attack is due to wingtip vortices (which are stronger near the trailing edge), the location of the center of lift would shift downstream. The amount by which the AC shifts towards the trailing edge is a direct indication of how much nonlinear lift is being generated by the wing. Wings of $AR = 0.75$ have a much steeper shift of AC with α than wings of $AR = 2.00$. If one were to plot h_{AC} versus α for a wing of $AR = 10.00$, this curve would be expected to be a horizontal line centered close to 0.25. h_{AC} would not be expected to change until α_{stall} is reached.

Another important conclusion that can be drawn from the AC analysis relates to the effect of planform and how some planforms are more "linear" than others. Zimmerman and elliptical planforms are seen to have a value of h_{AC} which is generally lower than that of rectangular and inverse Zimmerman planforms. This is probably due to the fact that, as discussed in Section 3.1.1, *zim* and *ell* planforms have a weaker wingtip vortex system than the one found in *ziminu* and *rect* planforms. As such, it would be expected that the AC of the planforms with the weaker vortices would be farther forward than the AC of wings with strong vortices. This is indeed the case.



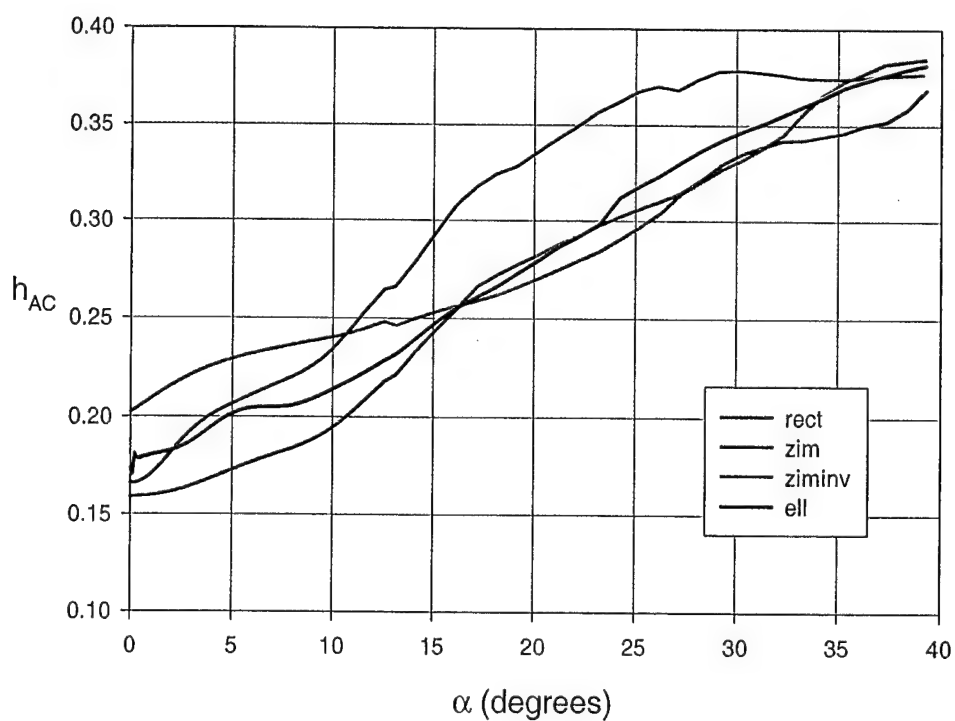


Figure 3.15: h_{AC} vs. α , $AR = 1.25$, $Re_c = 140,000$

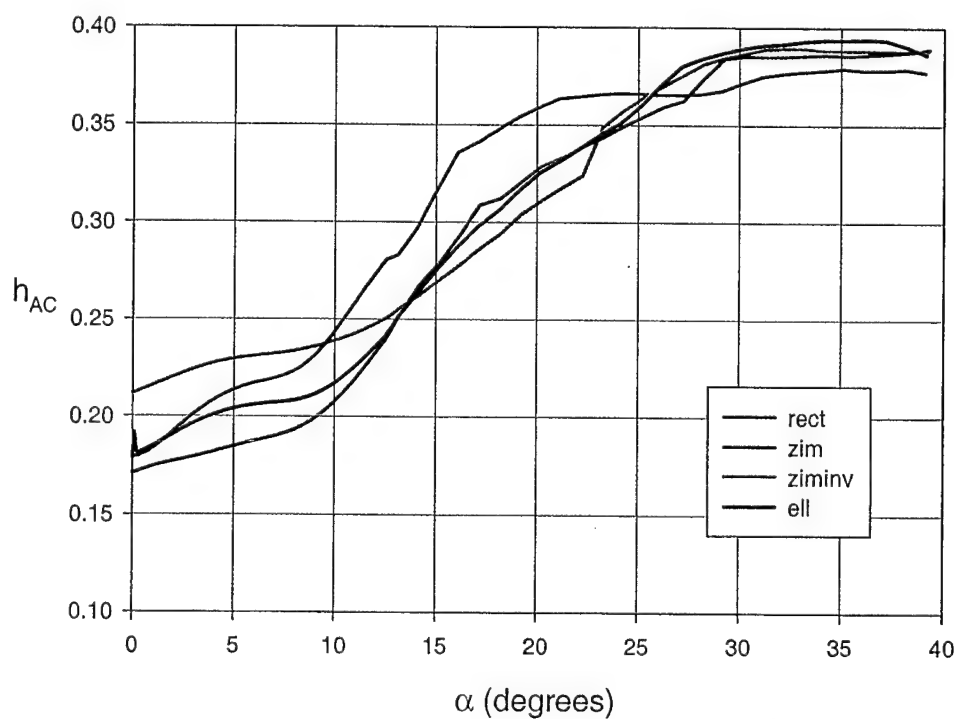


Figure 3.16: h_{AC} vs. α , $AR = 1.50$, $Re_c = 140,000$

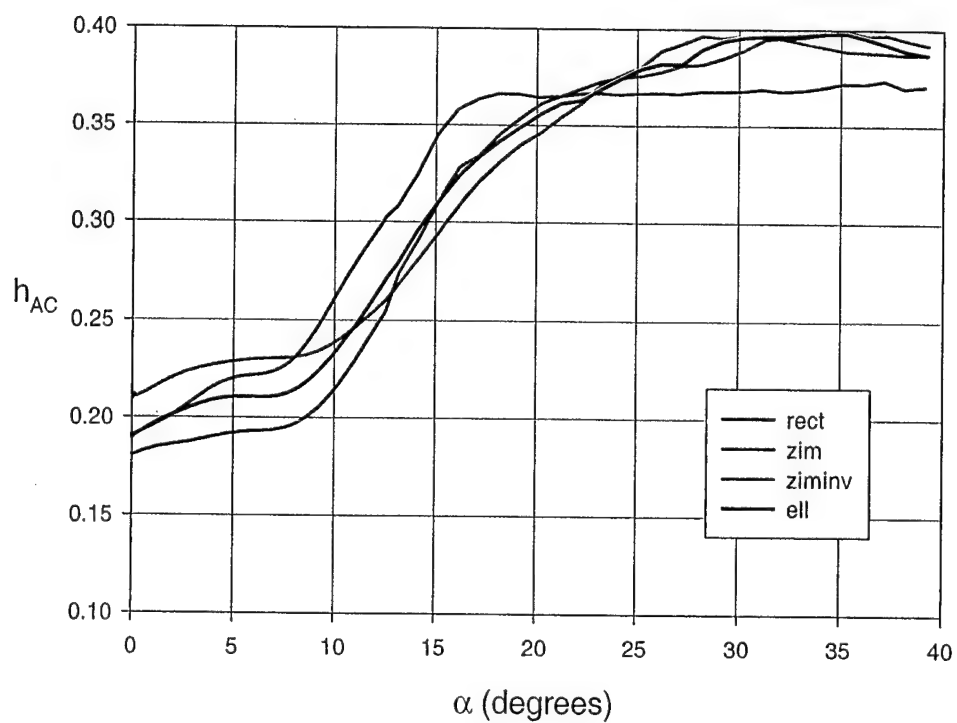


Figure 3.17: h_{AC} vs. α , $AR = 1.75$, $Re_c = 140,000$

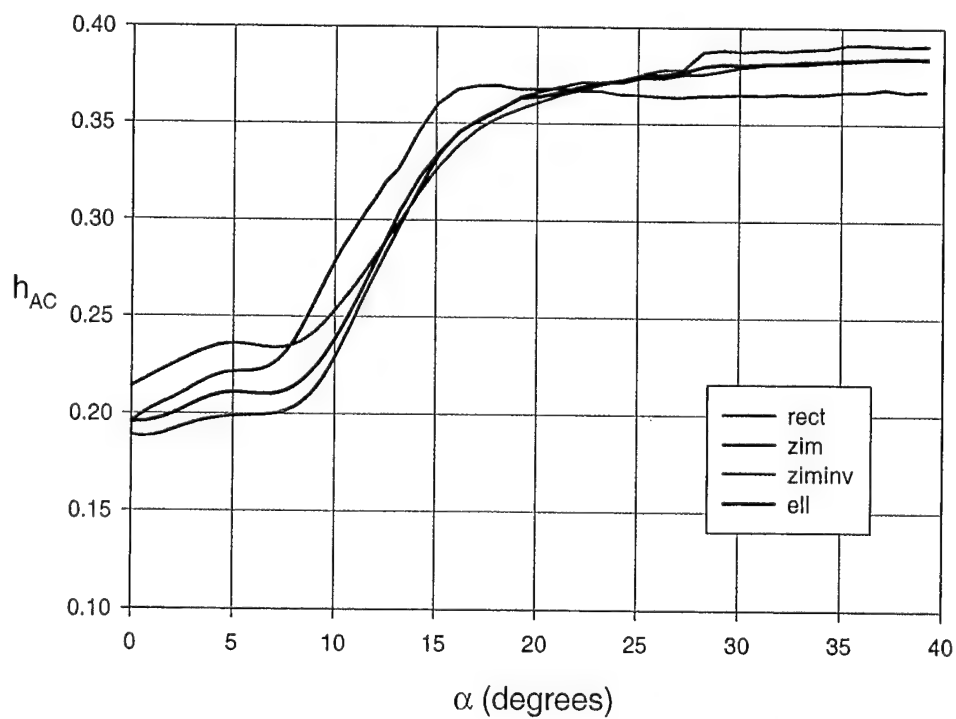


Figure 3.18: h_{AC} vs. α , $AR = 2.00$, $Re_c = 140,000$

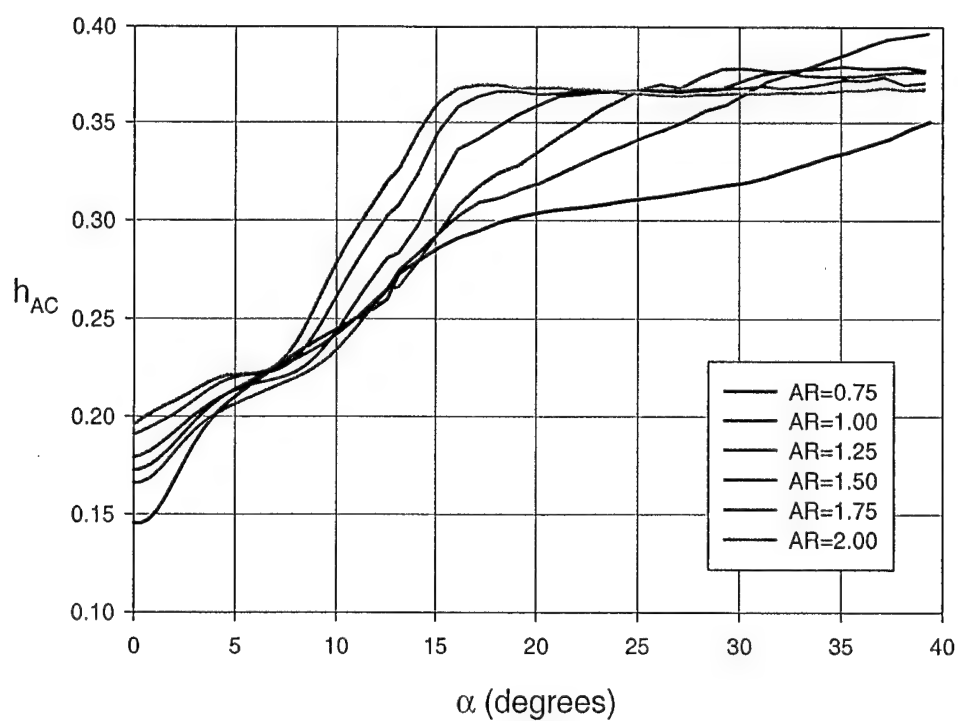


Figure 3.19: h_{AC} vs. α , rectangular planform, $Re_c = 140,000$

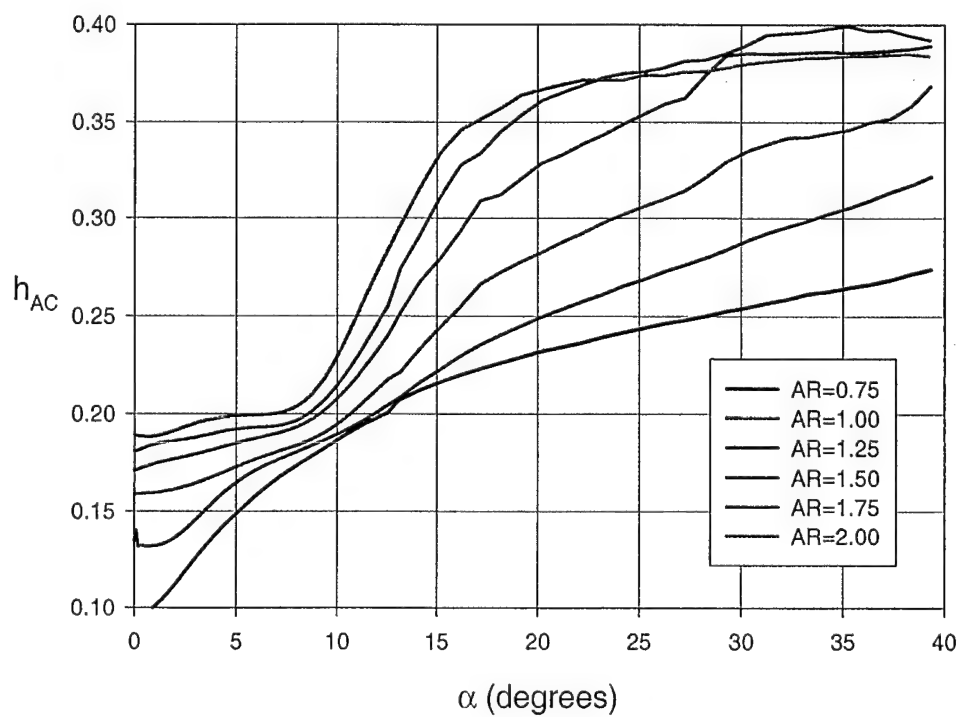


Figure 3.20: h_{AC} vs. α , Zimmerman planform, $Re_c = 140,000$

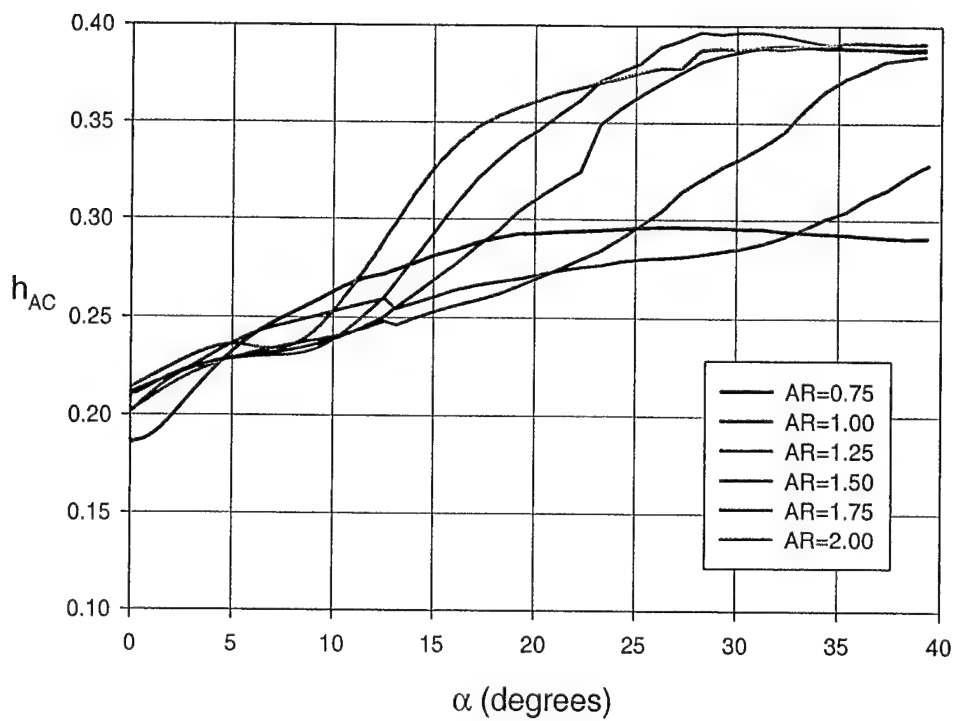


Figure 3.21: h_{AC} vs. α , Inverse Zimmerman planform, $Re_c = 140,000$

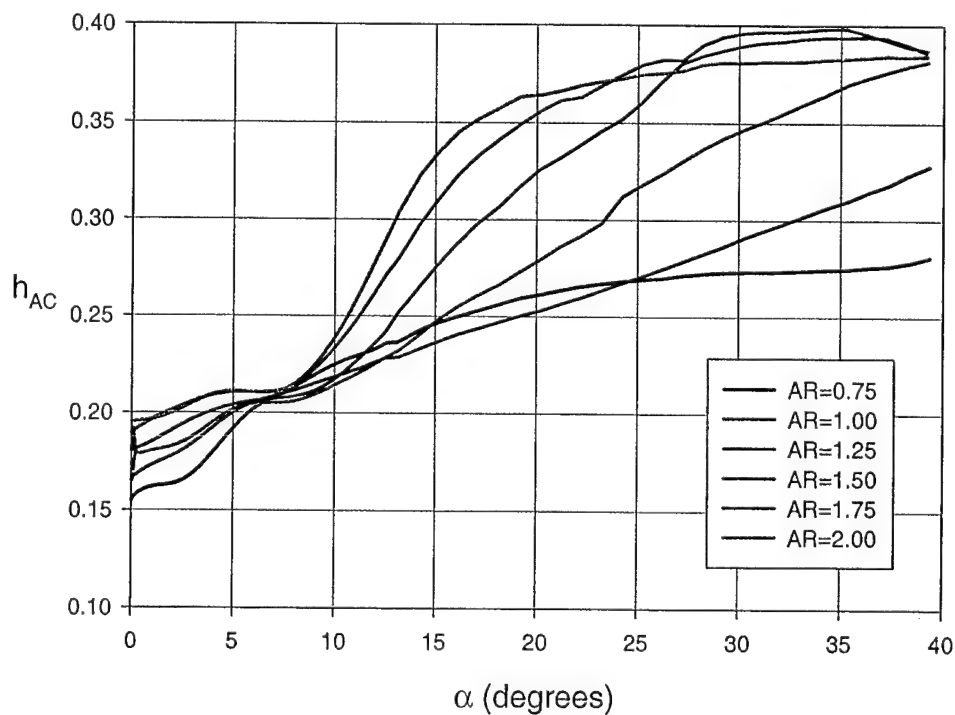


Figure 3.22: h_{AC} vs. α , Elliptical planform, $Re_c = 140,000$

3.4 Effect of Reynolds Number

The effect of varying Reynolds number on the lift and drag coefficients of LAR wings at low Re are generally small. In most cases, the most significant effect of Reynolds number is associated with the maximum lift coefficient and stall angle of attack. Figures 3.23 to 3.26 plot results corresponding to the rectangular planform of AR 0.5, 1.0, and 2.0 at two different values of Re . The trends observed for these particular cases are similar to those seen in all other planforms and aspect ratios. It can be seen that both lift and drag coefficients increase as the Reynolds number increases. Analysis of Figure 3.25 reveals that except for angles of attack near stall, the effect of Reynolds number is within uncertainty bounds of the data. This figure also shows most clearly the increase in stall angle of attack, specially on the lower aspect ratio cases.

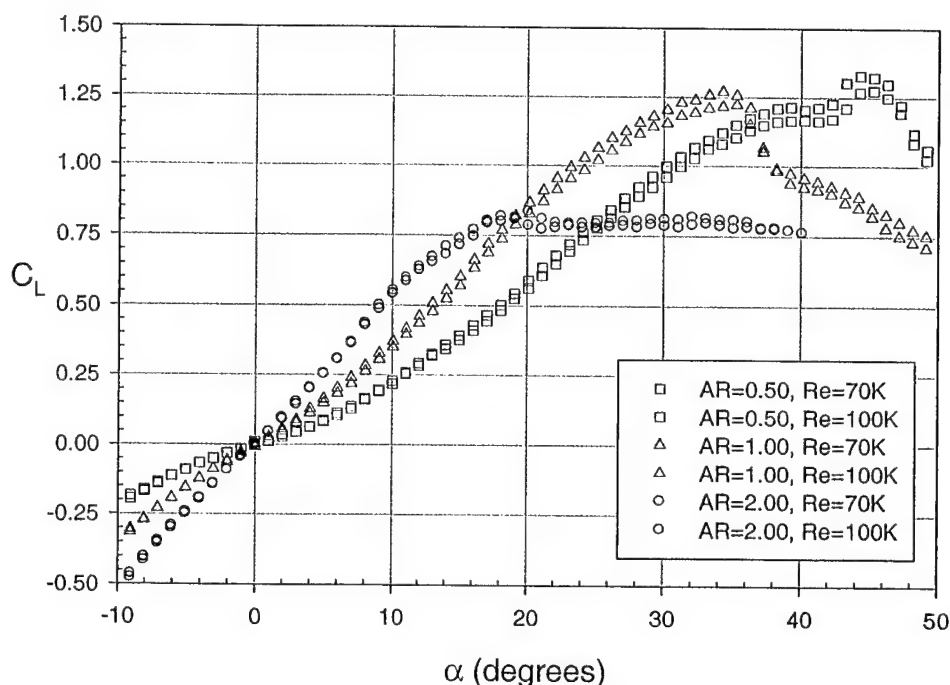


Figure 3.23: C_L vs. α , Rectangular Planform, Effect of Re

3.5 Effects of Camber

A series of experiments were also conducted that studied the effect of camber on LAR wings. Brown [21] provides a more detailed set of results than available in this report. Figures 3.27 through 3.30 reveal some general trends. In these experiments, some of the planform shapes presented in Chapter 2 were modified to have 4% circular camber. Based on the results shown in the figures of this section, the following conclusions about the effect of camber can be stated:

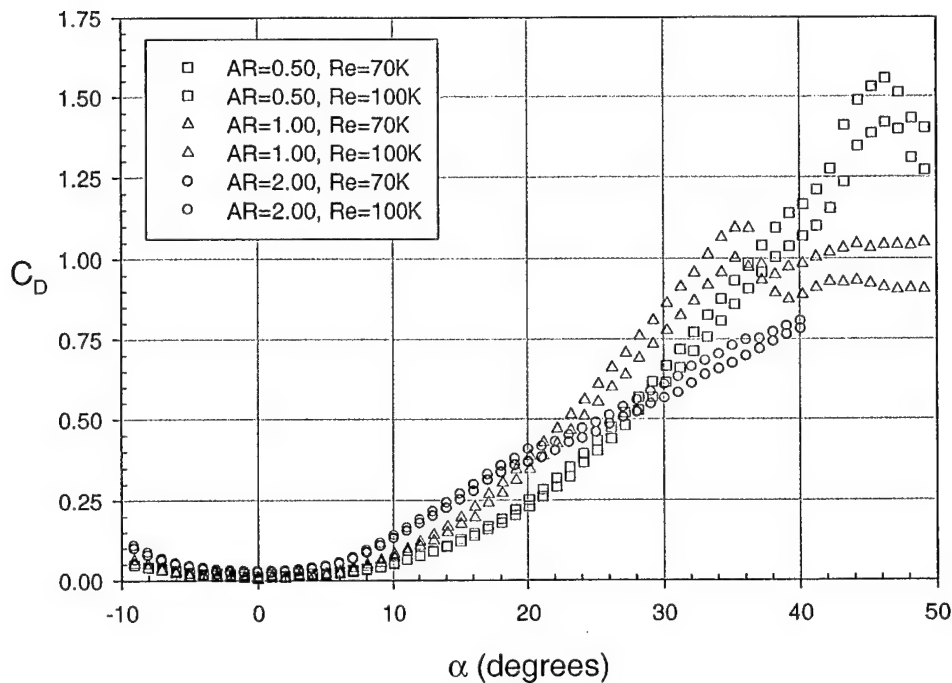


Figure 3.24: C_D vs. α , Rectangular Planform, Effect of Re

1. Wings with camber had higher lift and lower drag, yielding significantly more efficient lifting configurations than those of their uncambered counterparts
2. The angle of attack at stall and the maximum lift coefficient were seen to increase dramatically in the case of cambered wings
3. The most significant improvement of aerodynamic efficiency by means of addition of camber was seen to occur for the wings of aspect ratio 2.00. The performance improvement (in terms of lift-drag polar) of wings of lower AR was not as large.

In general, all experimental results point to the conclusion that LAR wings at low Re benefit from camber just as much as wings of high aspect ratio at higher operating Reynolds numbers.

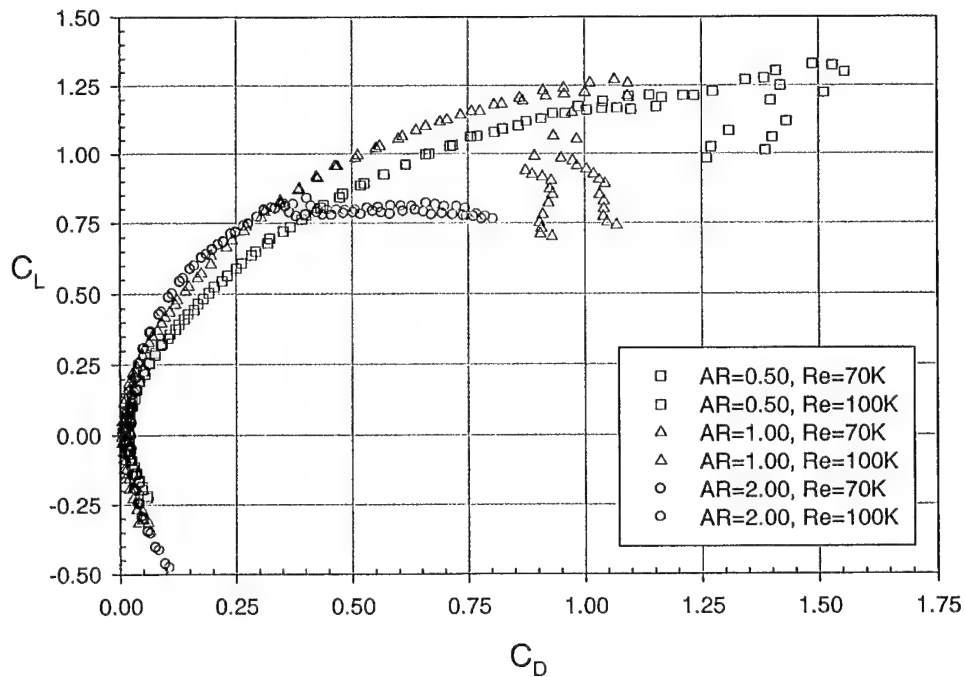


Figure 3.25: C_L vs. C_D , Rectangular Planform, Effect of Re

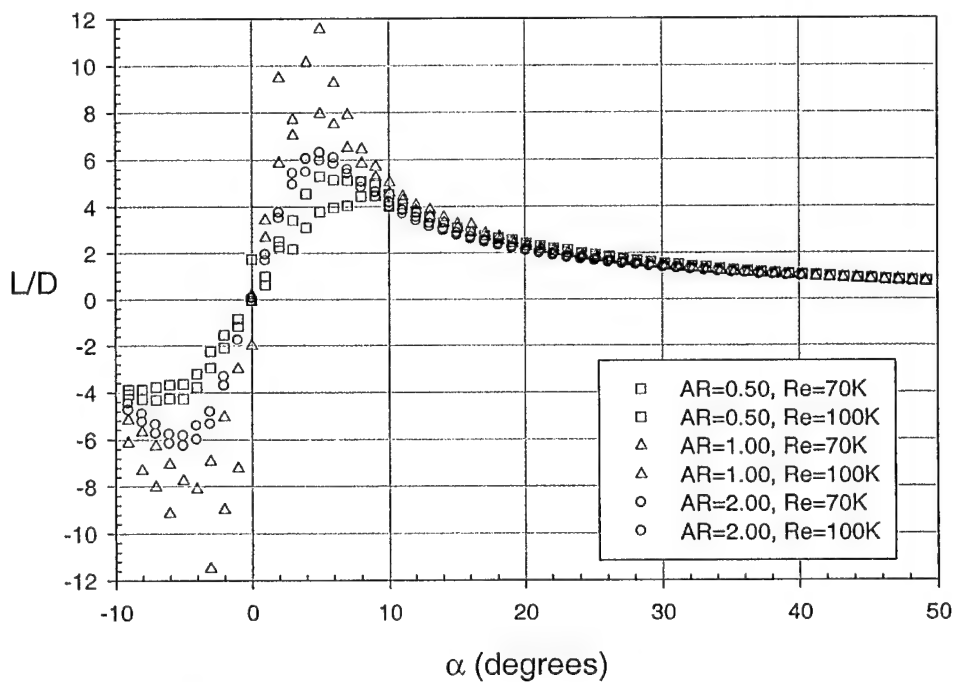


Figure 3.26: L/D vs. α , Rectangular Planform, Effect of Re

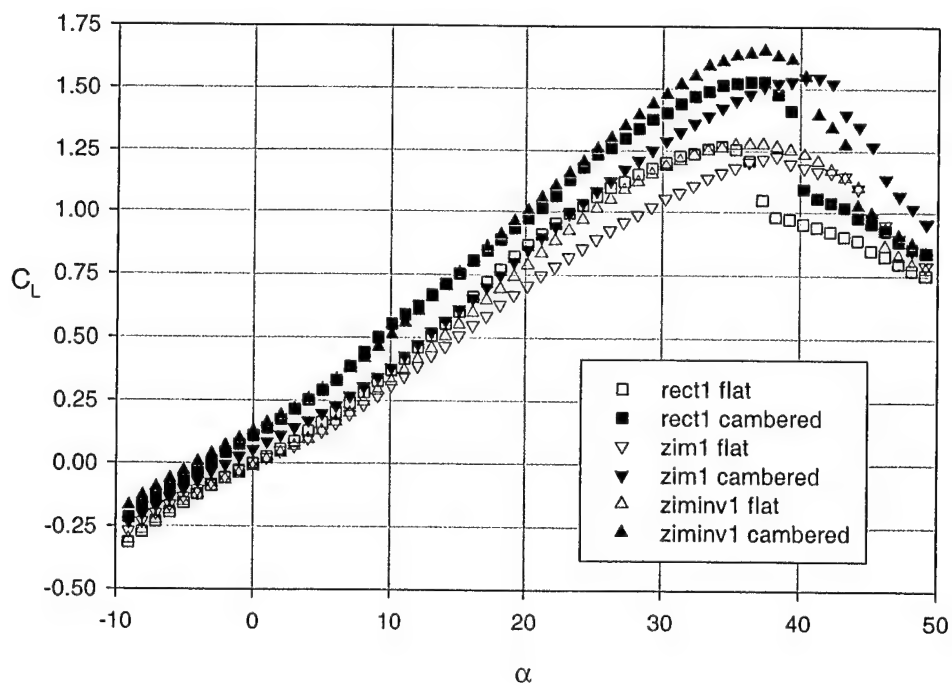


Figure 3.27: C_L vs. α , $AR = 1.00$, Effect of Camber

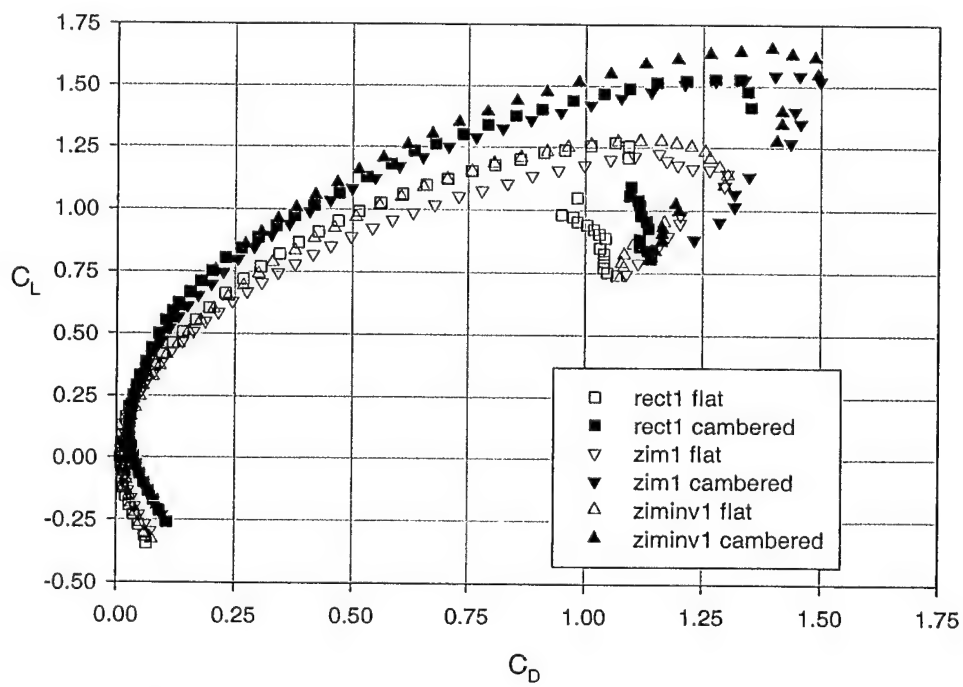


Figure 3.28: C_L vs. C_D , $AR = 1.00$, Effect of Camber

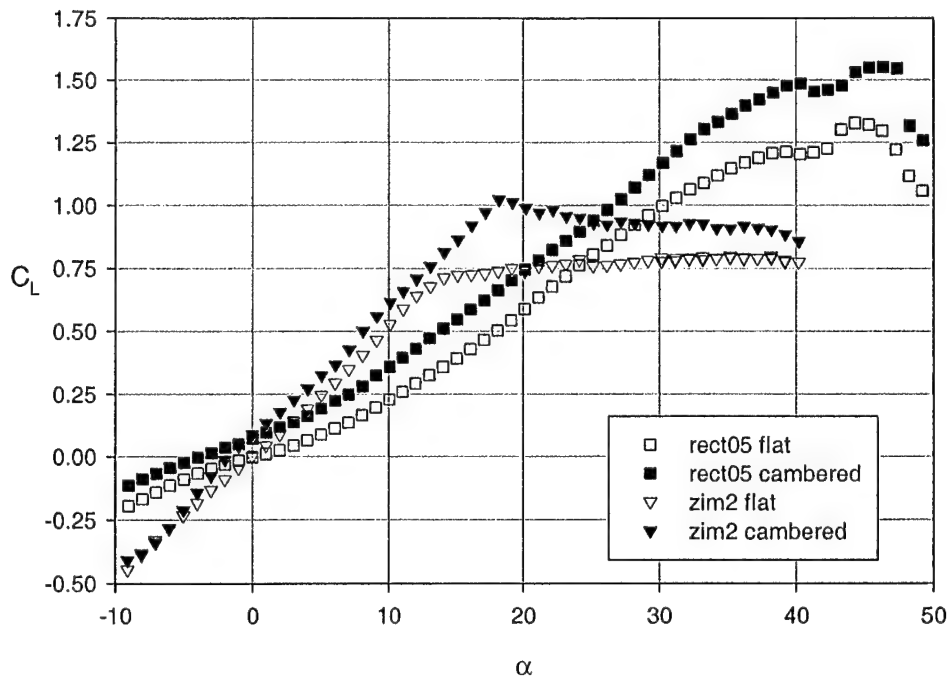


Figure 3.29: C_L vs. α , $AR = 0.50$ and 2.00 , Effect of Camber

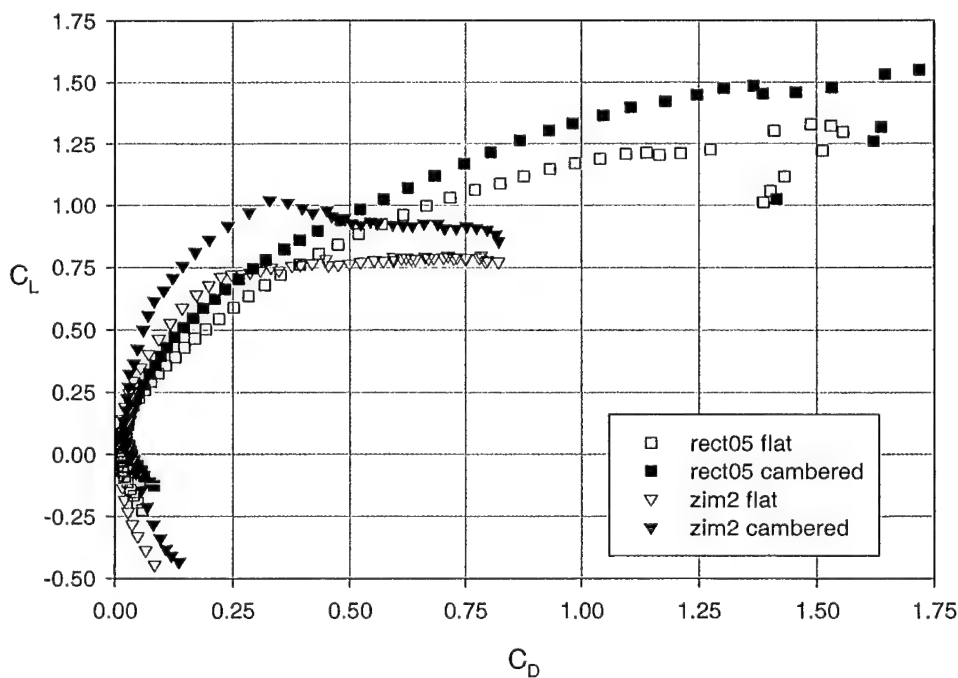


Figure 3.30: C_L vs. C_D , $AR = 0.50$ and 2.00 , Effect of Camber

3.6 Effects of Leading Edge Shape

A preliminary study of the effects of leading edge shape was conducted. The objective of this study was to determine whether leading edge shape should be looked at more closely in future research projects. This analysis also reveals how sensitive a MAV's performance is to the shape of the leading edge and how much care must be taken in the manufacture of wings. The experimental results presented in this section correspond to a rectangular wing of $AR = 2.00$ at Reynolds numbers of 100,000 and 200,000. The wing has either of three leading edge shapes: 5-to-1 elliptical, 10° wedge, or 20° wedge. Depending on the orientation of the wing (right side up or upside down), each of the wedge leading edge shapes is actually two distinct geometries (see Figure 3.31).

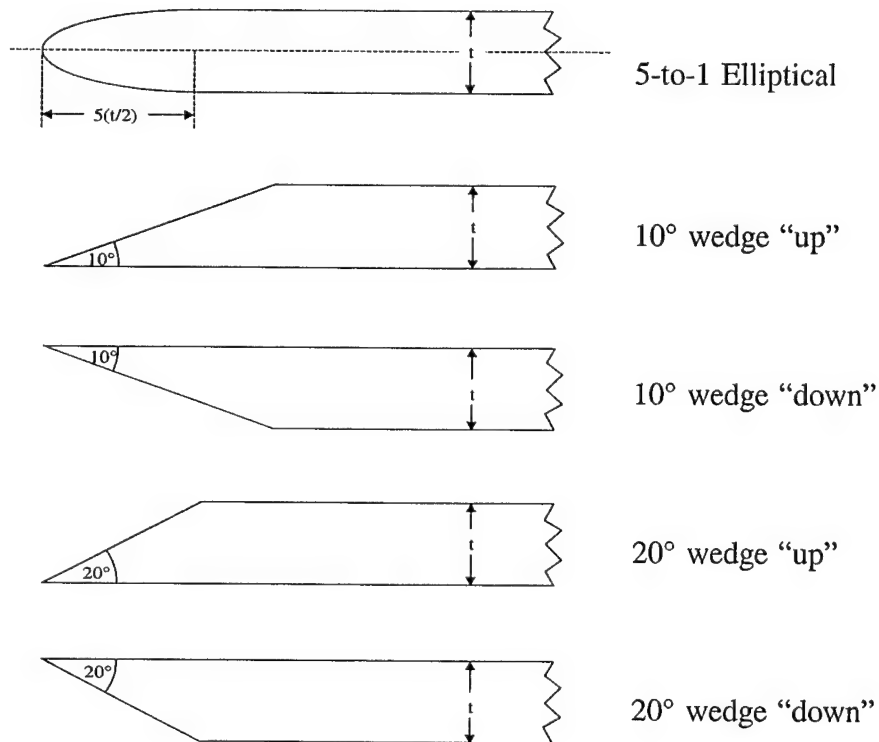


Figure 3.31: Leading Edge Geometries

Figures 3.32 and 3.33 shows plots of the normal force coefficient and pitching moment coefficient about the quarter-chord as a function of angle of attack for the AR 2.0 rectangular planform. The effect on C_N is not very large. In many cases, differences in normal force coefficient between one leading edge and another lie within uncertainty bounds of the experimental data. The most significant change in C_N is visible at stall. The stall angle and maximum normal force coefficient for the wings with "down" leading edges is much lower than that of the wings with "up" leading edges. This is expected as the "down" leading edges form an extremely sharp geometry on the upper surface of the wing. As such, flow separation occurs earlier.

In contrast, the effect on the moment coefficient is quite large at all angles of attack. Particularly interesting in Figure 3.33 is the shift of the angle of attack at which the moment coefficient

begins to decrease. We will define an angle of attack α_{peak} as the α at which the moment coefficient reaches a maximum. As an example, for the 10° "down" leading edge at $Re = 100,000$, $\alpha_{\text{peak}} = 4.5^\circ$. For both "down" leading edges, C_M has an α_{peak} near $\alpha = 4.5^\circ$. For the 10° "up" leading edge, α_{peak} is near $\alpha = 8.5^\circ$ while for the 20° "up" leading edge, α_{peak} is closer to $\alpha = 10^\circ$. It is proposed that the reason for this shift in α_{peak} is due to flow separation. For the "up" leading edges, an adverse pressure gradient (in the geometric sense) on the upper surface of the wing does not exist until the angle of attack goes beyond the angle of the leading edge wedge. Thus, it is expected that the flow will remain attached to the upper surface up until that angle. For the "down" leading edges, separation is expected to occur immediately because the wedge angle is essentially zero. Evidence for the proposed explanation can be seen in the curves of Figure 3.33. The correlation is not perfect, as exemplified by the fact that α_{peak} does not occur at 20° for the 20° wedge. Nevertheless, a trend definitely exists that links the angle of inclination of the leading edge's upper surface and the value of α_{peak} .

Another interesting result of Figure 3.33 is the effect of Reynolds number on α_{peak} . For all the geometries shown in this figure (except for the 10° "down" one), a jump in the C_M vs. α curve occurs as the Reynolds number increases from 100,000 to 200,000 (for example, this jump occurs at $\alpha = 1.75^\circ$ for the elliptical leading edge).

The observations and proposed explanations provided in this section are preliminary. Not enough experimental data is available to thoroughly explain the effects of leading edge shape. One sure conclusion of this phase of the project is that further study of leading edge influence on aerodynamic characteristics should be made in the future. Such a study is beyond the scope of the present work. Future research at the Hessert Center for Aerospace Research could focus on this aspect of LAR wing aerodynamics.

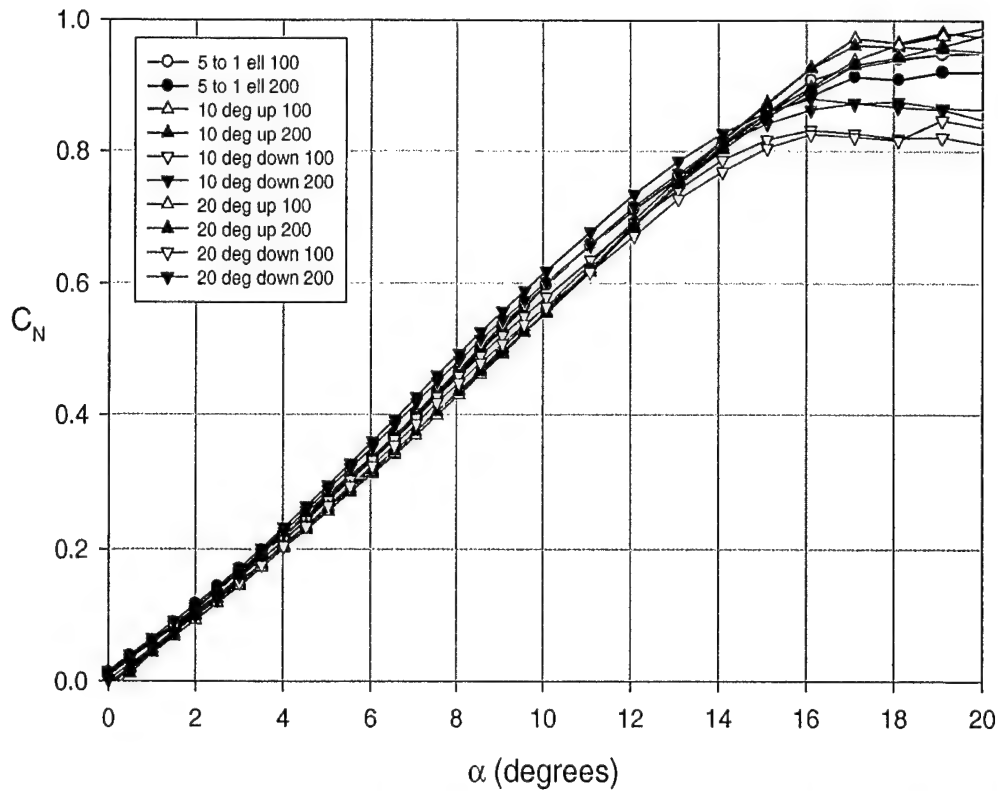


Figure 3.32: Effect of Leading Edge Shape on C_N , Rectangular Planform $AR = 2.0$

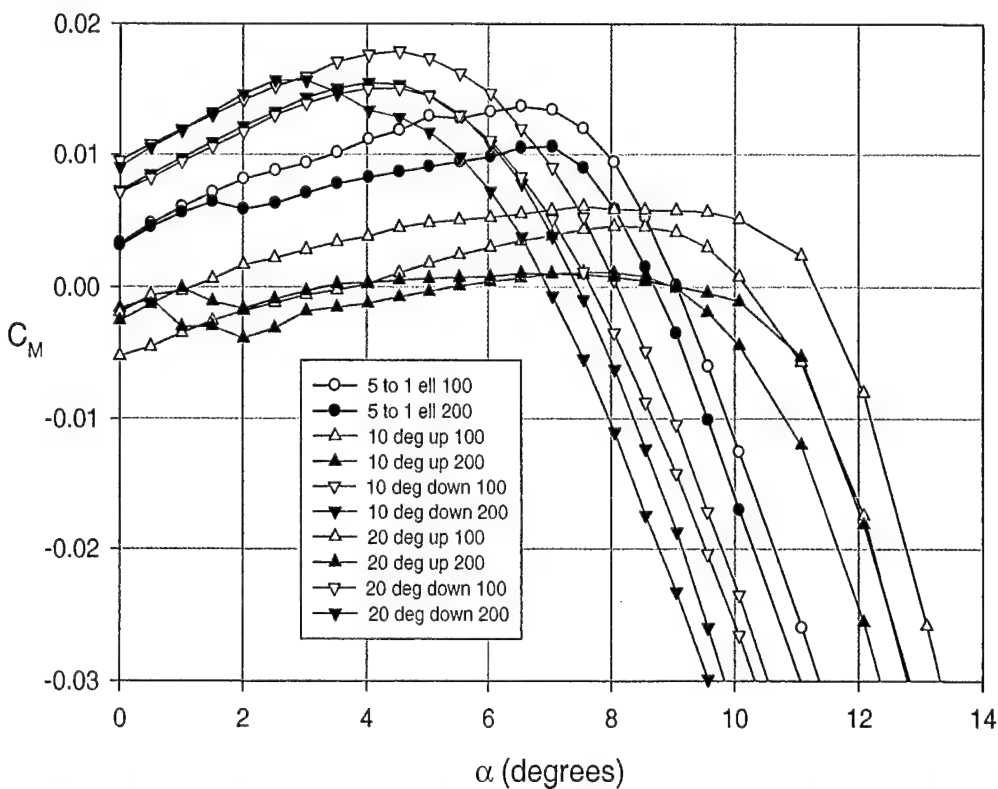


Figure 3.33: Effect of Leading Edge Shape on C_M , Rectangular Planform $AR = 2.0$

Chapter 4

Design-Optimization Part I: Design Variables and Optimization Algorithm

4.1 Introduction to MAV Design-Optimization

The previous chapters of this report have summarized wind tunnel data for wings with the following criteria:

1. Four distinct planforms (*rect*, *zim*, *ziminu*, *ell*).
2. Seven values of aspect ratio (0.50, 0.75, 1.00, 1.25, 1.50, 1.75, and 2.00).
3. Three values of Reynolds numbers (70,000, 100,000, and 140,000).
4. Two values of camber (0% and 4%).
5. Three fuselage-body configurations (no fuselage-body and two rounded bodies with different fineness ratios).

The data consists mostly of curves of C_L , C_N , C_D , and C_M versus angle of attack for each wing planform, aspect ratio, and Reynolds number combination. The location of the aerodynamic center of any of the wings tested as a function of angle of attack can be determined using this same data.

It is important to stress that this wind tunnel data is directly applicable to real world aerodynamic design problems. The data itself does not yield much practical information unless it is incorporated into some type of useful aerodynamic analysis tool. This is the objective of the next two chapters. In this chapter, an example design challenge typical to MAV applications is introduced. After appropriate restrictions are imposed, the design variables and aircraft performance characteristics are defined. The design problem is well suited to the use of optimization algorithms. Therefore, a genetic algorithm global optimization technique is suggested to solve the problem. The next chapter shows how the experimental data obtained in this work can be incorporated into an aerodynamic analysis procedure applicable to MAVs. This analysis tool is used in the optimization program in order to generate optimum designs.

The application presented in the next two chapters is by no means meant to be a final product or to represent the only possible use of the wind tunnel data. It is meant to show how useful engineering decision-making tools can be extracted from wind tunnel data.

4.2 Design Problem Statement

4.2.1 Summary of Design Optimization Problem

The design problem considered in this chapter incorporates requirements and mission objectives that are common to many current MAV implementations. Even though mission objectives vary greatly depending on the application and (sometimes more importantly) on the end user, many MAV missions share common characteristics. In the discussions that follow, the design problem is defined to be the following:

The designer is presented with the challenge of developing the **smallest** remote-controlled air vehicle that:

- a) can carry a wireless video transmitter/video camera payload,
- b) has an endurance of at least 10 minutes and a surveillance range of at least 0.8 *Km* (0.5 *mi*) and
- c) is maneuverable enough to be able to capture an image of a target on the ground.

The size of the vehicle is defined explicitly as the maximum linear dimension between any two points located on the aircraft while it is airborne.

4.2.2 Detailed Mission Requirements

The mission requirements listed above can be further analyzed in order to obtain more quantitative design objectives. These are:

Video Payload: The MAV must be able to carry video components that have a range of at least 0.8 *Km* (0.5 *mi*). Video components that satisfy these specifications can be selected from off-the-shelf components and thus their dimensions and weights are known.

Range/Endurance: For the purposes of this example problem, the propulsion system of the MAV is restricted to be an internal combustion engine. The particular engine was chosen based on the expected takeoff weight of the MAV. The fuel consumption of the engine is known from engine tests; therefore, the required fuel weight needed for an endurance of 10 minutes can be calculated directly.

Stability and Control: The airplane should be able to cruise in a trimmed flight condition (that is, the pitching moment about the center of gravity should be close to zero). Also, the pitching moment derivative with respect to angle of attack at cruise must be negative in sign (longitudinal stability requirement). For control, the airplane must carry control surface actuators (servos), a remote-control radio receiver, and batteries (which power both the control system and the video system). These components are also predefined and their weights and dimensions are known.

4.2.3 Restrictions

Certain restrictions must be placed on the aircraft in order to apply the semi-empirical analysis procedure and in order to simplify the design process. These restrictions are:

Fixed Wing: The MAV is restricted to a fixed-wing aircraft that may or may not have a horizontal stabilizer. The results section of this chapter discusses the complications arising in tail-less airplane configurations. However, for the present work, the optimizer is allowed to select a design set that has zero horizontal tail area.

Wing and Tail Thickness, Camber, and Edge Shape: The main aerodynamic analysis is based on the interpolation of wind tunnel data of low aspect ratio, flat-plate wings (details of this procedure are given in Section 5.1.1). As such, the wing and tail surfaces must be restricted to zero-camber, a thickness to chord ratio of 1.96%, and 5-to-1 elliptical leading and trailing edges so that they match the parameters of the wing models used in the experiments.

Vertical Location of Tail: It is assumed that if a tail is present, the tail is located behind the wing (not a canard configuration). In addition, the tail is restricted to be located below the wing. The vertical separation between the wing and tail is set equal to the fuselage height. The reason for this restriction is that flight-testing of a variety of MAV configurations has revealed that significantly more stable flight can be achieved if the horizontal tail is located well clear of the wing wake.

Tractor Configuration: The engine is assumed to be at the nose of the airplane in a tractor configuration.

Predefined Components: The main components of the MAV (engine, propeller, fuel tank, batteries, video transmitter, video camera, RC receiver, and RC servos) have been selected based on commercially available products that are as small and light as possible but still satisfy mission requirements. This restriction is particularly important in terms of the engine because in traditional airplane design procedures, the selection of the propulsion system is part of the design process.

Fixed Take-off Weight: Since the components to be carried by the MAV are predefined, the size of the fuselage that will house the components is also essentially fixed. The fuselage is the largest contributor of structural weight of an MAV; therefore it is possible to approximately define a fixed take-off weight that includes the component weights as well as estimates for the structural weights of the fuselage, wing, tail, vertical stabilizer, and miscellaneous accessories (linkages, hinges, switches, wiring, etc.). The fixed value of takeoff weight W for the MAV to be designed in this report is 1.0 Newton (0.22 lb), equivalent to a mass of approximately 100 g (3.52 oz).

4.3 Design Variables, Design Parameters, and Aircraft States

4.3.1 Design Variables

For an MAV with the configuration limitations mentioned above, the design variables are defined as follows:

Variable	Symbol	Type
Main Wing		
Wing Planform	P_W	Discrete
Aspect Ratio	AR_W	Continuous
Planform Area	S_W	Continuous
Incidence Angle	i_W	Continuous
Horizontal Tail		
Tail Planform	P_T	Discrete
Aspect Ratio	AR_T	Continuous
Planform Area	S_T	Continuous
Incidence Angle	i_T	Continuous
Position Variables		
Location of Tail	x_T	Continuous
Location of Propeller	x_{prop}	Continuous
Aircraft Angle of Attack		
Aircraft Angle of Attack	$\tilde{\alpha}$	Continuous

Table 4.1: Design Variables

Wing and tail variables which are treated as constants in this example are the thickness to chord ratio (1.96%), percent camber (0%), and leading and trailing edge shape (5-to-1 elliptical shape). As mentioned before, the reason for fixing these four variables as constant is that wind tunnel data is used in the primary aerodynamic analysis through an interpolation procedure. In order to match the experiment data with the design variables of the MAV, these four parameters are set equal to those of the experiments.

Note that the planform of the wing and tail is defined as being a discrete variable. This is due to the fact that the wind tunnel data used in the main aerodynamic analysis includes only four wing planforms. The shape parameters associated with these planforms are not evenly spaced and thus do not offer a simple way of fitting a response surface based on wing shape. Therefore the wing and tail are allowed only four possible shapes. Nevertheless, the wing area and aspect ratio are truly continuous variables and their aerodynamic performance *can* be interpolated.

The location variables x_T and x_{prop} determine the location of the horizontal tail and propeller in the streamwise direction. These two variables alone define the placement of all other components due to restrictions placed on the relative location of components inside the aircraft. Section 5.3 provides details of these restrictions and how they affect the aircraft's center of gravity.

Finally, the vertical position of the wing and tail is not defined as a design variable but is considered a parameter instead. See Section 5.4.1 for an explanation of how the values of vertical distance between the wing/tail and the fuselage centerline (z_W and z_T , respectively) are assigned.

4.3.2 Design Parameters

Design parameters are those design elements that cannot be directly controlled by the designer. For the example design problem considered in this report, the design parameters can be sub-classified into either component parameters or operational parameters:

Component Parameters: The component parameters include the size, weight, and center of mass of the components to be carried on board (engine, propeller, fuel tank, batteries, two servos, radio control receiver, video transmitter, and video camera). The geometry and mass-distribution of these components (given in Appendix B) are inputs to the overall design process. Furthermore, the total takeoff weight of the aircraft is assumed to be constant and known [equal to 1.0 Newtons (0.22 lb)].

Also included in this category is the performance of the engine to be used for the MAV. Experiments with this engine have yielded curves of thrust versus freestream velocity. This information is used in the determination of the cruise speed.

Finally, the weight density of the material used to construct the wing and tail is also considered a component parameter and is used in center of gravity calculations. The MAV prototypes constructed at Notre Dame over the last few years have been made using 0.3175 cm (1/8 in) foam and it is assumed that this is the material of choice for the design considered in this report.

Operational Parameters: The principal operational parameters are air density and freestream velocity, which are needed for converting non-dimensional coefficients into forces. Density is a user-supplied value while freestream velocity is calculated iteratively within the analysis program as described in Section 5.2.2. Other operational parameters could be air viscosity or wind speed; however these secondary operational parameters are not considered in this report.

4.3.3 Aircraft States (Performance)

The main states of an MAV design are the maximum dimension, the total lift force generated, and the overall pitching moment and trim characteristics. In more detail, these states are:

Maximum Dimension: The maximum dimension of a given design depends on the size, aspect ratio, and shape of the wing and tail, the location of these two surfaces, and the location of the propeller (from which the position of all other components is derived). Section 5.5 discusses the details of the determination of maximum dimension.

Total Lift: The total lift generated by the aircraft is dependent on the size, aspect ratio, shape, and incidence angle of the wing and tail, angle of attack of the aircraft, and on the cruise velocity. The total lift force acting on the airplane must be equal to the takeoff weight of the MAV, W (within some threshold). In addition, the angle of attack of the wing and tail should be lower than the stall angle of attack for each lifting surface. In general, the cruise angle of attack is desired to be much smaller than the stall angle of attack to allow for maneuvering. This additional angle is defined here as $\tilde{\alpha}_{\text{safety}}$.

Pitching Moment: The moment about the center of gravity must be equal to zero (or within ϵ_2 of zero) for steady cruise flight. Also related to pitching moment is the requirement that the derivative of pitching moment with respect to angle of attack be negative in sign.

4.4 Optimization Problem

4.4.1 Statement of Optimization Problem

The discussion in the previous sections provides a preliminary basis for stating the complete design/optimization problem related to the design of a micro air vehicle in standard optimization form. The constraints have been converted into less than or equal constraints in order to facilitate the use of optimization algorithms.

Objective Function:

Maximum dimension of the MAV, $D_{\max} \implies$ to be **minimized**.

Design Variables:

$$\underline{x} = [P_W, AR_W, S_W, i_W, P_T, AR_T, S_T, i_T, x_T, x_{\text{prop}}, \tilde{\alpha}]^T$$

Subject to the Constraints:

$$\begin{aligned} \|W - L_{\text{total}}\| &\leq \epsilon_1 \\ \tilde{\alpha} + i_W + \tilde{\alpha}_{\text{safety}} - \alpha_{\text{stall}_W} &\leq 0 \\ \tilde{\alpha} + i_T + \tilde{\alpha}_{\text{safety}} - \alpha_{\text{stall}_T} &\leq 0 \\ \|M_{\text{CG}}\| &\leq \epsilon_2 \\ \frac{\partial M_{\text{CG}}}{\partial \tilde{\alpha}} &\leq 0 \end{aligned}$$

4.4.2 Design Variable Constraints

The design variables are constrained to satisfy the following requirements:

$$\begin{aligned} P_{W_{\min}} &\leq P_W \leq P_{W_{\max}} \\ AR_{W_{\min}} &\leq AR_W \leq AR_{W_{\max}} \\ S_{W_{\min}} &\leq S_W \leq S_{W_{\max}} \\ i_{W_{\min}} &\leq i_W \leq i_{W_{\max}} \\ P_{T_{\min}} &\leq P_T \leq P_{T_{\max}} \\ AR_{T_{\min}} &\leq AR_T \leq AR_{T_{\max}} \\ S_{T_{\min}} &\leq S_T \leq S_{T_{\max}} \\ i_{T_{\min}} &\leq i_T \leq i_{T_{\max}} \\ x_{T_{\min}} &\leq x_T \leq x_{T_{\max}} \\ x_{\text{prop}_{\min}} &\leq x_{\text{prop}} \leq x_{\text{prop}_{\max}} \\ \tilde{\alpha}_{\min} &\leq \tilde{\alpha} \leq \tilde{\alpha}_{\max} \end{aligned}$$

4.4.3 Genetic Algorithm

4.4.3.1 Summary of Genetic Algorithm

The MAV design-optimization problem described thus far is a highly nonlinear design problem with many design variables. Therefore it lends itself to nonlinear global optimization methods such as simulated annealing or genetic algorithms. A genetic algorithm (GA) method will be used in this work; it is implemented following the description of Belegundu [22]. Genetic algorithms are applicable for the maximization of a function $f(\underline{x})$ (where \underline{x} is the vector containing the design variables x_1, x_2, \dots, x_N) subject to upper and lower bounds on \underline{x} (that is, $\underline{x}_{min} \leq \underline{x} \leq \underline{x}_{max}$). A brief description of the algorithm follows:

1. Each continuous design variable x_i is represented as a binary number of m_2 bits. The interval of said design variable ($x_{max_i} - x_{min_i}$) is therefore partitioned into $(2^{m_2} - 1)$ sub-intervals. A special case exists for the two discrete variables P_W and P_T (the planforms of the wing and tail). These variables can only take four values: 1, 2, 3, or 4, each representing one of the four planforms tested in wind tunnel experiments. A convenient way to represent these discrete design variables is to define the number of bits for P_W and P_T to be equal to $m_1=2$. This automatically allows only four possible conditions. The number of bits of the other continuous variables (m_2) is still a parameter at the control of the user.
2. A population of Z members is created by attaching the binary representation of each x_i end to end. As an example, one member of a population with $m_2 = 8$ would have $8N$ bits and would look as follows:

$$\underbrace{101101010100111100110101}_{x_1} \dots \underbrace{11101010}_{x_N}$$

The number of members in a population usually varies between 10 and 200. Note that the example above ignores the complication of the discrete variables having a different number of bits than the number of bits of the continuous variables. The two discrete variables use $m_1=2$ bits while the continuous variables use $m_2=8$ bits. For this case, the binary representation of a population member would be:

$$\underbrace{10}_{x_1} \underbrace{101101010100111100110101}_{x_2} \underbrace{11}_{x_3} \underbrace{10010101}_{x_4} \dots \underbrace{11101010}_{x_N}$$

Note that the number of bits in a member of the population for the discrete variable case is $N_{bits} = [2m_1 + m_2(N - 2)]$

3. An initial population is selected using a random number generator that randomly selects a 1 or a 0 for each of the N_{bits} bits in each member of the population.
4. Each member of the population is converted from a string of 1's and 0's into N design variables x_1, x_2, \dots, x_N by transforming the binary representation into actual values.
5. The function value f is evaluated for each set of design variables \underline{x} corresponding to each member of the population.

6. A mating pool is created such that the members of the population whose function value is greater have a greater probability of “reproducing”. This is done as follows:

- (a) The maximum and minimum values of f in the population (f_h and f_l) are used to define two parameters C and D :

$$C = 0.1f_h - 1.1f_l \quad (4.1)$$

$$D = \max(1, f_h + C) \quad (4.2)$$

- (b) The function values f_i for each member of the population are then scaled using C and D :

$$f'_i = \frac{f_i + C}{D} \quad (4.3)$$

- (c) The parameter S is defined as $S = \sum f'_i$ for $i = 1 \dots Z$.
 (d) A random number r between 0 and 1 is generated Z times. Each time, the index j is found such that

$$\sum_{i=1}^{j-1} f'_i \leq rS \leq \sum_{i=1}^j f'_i \quad (4.4)$$

The j th member of the population is copied into the mating pool.

- (e) If desired, the procedure for selecting the mating pool can be modified such that the first N_{best} members of a given population are guaranteed to be in the mating pool. The procedure outlined above would then be used for the remaining members of the mating pool.

7. Crossover is performed as follows:

- (a) Two members of the mating pool population are selected to be “parents”.
 (b) A random number k between 1 and N_{bits} is generated.
 (c) The first k bits of the two parents are exchanged and they become the first k bits of the “children”. The remaining bits of the children are copied from those of the parents. As an example, the following crossover operation would take place if k is randomly determined to be 13:

```
parent1  1001001010101 01010001010...
parent2  0100100110111 11110100101...
child1   0100100110111 01010001010...
child2   1001001010101 11110100101...
```

- (d) The crossover operation is performed $Z/2$ times, generating a new child population with Z members.

8. Mutation is accomplished by pre-defining a mutation probability b_p . Every time that a crossover operation is performed, a random number r_m is selected between 0 and 1 for each of the N_{bits} bits of each child. If $r_m \leq b_p$, then the bit is changed to a 0 if it was a 1 or to a 1 if it was a 0.
9. The function value is evaluated for each member of the new child population. Steps 6 through 8 are repeated N_{GEN} times (equal to the number of generations).

4.4.3.2 Penalty Functions

The MAV optimization problem must be converted from a constrained minimization problem to a form that is applicable to the GA method. This requires the use of penalty functions to represent the constraints of the problem. The five constraints (lift constraint, wing/tail stall angle constraints, trimmed flight constraint, and longitudinal stability constraint) are converted to penalty functions as follows:

1. Lift Constraint: $\|W - L_{\text{total}}\| \leq \epsilon_1$

A penalty function P_1 is defined such that:

$$P_1 = (W - L_{\text{total}})^2 \quad (4.5)$$

2. Stall Angle of Attack Constraint: $\tilde{\alpha} + i_X + \tilde{\alpha}_{\text{safety}} - \alpha_{\text{stall}_X} \leq 0$ ($X = W$ or T)

Penalty functions P_2 and P_3 are defined such that:

$$P_2 = \max(0, (\tilde{\alpha} + i_W + \tilde{\alpha}_{\text{safety}} - \alpha_{\text{stall}_W}))^2 \quad (4.6)$$

$$P_3 = \max(0, (\tilde{\alpha} + i_T + \tilde{\alpha}_{\text{safety}} - \alpha_{\text{stall}_T}))^2 \quad (4.7)$$

3. Trimmed Flight Constraint: $\|M_{\text{CG}}\| \leq \epsilon_2$

A penalty function P_4 is defined such that:

$$P_4 = (M_{\text{CG}})^2 \quad (4.8)$$

4. Longitudinal Stability Constraint: $\frac{\partial M_{\text{CG}}}{\partial \tilde{\alpha}} \leq 0$

A penalty function P_5 is defined such that:

$$P_5 = \max(0, (M_{\text{CG}}^{\tilde{\alpha} + \Delta\tilde{\alpha}} - M_{\text{CG}}^{\tilde{\alpha}}))^2 \quad (4.9)$$

where $M_{\text{CG}}^{\tilde{\alpha} + \Delta\tilde{\alpha}}$ is the moment about the CG at an angle of attack that is higher than the design angle by an (arbitrary) amount $\Delta\tilde{\alpha}$.

4.4.3.3 Statement of Optimization Problem in GA Form

The penalty functions described in the previous section are used to convert the unconstrained minimization problem of Section 4.4.1 into a constrained maximization problem which is in the standard genetic algorithm form:

GA objective function:

$$f(\underline{x}) = -(D_{\max} + r_1 P_1 + r_2 P_2 + r_3 P_3 + r_4 P_4 + r_5 P_5), \text{ to be maximized.}$$

Subject to:

$$\underline{x}_{\min} \leq \underline{x} \leq \underline{x}_{\max}$$

The function $f(\underline{x})$ is calculated for a given set of design variables $\underline{x} = x_1, x_2, \dots, x_N$ using the aerodynamic analysis procedure described in Chapter 5. The factors r_1 through r_5 are penalty function multipliers chosen by the user. The values of the penalty function multipliers used in the optimization for this report are $r_1=15,000$, $r_2=10$, $r_3=10$, $r_4=100,000$, and $r_5=1,000,000$. The reason for such large values of r_4 and r_5 is that the pitching moment about the CG usually has values smaller than $0.01 N - m$. The corresponding penalty functions must be scaled such that they become significant in comparison to the maximum dimension or the other penalty functions.

The minimum and maximum values that were used for the MAV optimization are given in Table 4.2.

Variable	Minimum	Maximum	Units
P_W	rect, zim, ziminv, ell		
AR_W	0.5	2.0	
S_W	25 (3.88)	400 (62.00)	$cm^2 (in^2)$
i_W	0	15	degrees
P_T	rect, zim, ziminv, ell		
AR_T	0.5	2.0	
S_T	0	200 (31.00)	$cm^2 (in^2)$
i_t	-15	0	degrees
x_T	0	15 (5.91)	$cm (in)$
x_{prop}	0	15 (5.91)	$cm (in)$
$\tilde{\alpha}$	-5	25	degrees

Table 4.2: Minimum and Maximum Values for Design Variables

4.5 Results and Discussion

4.5.1 Test of Genetic Algorithm Code

A FORTRAN code of the genetic algorithm was written which implements the steps of the GA code as described in Section 4.4.3. This code was tested by solving an optimization problem that has a known solution. An objective function F_{test} was defined as:

$$F_{\text{test}} = -[(w_1[P_W - P_{W_0}])^2 + (w_2[AR_W - AR_{W_0}])^2 + (w_3[S_W - S_{W_0}])^2 + (w_4[i_W - i_{W_0}])^2 + (w_5[P_T - P_{T_0}])^2 + (w_6[AR_T - AR_{T_0}])^2 + (w_7[S_T - S_{T_0}])^2 + (w_8[i_T - i_{T_0}])^2 + (w_9[x_T - x_{T_0}])^2 + (w_{10}[x_{\text{prop}} - x_{\text{prop}0}])^2 + (w_{11}[\tilde{\alpha} - \tilde{\alpha}_0])^2] \quad (4.10)$$

where the variables with the subscript 0 are constants and the factors w_1 through w_{11} are constant multipliers which scale each term so that it contributes approximately equally to the objective function. The maximum value of F_{test} is achieved when each variable is equal to its corresponding 0-subscript constant (that is, $P_W = P_{W_0}$, $AR_W = AR_{W_0}$, $S_W = S_{W_0}$, $i_W = i_{W_0}$, etc.). The values of the constants and multipliers used in the test case are shown on Table 4.3.

Variable	Target (X_0)	GA Result	Scaling multiplier (w_X)
P_W	1.000	1.000	1.000
AR_W	1.350	1.356	2.000
S_W	155.0	155.1	0.005
i_W	7.500	6.884	0.200
P_T	3.000	3.000	1.000
AR_T	0.850	0.825	2.000
S_T	95.00	102.4	0.005
i_T	-4.500	-4.790	0.200
x_T	7.500	6.940	0.100
x_{prop}	9.500	8.673	0.150
$\tilde{\alpha}$	3.500	3.413	0.100

Table 4.3: Results of GA Test Case

The genetic algorithm parameters used were a population of 50 members, 200 generations, 12-bit discretization of the design variables (except for the two discrete planform variables P_W and P_T which use 2-bit discretization), and a mutation probability of 0.05. The lower and upper bounds of the design variables were the same as those in Table 4.2. Figure 4.1 shows the convergence history of the test case. The negative of the objective function converges to a value close to the exact optimum as the number of generations increases. The final values of the design variables for the case plotted in Figure 4.1 are shown on Table 4.3. Based on the results of the test case for the GA code, it can be concluded that the genetic algorithm is working correctly. It is now possible to apply the algorithm to the actual design optimization problem.

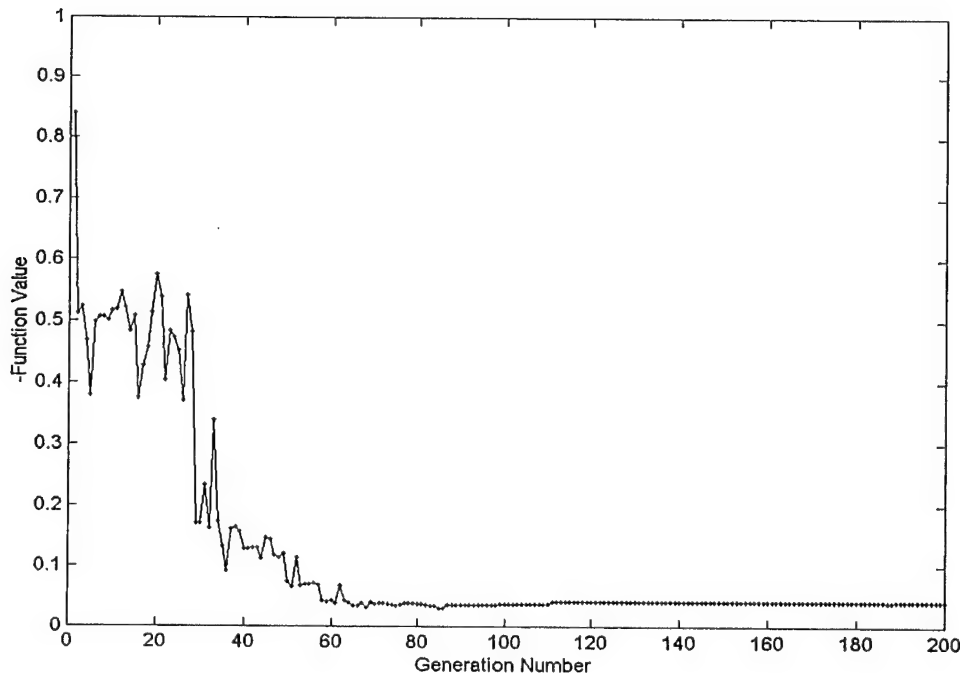


Figure 4.1: Convergence History of GA Test Case

4.5.2 Preliminary Results: Problems With Discrete Variables

The first attempts at running the actual optimization revealed some shortcomings of the procedure as outlined thus far. Convergence almost never occurred regardless of the values chosen for population size, number of generations, mutation probability, or bit-discretization. In almost all cases, the function value fluctuated wildly and did not seem to converge. The cause for this behavior was traced back to the two discrete variables of wing and tail planform (P_W and P_T). As mentioned before, these variables are only allowed to take four possible values which represent each of the four planforms tested in wind tunnel experiments. The problem arises from the fact that the aerodynamic characteristics of two planforms differ greatly even if all other factors (aspect ratio, angle of incidence) remain constant. The GA would drive all continuous design variables to an optimum for a given combination of wing and tail planform. However, if the planform variable was changed, the resulting aircraft would differ so much from the previous "near-optimum" design that convergence would be nearly impossible.

The solution to this problem was to remove the two discrete variables (wing planform and tail planform) from the list of design variables which are controlled by the GA code. That is, for each optimization run, the planform of the wing and tail are defined and kept constant. This leaves 9 continuous design variables which define completely the MAV design. One possibility for dealing with the remaining two discrete planform variables is to run 16 cases, each case corresponding to a combination of wing planform and tail planform. The smallest maximum dimension of the 16 optimized designs would be considered to be the global optimum. For the purpose of this report, solving only one of the 16 cases proves the applicability of the GA optimization code to the design of MAVs. Performing the remaining 15 cases would then be a straightforward procedure.

It was decided to define the wing to be of inverse Zimmerman planform and the tail to be of rectangular planform. These wing shapes are kept constant and the remaining 9 design variables are used in the GA code to arrive at an optimum for this configuration.

4.5.3 Results of Modified Optimization Problem

4.5.3.1 Design Variables of Optimum Design (Converged Solution)

With the modified genetic algorithm procedure it was found that convergence was easier to achieve. Approximately eight out of every ten times that the code was run resulted in convergence to a feasible solution. There are a number of factors that could cause lack of convergence in the unsuccessful cases. First and foremost, the objective function itself is highly nonlinear. Small changes in one variable have major impacts on the performance of the design. It becomes difficult for the GA to minimize the maximum dimension of the aircraft while also keeping the penalty functions as small as possible. In many of the failure cases, the optimizer converged to a solution which was not feasible (penalty functions active) but did not shift from this solution. A higher value of the mutation probability was found to fix this problem but it made the optimizer simply jump randomly from one design condition to another one. Other factors that were seen to influence convergence were the penalty function multipliers and the number of members in a given population. Some more experimentation with these parameters might prove helpful in improving the chances of a feasible convergence of the code.

Overall, converged solutions were significantly more common. Figure 4.2 shows one such successful case. It plots the aircraft's maximum dimension versus generation number. The GA optimization parameters used for this run were a population of 40 members, 60 generations, 12-bit discretization for the continuous variables, and a mutation probability of 0.06. Table 4.4 lists the values of the optimized design variables (corresponding to the fittest member of generation number 60). Figure 4.3 shows a planform view of the optimized design.

The optimized design of Figure 4.3 is similar to MAV prototypes built at Notre Dame. These aircraft have successfully flown with 100 grams takeoff weight. Specially important is the fact that the optimized MAV has a horizontal tail. There were other optimization cases that converged on a design that did not have a horizontal tail. That is, in these cases, the optimizer identified a tail-less airplane as a more efficient configuration in terms of maximum dimension. This is logical since the tail is not actually necessary to satisfy the very limited trimmed flight constraint. It may seem that the tail only adds to the maximum dimension without providing any additional benefit. However, the aerodynamic analysis used as part of the GA code does not include a very important effect associated with tail-less airplanes with low aspect ratio (LAR) wings: LAR wings usually operate at relatively large angles of attack (10° in some cases). At these high angles, the flow separates near the trailing edge of the wing without inducing stall. Control surfaces (which are usually located at the trailing edge of the wing in tail-less airplane configurations) can become ineffective when immersed in this separated air region. Ineffective control surfaces yield highly unstable flight even at cruise conditions. Extensive flight-testing of MAV prototypes has revealed that a tail-less configuration can sustain stable flight for a takeoff weight which is approximately 25% smaller than a tailed configuration of the same maximum dimension. Unfortunately, at the moment it is difficult to quantitatively define the disadvantages of tail-less flight within the aerodynamic analysis portion of the code. The understanding of

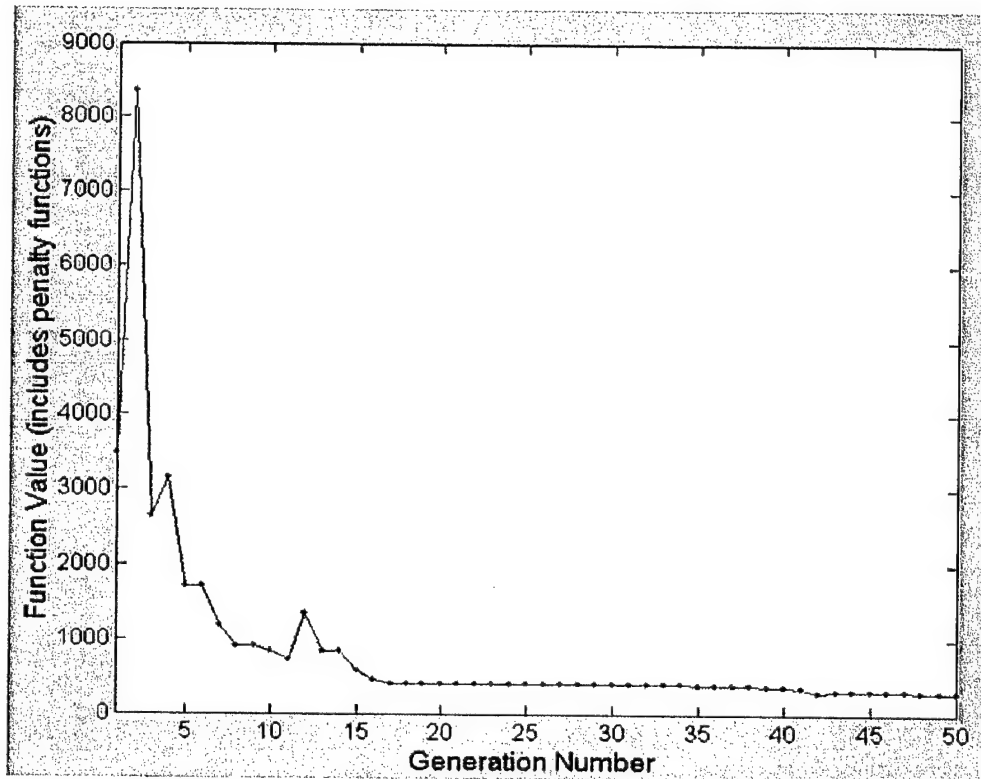


Figure 4.2: Convergence History of Genetic Algorithm

exactly how the wing's wake affects the control of the MAV is not very vast yet. Therefore, for the present version of the optimization algorithm, the problems associated with tail-less airplane configurations are ignored and a tail-less configuration is not considered in any way inferior to one that does have a tail.

The design defined in Table 4.4 is considered to be a feasible design even though the moment about the center of gravity is not exactly zero. A moment of $0.0003 \text{ N} - \text{m}$ is equivalent to a 3 gram weight located 1 *cm* from the center of gravity. This small moment is not expected to change the trim characteristics of the MAV considerably. As a reference, it should be compared to the change in pitching moment arising from the loss of fuel weight in the fuel tank as a flight progresses. A typical location for the fuel tank is 2 *cm* forward of the *CG* (of course, the exact location of the tank is different for each design). The fuel tank carries 7 grams of fuel. Thus, at the end of the flight, a change in pitching moment which is more than 3 times larger than $0.0003 \text{ N} - \text{m}$ is present due simply to fuel usage. It is therefore considered justifiable to treat $0.0003 \text{ N} - \text{m}$ as essentially zero moment.

Variable	Optimum Value	Units
P_W	3.000 (<i>zimin</i>)	
AR_W	1.725	
S_W	248.9 (38.58)	cm^2 (in^2)
i_W	12.15	degrees
P_T	1.000 (<i>rect</i>)	
AR_T	1.412	
S_T	103.0 (15.97)	cm^2 (in^2)
i_T	-9.68	degrees
x_T	6.270 (2.47)	cm (in)
x_{prop}	3.950 (1.56)	cm (in)
$\tilde{\alpha}$	2.53	degrees
Span of wing	20.72 (8.16)	cm (in)
Span of tail	12.06 (4.75)	cm (in)
Maximum dimension	21.20 (8.35)	cm (in)
Cruise speed	11.78 (26.36)	m/s (MPH)
Lift	1.024	N
M_{CG}	0.0003	$N - m$
$M_{CG}^{\tilde{\alpha} + \Delta\tilde{\alpha}}$	-0.0018	$N - m$

Table 4.4: Optimized MAV Design

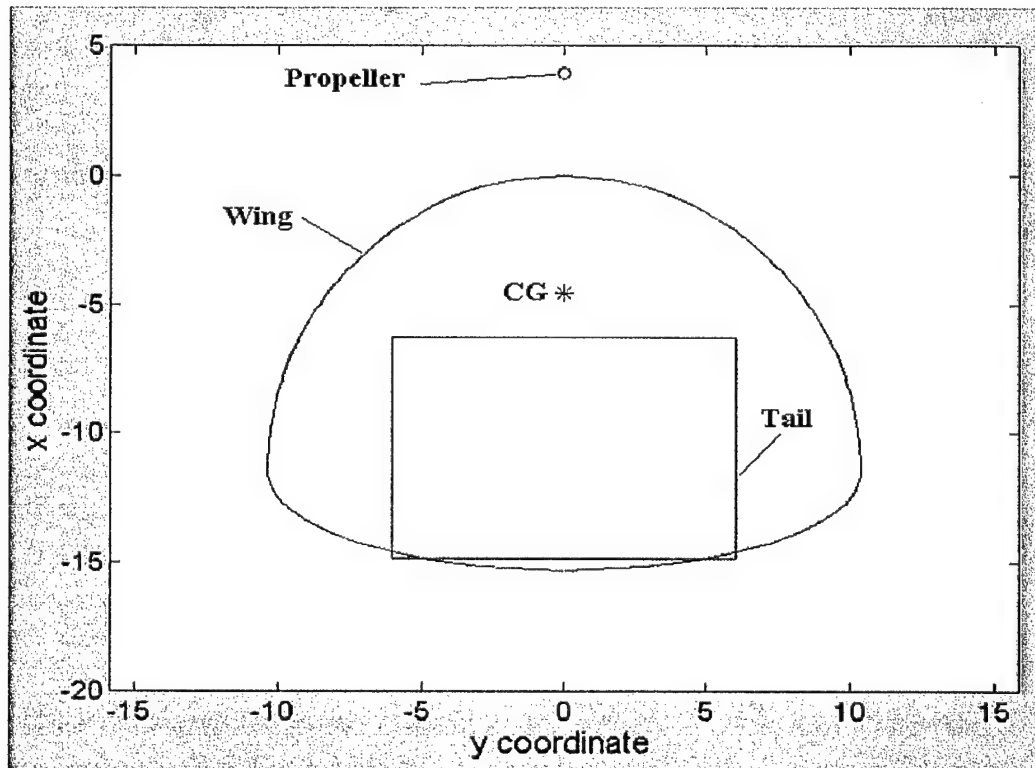


Figure 4.3: Top View of Optimized MAV Design

4.6 Conclusions and Recommendations of MAV Optimization

In this chapter, a genetic algorithm optimization method was applied to the design-optimization of a micro air vehicle. Typical mission requirements were used to define specific constraints and restrictions. The genetic algorithm code was found to converge on feasible designs that met all constraints and satisfied all mission requirements and restrictions.

In some cases, convergence of the algorithm did not occur. This is attributed largely to the highly nonlinear character of the objective function coupled with the restrictive nature of the constraints. It was also found that the aerodynamic performance analysis used within the GA code is not capable of modeling the unstable flight characteristics that can occur with some tail-less configurations. This is an important aspect of the design because tail-less airplanes can feasibly represent optimum configurations in respect to maximum dimension. Yet flying characteristics of certain configurations of tail-less aircraft are not good. Although a detailed study of aerodynamic interactions associated with tail-less and tailed aircraft configurations is beyond the scope of this work, it is still suggested that some type of qualitative analysis be incorporated in an effort to model the complications of tail-less configurations more accurately. Flow visualization experiments with different configurations are planned for the near future and will provide qualitative insight into the flow structure of separated flow regions in LAR wings.

Chapter 5

Design-Optimization Part II: Aerodynamic Analysis

This chapter discusses in detail the procedure used to calculate a value for the objective function used within the optimization scheme based on a set of design variables \underline{x} . The analysis consists of the following steps:

1. Determine the values of C_L and C_D of the wing and tail given each surface's angle of incidence, aspect ratio, and wing planform.
2. Check for stall condition for the wing and tail.
3. Iteratively determine the cruise velocity of the aircraft and the lift and drag forces of the wing and tail.
4. Calculate the location of the center of gravity.
5. Calculate the pitching moment about the CG.
6. Check for longitudinal stability (negative slope of M_{CG} vs. α curve).
7. Determine the maximum dimension of the MAV design.
8. Calculate the values of the penalty functions based on violations of constraints and penalty function multipliers.
9. Combine the maximum dimension and penalty functions to calculate the value of the objective function $f(\underline{x})$ for the given design defined by \underline{x} .

5.1 Interpolation of Aerodynamic Coefficients and Stall Angle Analysis

The first step of the procedure (shown schematically in Figure 5.1) is to calculate the lift and drag coefficients of the wing and tail based on the values of 7 design variables: the planform, aspect ratio, and incidence angle of the wing and tail and the angle of attack of the aircraft. The stall angle is also determined as a function of these variables and a check is made for both the wing and the tail to check for a stall condition. Note that the stall check for the tail does not

include the effect of downwash. The change in effective angle of inclination of the local flow of the horizontal tail due to downwash is expected to be small. Future revisions of the analysis procedure will include the downwash effects.

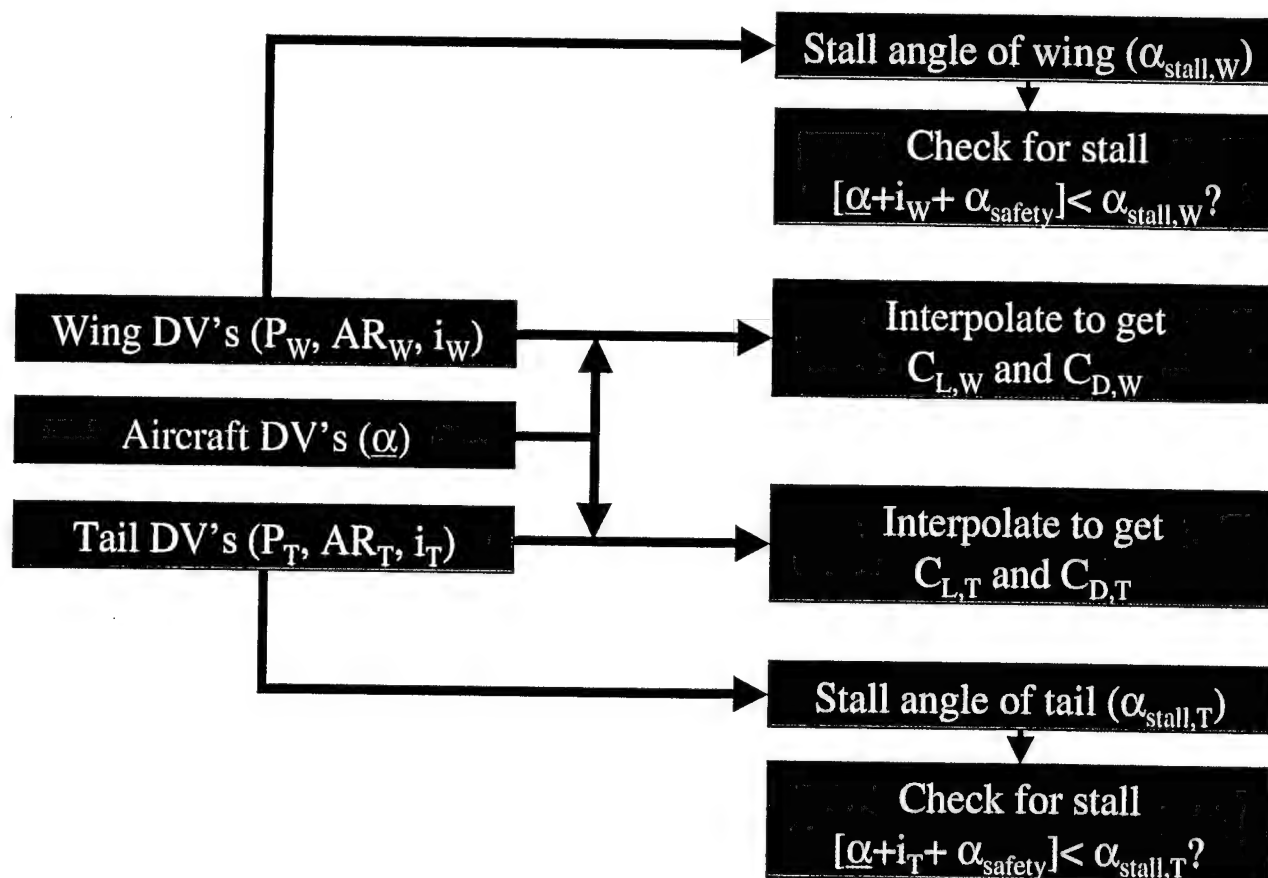


Figure 5.1: Analysis Procedure:

5.1.1 Determination of Lift and Drag Coefficients for Wing and Tail

Research on low aspect ratio wing aerodynamics at low Reynolds numbers has revealed that analytical expressions for lift and drag coefficients are seldom accurate. Even though the slope of the linear region of the lift curve can be approximated quite well, most LAR wings operate in the nonlinear region of lift. Analytical methods for nonlinear lift have been found not to compare well with wind tunnel experiment data. Correlations of experiment drag curves with analytical predictions have been determined to be particularly inaccurate.

A proposed solution to this problem is to use the wind tunnel data presented in this report as the basis of an interpolation scheme. The wind tunnel data corresponds to flat-plate wings of aspect ratios of 0.5, 0.75, 1.0, 1.25, 1.5, 1.75, and 2.0 and four distinct wing planforms (rectangular, Zimmerman, inverse Zimmerman, and elliptical). This experimental data consists of curves of lift and drag coefficients versus angle of attack ($-10^\circ \leq \alpha \leq 40^\circ$ in increments of 1°).

The chord-Reynolds numbers at which these sets of data were taken are 70,000 and 100,000, with some wings having been tested at 140,000. Most MAV designs with a takeoff weight of approximately 1 Newton operate at Reynolds numbers between 100,000 and 200,000. Experimental data has revealed little change of the aerodynamic characteristics from $Re = 100,000$ to $Re = 140,000$. Thus the lift and drag coefficients at $Re = 100,000$ are considered as the correct values. All wing models tested had a thickness to chord ratio of 1.96%, camber of 0%, and 5-to-1 elliptical leading and trailing edges.

The lift and drag coefficients of a particular wing or tail design are considered to be a function of three variables only: wing planform, aspect ratio, and angle of inclination with respect to the incoming flow (α_{eff}). Since the planforms are discrete variables, C_L and C_D are, for a given planform, actually functions of only two independent variables. Note however that the angle of inclination of the wing or tail with respect to the incoming flow is itself a function of two design variables: $\tilde{\alpha}$ and i_W (or $\tilde{\alpha}$ and i_T for the tail). That is, $\alpha_{effW} = i_W + \tilde{\alpha}$ and $\alpha_{effT} = i_T + \tilde{\alpha}$. A linear interpolation procedure is used to obtain the value of lift and drag coefficients for a given set of design variables. The interpolation algorithm is the following:

1. The planform of the wing or tail is read and the database of wind tunnel data corresponding to that planform is loaded.
2. The lift and drag coefficients are interpolated linearly at the desired α_{eff} for **all** aspect ratios.
3. The interpolated coefficients from step 2 are then used to interpolate the final value of C_L and C_D at the desired aspect ratio. Figures 5.2 and 5.2 show examples of the interpolation procedure.

Once the C_L and C_D are known, they are converted to dimensional forces:

$$L_W = C_{LW} \frac{1}{2} \rho V_\infty^2 S_W \quad (5.1)$$

$$D_W = C_{DW} \frac{1}{2} \rho V_\infty^2 S_W \quad (5.2)$$

$$L_T = C_{LT} \eta \frac{1}{2} \rho V_\infty^2 S_T \quad (5.3)$$

$$D_T = C_{DT} \eta \frac{1}{2} \rho V_\infty^2 S_T, \quad (5.4)$$

where η accounts for the change in dynamic pressure at the tail with respect to the dynamic pressure at the wing. In the first implementation of this design-optimization procedure, η is set to 1.0.

V_∞ is not known a priori and must be calculated in an iterative manner. See Section 5.2.2 for details on how this iterative procedure is carried out.

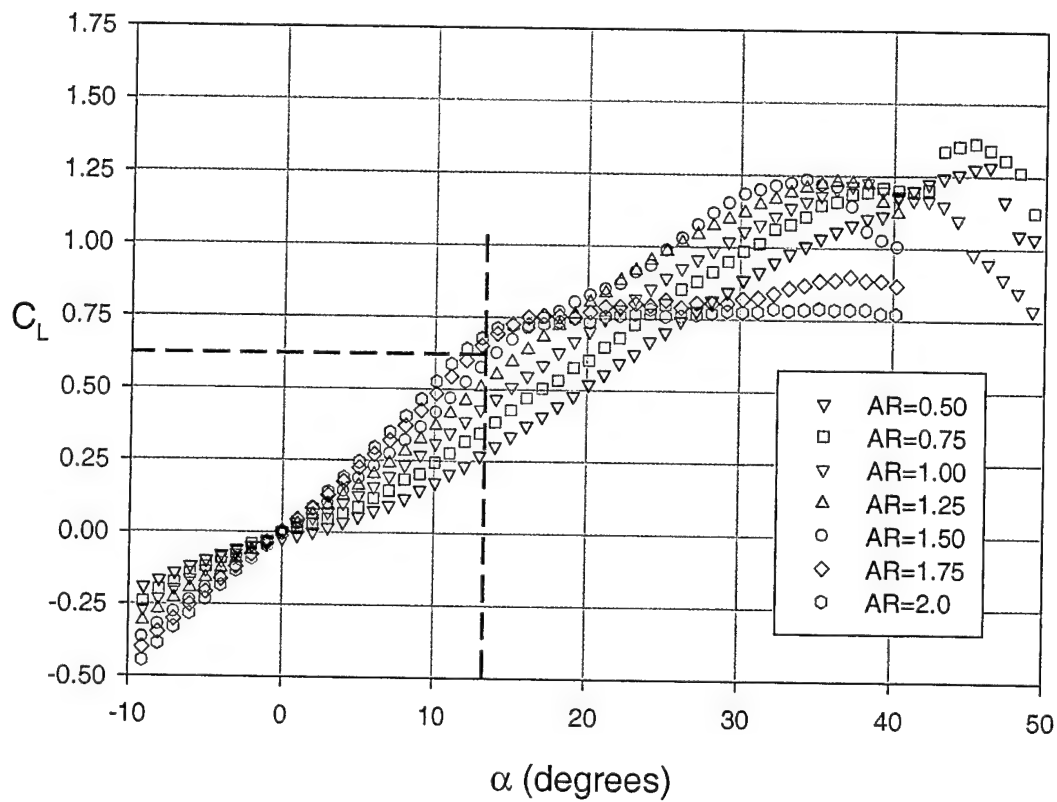


Figure 5.2: Example of Interpolation of C_L : Interpolate α

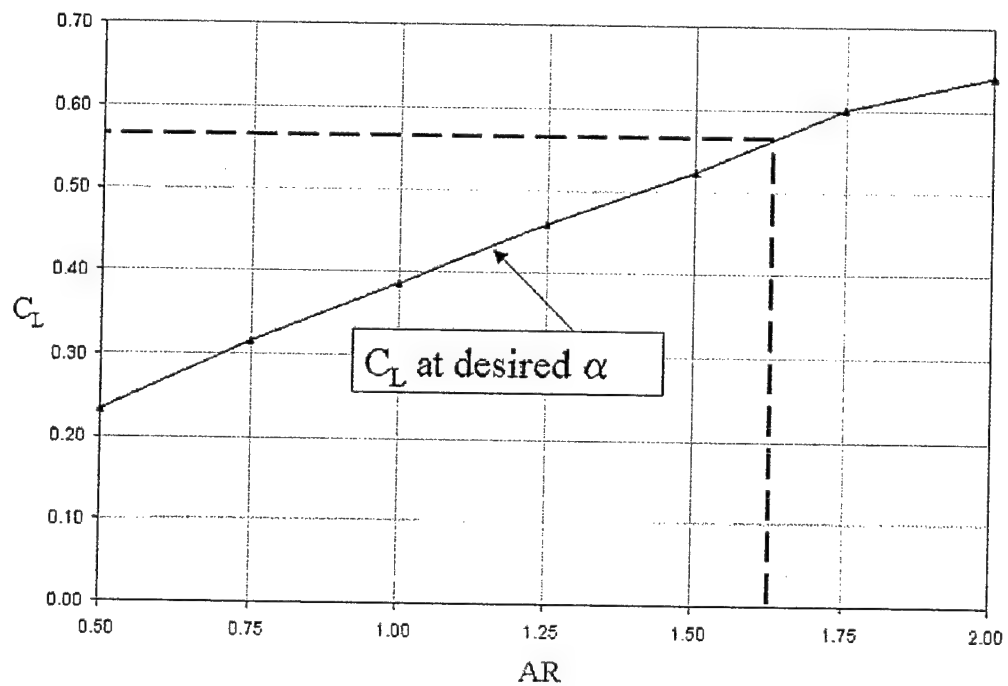


Figure 5.3: Example of Interpolation of C_L : Interpolate AR

5.1.2 Determination of Stall Angle for Wing and Tail

The angle of attack at stall is also needed within the optimization program. In Section 3.2, graphs of α_{stall} vs. AR for each of the four planforms were presented and discussed. An interpolation procedure similar to the one used in the previous section could be implemented for the value of α_{stall} . In that manner, a value of α_{stall} could be calculated given the wing planform and aspect ratio. At the time of writing this report, the aerodynamic analysis code had not been updated to include such an interpolation procedure. Instead, the average value (at each value of AR) for all four wing planforms was plotted versus AR as shown in Figure 5.4. An empirically derived expression that closely approximates the average stall angle curve is also plotted. The equation for this empirical approximation is

$$\alpha_{\text{stall}} \approx -10^\circ \text{atan}(4(AR - 1.25)) + 28^\circ \quad (5.5)$$

In lieu of the interpolation technique, Equation 5.5 is used within the analysis program to determine the maximum allowable angle of attack of the wing and tail. Future versions of the code will have a more detailed determination of α_{stall} through an interpolation method that is unique to each planform.

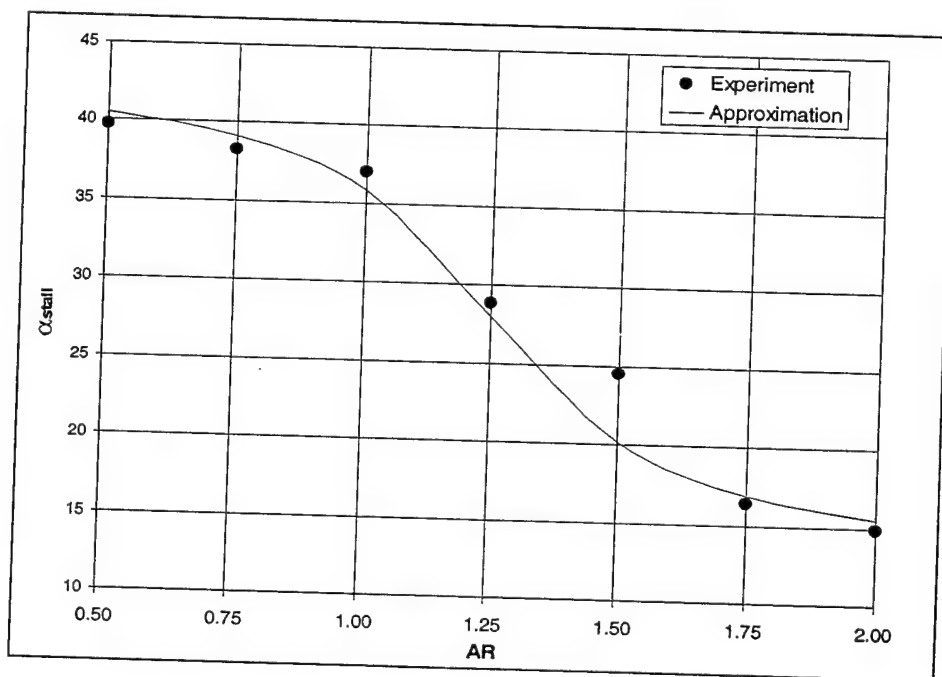


Figure 5.4: Average Stall Angle of Attack for All Planforms

5.2 Drag Analysis and Cruise Speed

The total drag force is determined here through an iteration procedure. The cruise velocity is needed to calculate the total drag force, and in turn, the thrust available from the propulsion source (engine) is dependent on cruise speed. Thus, in an iterative manner, the cruise speed at which the drag and thrust are equal to each other is calculated. The procedure used in this analysis is diagrammed in Figure 5.5.

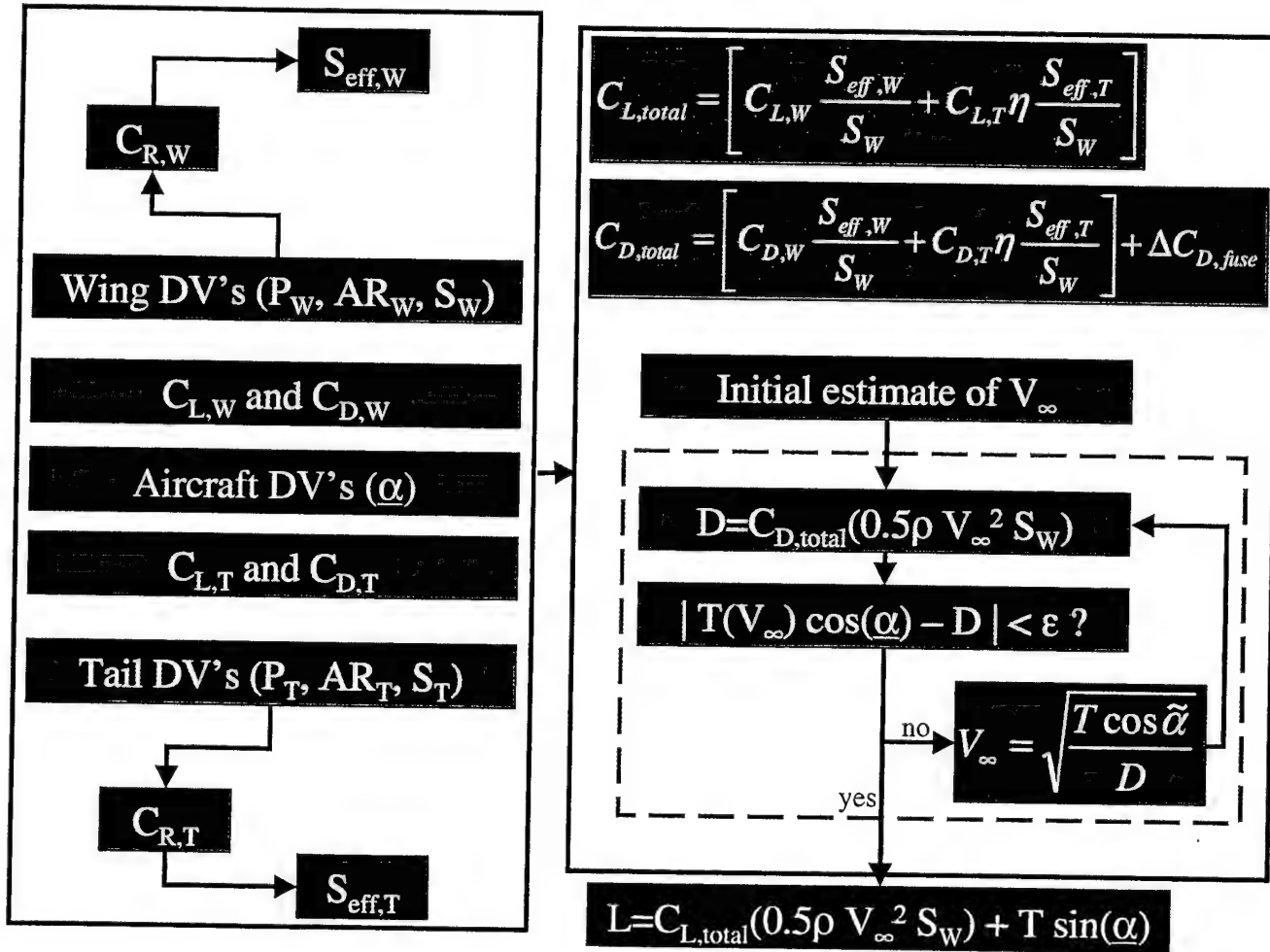


Figure 5.5: Analysis Procedure: Cruise Speed and Lift and Drag Forces

5.2.1 Total Drag Force

Thus far, the drag coefficients of the wing and tail are known based on the interpolation procedure of Section 5.1.1. An additional drag increment exists due to the presence of the fuselage, engine, and vertical tail, as well as due to aerodynamic interactions between these items and the wing/tail. Because the fuselage is expected to have the greatest influence on the total airplane drag increment, wind tunnel experiments were conducted that measured the difference in drag coefficient between a wing alone and a wing outfitted with a typical MAV

fuselage. In such a manner, an empirical method for estimating the increase in drag due to the fuselage can be formulated. The experiments were done using rectangular, Zimmerman, and inverse Zimmerman wings of AR 1.0, 1.5, and 2.0. Figures 5.6 through 5.8 show results for the rectangular planforms of aspect ratio 1.0, 1.5, and 2.0. In each plot, two curves are graphed. One of them is the difference in drag coefficient between the wing outfitted with a fuselage and the wing alone. That is, this is the increment in drag coefficient due to the presence of the fuselage. The other curve plots the drag coefficient of the fuselage by itself (without a wing). The drag coefficient for the fuselage is nondimensionalized by the same reference area as that of the wing corresponding to each graph. It can be seen from these graphs that the actual increment in drag coefficient due to the fuselage is generally greater than the drag of the fuselage alone. This is likely due to interference effects that cannot be modeled in a test of the fuselage alone.

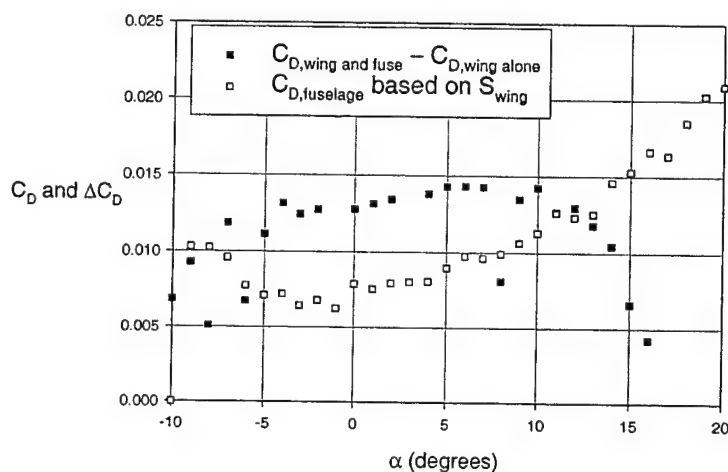


Figure 5.6: Increment of Drag due to Fuselage, Rectangular Wing of $AR = 1.0$

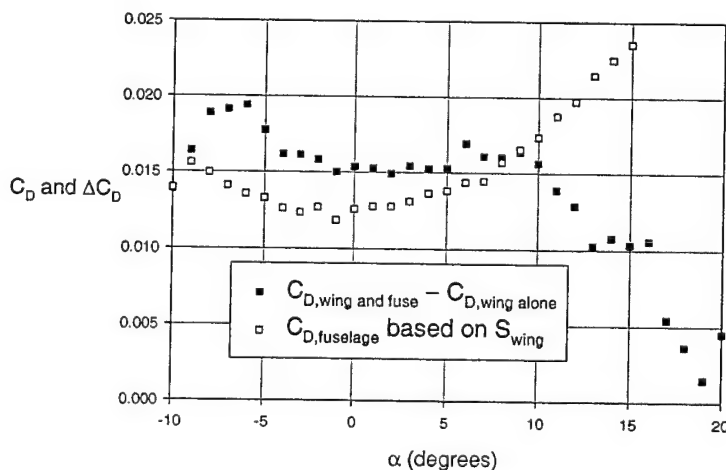


Figure 5.7: Increment of Drag due to Fuselage, Rectangular Wing of $AR = 1.5$

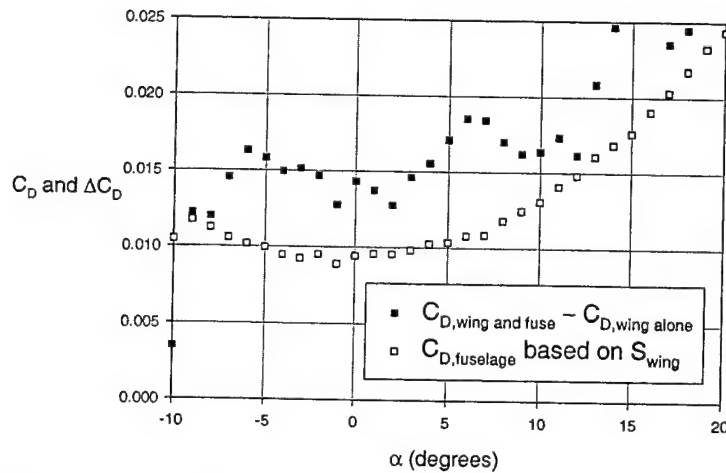


Figure 5.8: Increment of Drag due to Fuselage, Rectangular Wing of $AR = 2.0$

It is interesting to note, though, that the drag increment is actually lower than the C_D of the fuselage alone for the wings of $AR = 1.0$ and $AR = 1.5$ at angles of attack beyond 15° . This is again expected to be due to interference effects and highly nonlinear aerodynamic interactions occurring between the wing and the fuselage body. A detailed investigation of the linear and nonlinear effects associated with fuselage-body drag is beyond the scope of the current research. Rather, it is desired to obtain an approximation to the additional drag generated by the presence of a fuselage body on a lifting wing. Thus, for the purpose of the aerodynamic analysis presented herein, the average increase in drag coefficient due to the fuselage is taken to be 0.015 (based on the wing reference area). This additional drag coefficient is added to the aircraft total drag budget, yielding a total drag coefficient for the entire airplane.

5.2.2 Thrust Force and Cruise Speed

Once the total aircraft drag coefficient is known, the drag force can be calculated based on the freestream velocity, V_∞ . However, V_∞ is not known a priori. It is determined through an iterative procedure which matches the thrust from the engine with the drag force of the airplane at a given freestream velocity. Figure 5.9 shows the variation of engine thrust with freestream velocity (obtained experimentally) for a Cox 0.010 Tee Dee engine. This particular engine is typically used on small remote-controlled airplanes and represents the most adequate off-the-shelf propulsion system for non-battery-powered MAV designs. Again, the emphasis here is on the design-analysis procedure, not on the details of each step. The code could easily be changed such as to accommodate the use of an electric motor system whose performance is known.

The iterative procedure for defining V_∞ is the following:

1. Provide an initial guess for V_∞ .
2. Calculate the drag force of the aircraft and the engine thrust at that value of V_∞ . The thrust of the engine (in Newtons) is given by

$$T = -0.0208V_\infty \cos \alpha + 0.6991, \quad (5.6)$$

where V_∞ is in m/s .

3. If the component of thrust in the drag direction is not equal to the total drag (within some ϵ), then define a new $V_\infty = \sqrt{\frac{T \cos \tilde{\alpha}}{C_{D_{total}} 0.5 \rho S_W}}$.
4. Repeat steps 1 through 3 until $|T \cos \tilde{\alpha} - D_{total}| \leq \epsilon$.

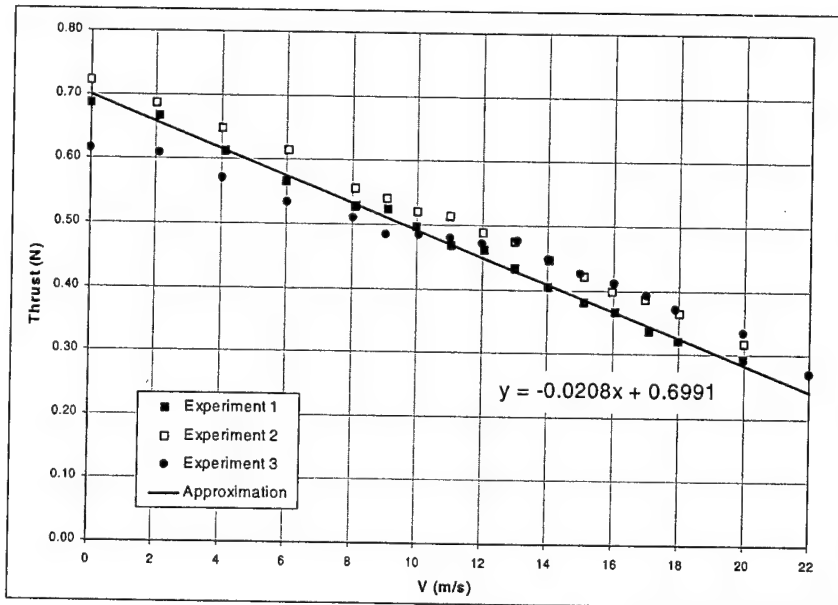


Figure 5.9: Experimental Determination of Thrust of MAV Engine as a Function of V_∞

5.3 Center of Gravity Analysis

In the next section, the pitching moment of a given MAV design with respect to the center of gravity is calculated. Before that can be done, however, the location of the center of gravity must be defined first. The center of gravity of the airplane is a function of the planform, aspect ratio, area, and location of the wing and tail and the location of the propeller. A schematic of the procedure used to calculate the center of gravity is shown in Figure 5.10.

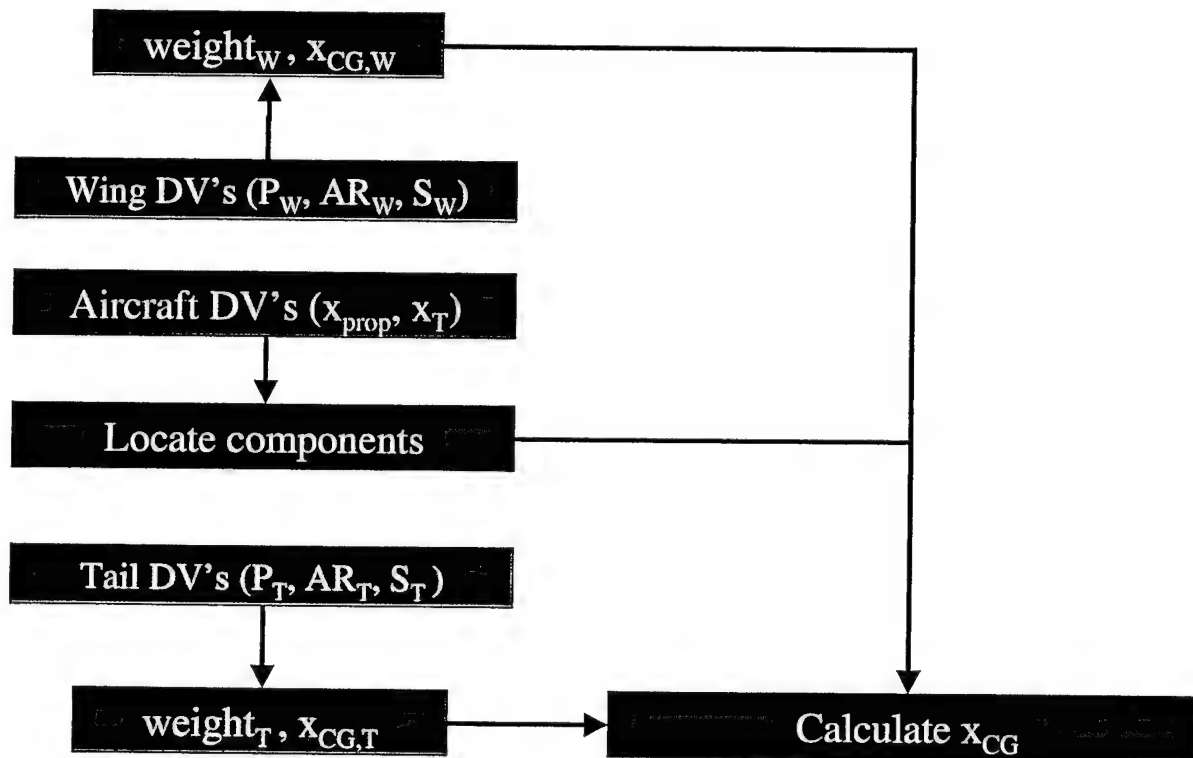


Figure 5.10: Analysis Procedure: Center of Gravity Analysis

The wing and tail geometry parameters are used to calculate the weight of each of these surfaces and the location of their centers of mass. Their position relative to the origin is used to calculate the moment exerted by their weights.

Also needed for a mass balance analysis is the location and weight of all components. All component locations are based on the value of the design variable x_{prop} . Figure 5.11 illustrates the general layout of the components in a typical MAV design.

The components and placement constraints are dictated by the desire to shift the center of gravity as forward as possible, within the constraints of the components placed within the fuselage. The reason for the desire of a forward CG is that in general the fuselage has to be lengthened beyond the leading edge of the wing in order to shift the CG forward enough for

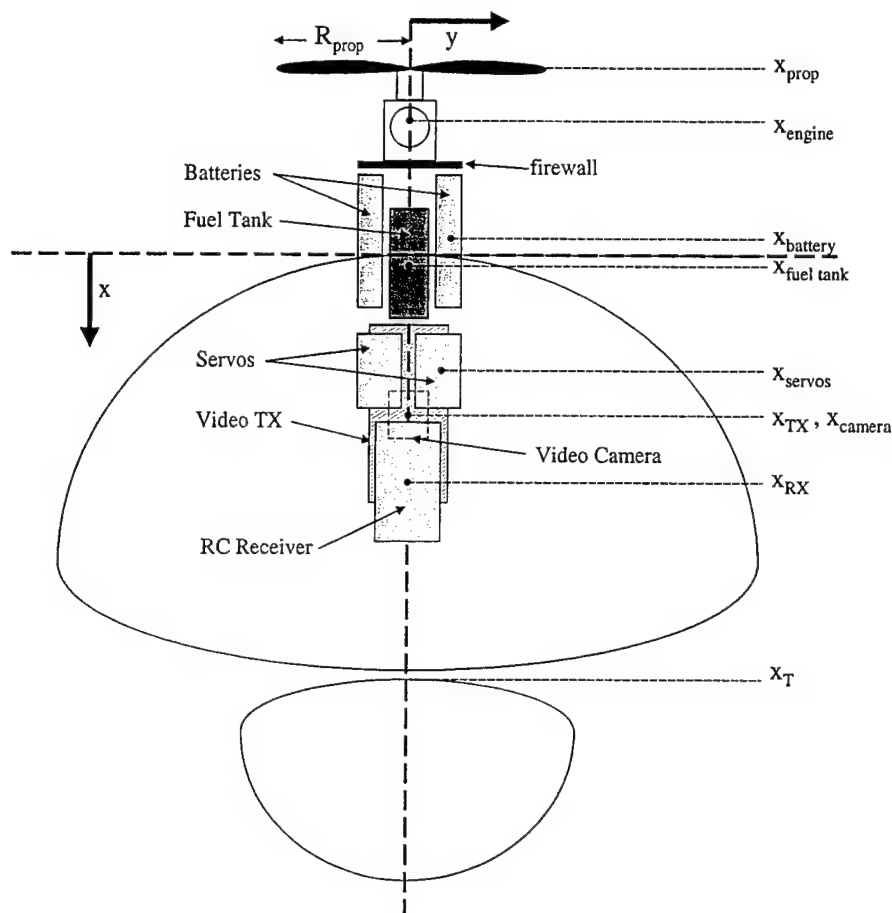


Figure 5.11: Dimensions of MAV

a longitudinally stable configuration. Extending the fuselage increases the maximum dimension and thus it should be avoided as much as possible. Therefore, by forcing the placement of the components as far forward as possible, the required extension of the fuselage past the leading edge of the wing is minimized. The placement constraints of the components are:

1. **Engine:** The engine is located just behind the propeller. A firewall (usually 0.3 *cm* thick) is placed directly behind the engine.
2. **Batteries:** The two battery cells are located just behind the firewall, leaving a small amount of space for foam cushioning between the firewall and the front of the cells (about 0.5 *cm* thick).
3. **Fuel tank:** The fuel tank is located behind the firewall, with enough spacing to allow for the fuel tubing to curve around through a hole in the firewall towards the engine (about 1 *cm*).
4. **Video Transmitter:** The video transmitter is located at the bottom of the fuselage, behind either the batteries or the fuel tank (depending on which of the two extends further downstream). Foam cushioning spacing is taken into account as well.
5. **Camera:** The camera is located directly underneath the video transmitter.

6. **Servos:** The two servos are located at the top of the fuselage, behind either the batteries or the fuel tank (depending on which of the two extends further downstream).
7. **RC receiver:** The radio control receiver is located directly behind the servos, again allowing for foam spacing.

It should be noted that the dimensions, weight, center of gravity, and locational constraints of each of these components are assumed to be known and are furthermore considered to be constant parameters of the design problem rather than design variables (see Appendix B for details about the component specifications). The only true design variable is x_{prop} . All other component location variables are derived from x_{prop} . Given this information it is possible to determine the location of the center of gravity of the MAV design.

5.4 Pitching Moment Analysis

5.4.1 Moment About the CG

Having calculated the x -location of the center of gravity of the aircraft, it is now possible to calculate the pitching moment with respect to the CG. The procedure is outlined in Figure 5.12.

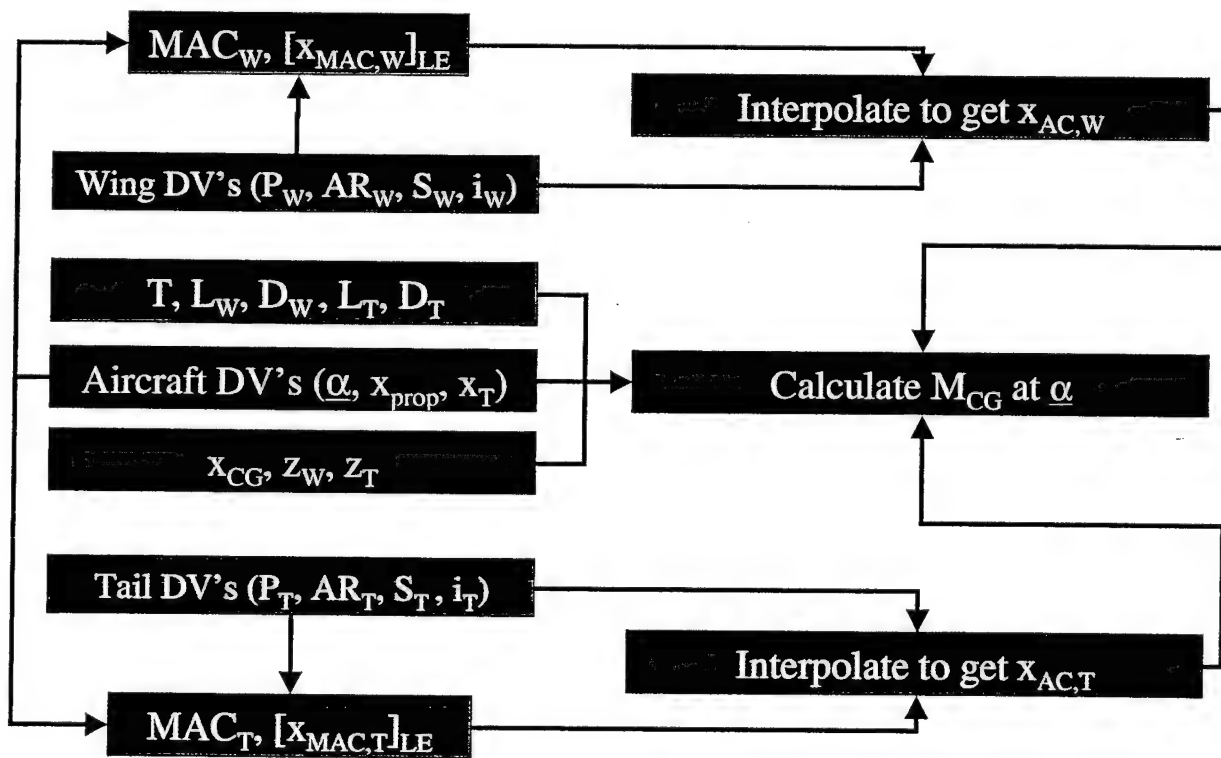


Figure 5.12: Analysis Procedure: Pitching Moment About the CG

Referring to Figure 5.13, the following expression for the pitching moment with respect to the center of gravity (positive for pitch up) can be derived:

$$\begin{aligned}
 M_{CG} = & -(L_W \cos \tilde{\alpha})(x_{AC_W} - x_{CG}) - (L_W \sin \tilde{\alpha})(z_W) \\
 & - (L_T \cos \tilde{\alpha})(x_{AC_T} - x_{CG}) + (L_T \sin \tilde{\alpha})(z_T) \\
 & - (D_W \sin \tilde{\alpha})(x_{AC_W} - x_{CG}) + (D_W \cos \tilde{\alpha})(z_W) \\
 & - (D_T \sin \tilde{\alpha})(x_{AC_T} - x_{CG}) - (D_T \cos \tilde{\alpha})(z_T) + (N_P)(x_{prop} + x_{CG}) \quad (5.7)
 \end{aligned}$$

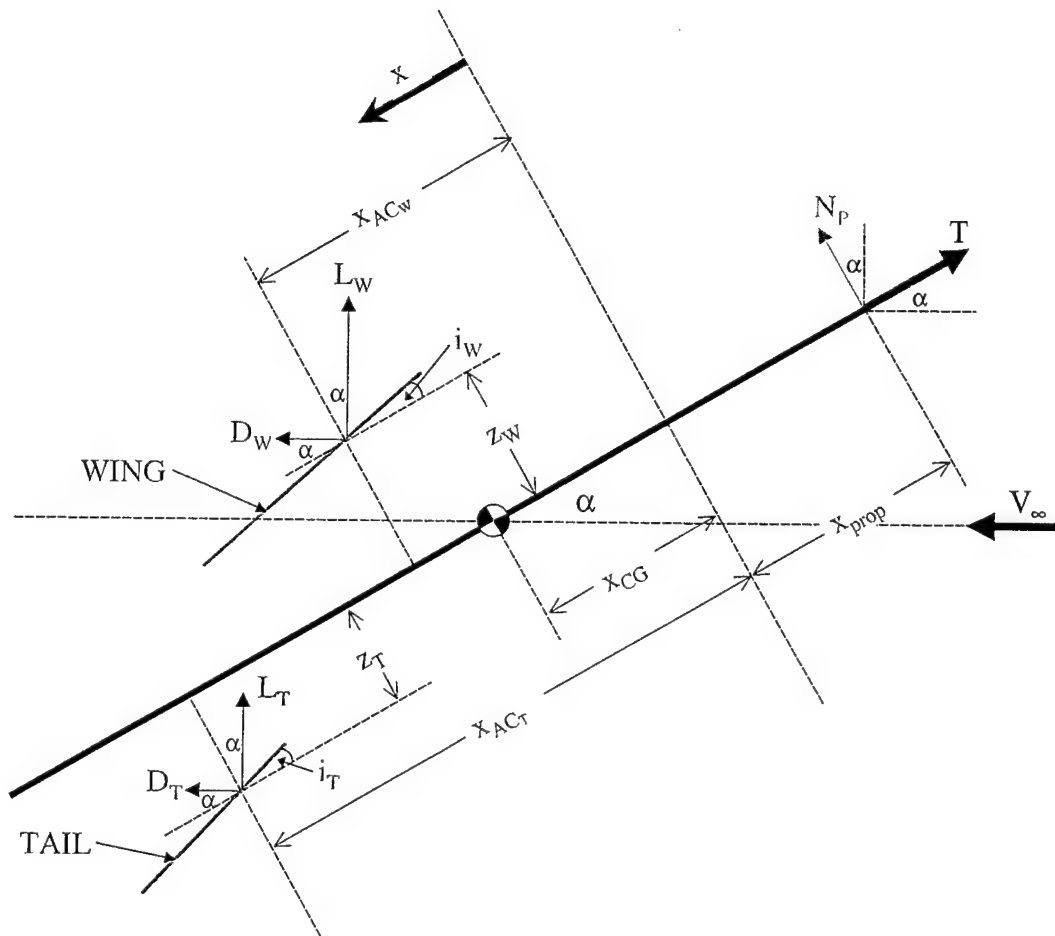


Figure 5.13: Pitching Moment About the Center of Gravity

The variables z_W and z_T represent the separation between the centerline of the fuselage and the quarter-chord location of the MAC of the wing and tail, respectively. This separation is

dictated by the height of the components that will fit into the fuselage (as described in Appendix B). Furthermore, as discussed in Section 4.2.3, the tail is assumed to be always below the wing. z_W and z_T were both set to 2.0 cm for use in the optimization code of this report.

The force N_P is the propeller normal force which is generated by a rotating propeller when it is inclined at an angle of attack with respect to the incoming flow. Following the procedure of Etkin [23], the approximate value of N_P was calculated for the 3-inch propeller used in the Cox 0.010 engine. At an angle of incidence of 30° , the normal propeller force was determined to be equivalent to a mass of 1 gram. In comparison with the 100 gram takeoff weight of the MAV, this is a small force and it contributes only very slightly to the pitching moment. Therefore it was decided to neglect the influence of the propeller normal force. This simplification greatly shortens the computation time because the pitching moment is no longer a function of freestream velocity.

5.4.2 Aerodynamic Center

The location of the aerodynamic center of the wing and tail also deserves some attention. As discussed in Section 3.3, experiments of LAR wings at low Re have revealed that the aerodynamic center of such wings is not constant with angle of attack. It generally shifts towards the trailing edge as the angle of attack is increased. At the time of writing this report, the aerodynamic analysis code had not yet been updated to include the results of aerodynamic center analysis of Section 3.3. Future revisions of the code will include such analysis and will incorporate wind tunnel data into an interpolation scheme similar to the one used in Section 5.1.1. As such, the location of the aerodynamic center would be a function of angle of attack, aspect ratio, and wing planform and would be determined empirically based on wind tunnel data. For the analysis code used for this work, a constant value was assigned to the AC of all wings and all ARs at all angles of attack. The value chosen was 30% of the MAC.

For the four wing planforms studied in this work, the length of the MAC and the x -location of its leading edge is calculated using the following formulas:

For rectangular planforms

$$b = \sqrt{AR S} \quad (5.8)$$

$$C_{root} = \frac{S}{b} \quad (5.9)$$

$$MAC = C_{root} \quad (5.10)$$

$$y_{MAC} = 0 \quad (5.11)$$

$$x_{MAC_{LE}} = 0 \quad (5.12)$$

For Zimmerman, inv. Zimmerman, and elliptical planforms

$$b = \sqrt{AR S} \quad (5.13)$$

$$C_{\text{root}} = \frac{S}{0.5\pi(b/2)} \quad (5.14)$$

$$MAC = \frac{2b(C_{\text{root}})^2}{3S} \quad (5.15)$$

$$y_{MAC} = \frac{(b/2)}{3\pi} \sqrt{9\pi^2 - 64} \quad (5.16)$$

$$x_{MACLE} = a_1 - \sqrt{(a_1)^2 \left[1 - \frac{y_{MAC}^2}{(b/2)^2} \right]} \quad (5.17)$$

The geometry parameters a_1 and a_2 of the ellipse-based wings are defined in Figure 5.14.

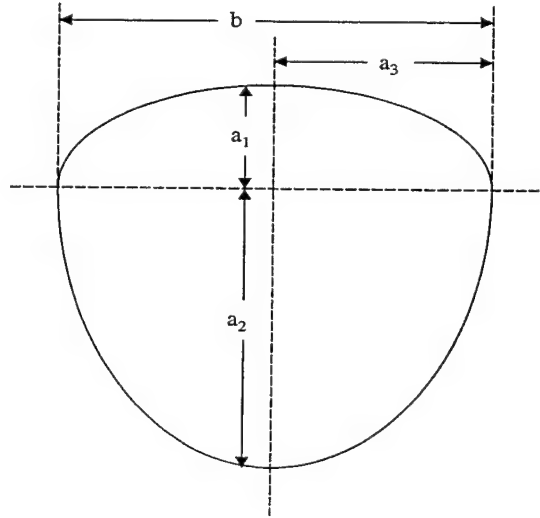


Figure 5.14: Geometry Parameters for Ellipse-Based Wings

5.4.3 Longitudinal Stability Analysis

The longitudinal stability requirement for the MAV design states that the slope of the pitching moment about the center of gravity should be negative. A test for longitudinal stability is performed within the aerodynamic analysis code by calculating the pitching moment at an angle of attack greater than the design angle of attack of the aircraft. That is, the pitching moment of the aircraft is taken at an angle $\tilde{\alpha} + \Delta\tilde{\alpha}$ where $\tilde{\alpha}$ is the design angle of attack of the aircraft and $\Delta\tilde{\alpha}$ is an arbitrarily chosen increment in angle. For the results presented in this report, $\Delta\tilde{\alpha}$ is set equal to 2° . If the moment at $\tilde{\alpha} + \Delta\tilde{\alpha}$ is lower than the moment at $\tilde{\alpha}$, then the longitudinal stability requirement is satisfied. The procedure used for this stability analysis is shown schematically in Figure 5.15.

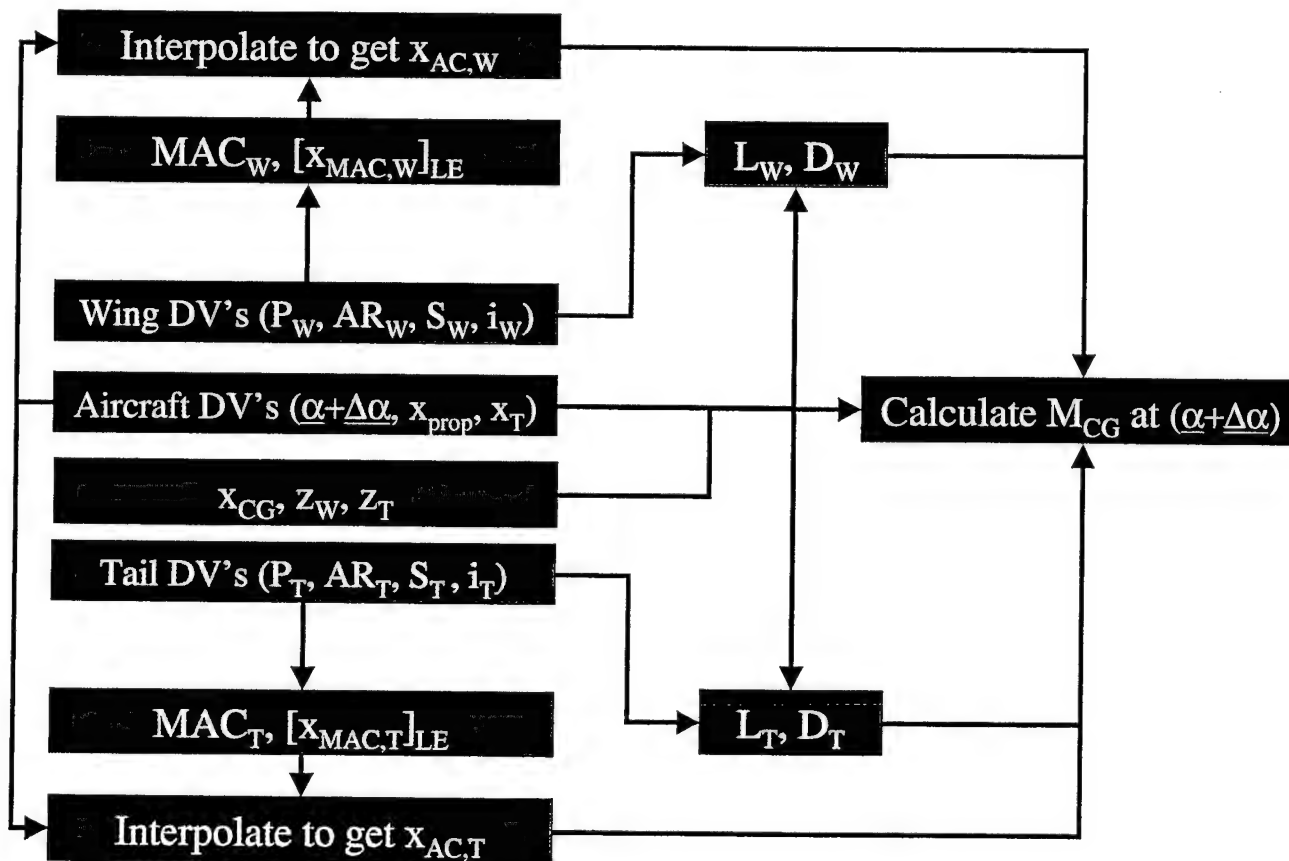


Figure 5.15: Analysis Procedure: Longitudinal Stability Requirement

5.5 Maximum Dimension and Penalty Functions

The objective function of a particular aircraft design can now be calculated. This objective function is a function of the maximum dimension of the aircraft as well as of the penalty functions arising from the constraints of the problem. A detailed discussion of the penalty functions associated with the design problem is given in Section 4.4.3.2. The steps followed for this step of the analysis code are summarized in Figure 5.16.

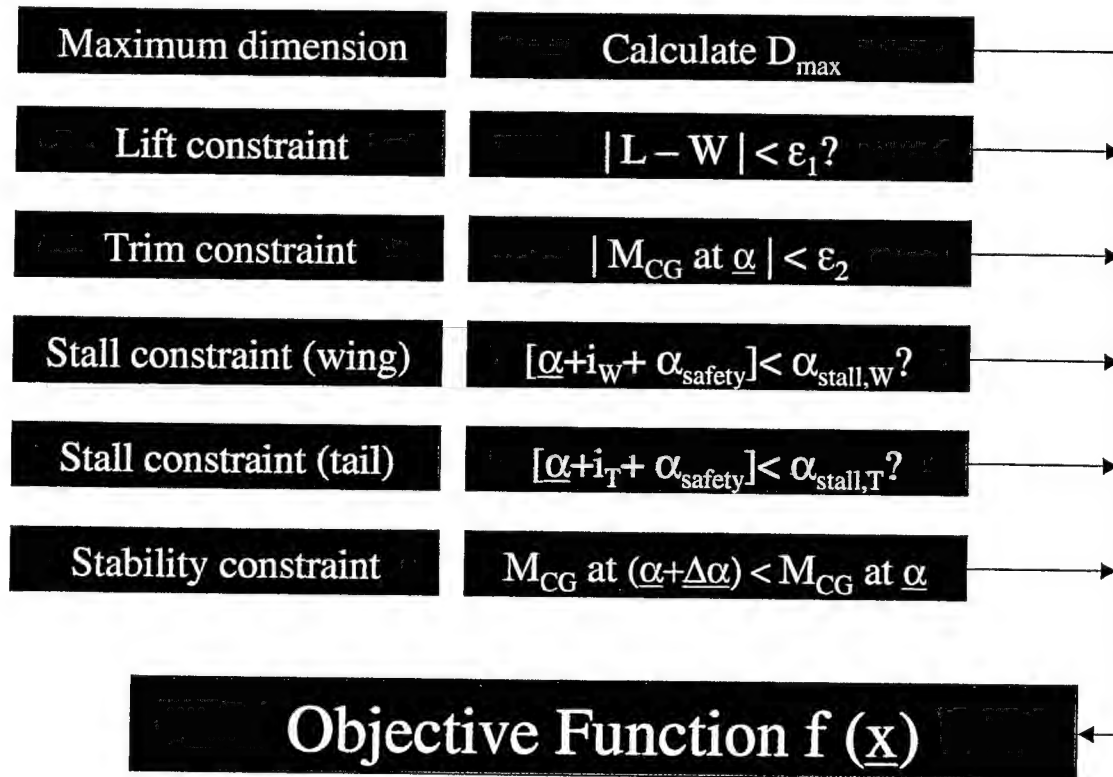


Figure 5.16: Analysis Procedure: Pitching Moment About the CG

The maximum dimension of the MAV design is calculated first. The distances in Figure 5.17 (d_{W_1} , d_{W_2} , d_{T_1} , d_{T_2} , H_{W-T_1} , H_{W-T_2} , H_W , and H_T) can be determined based on the geometry and location of the wing and tail and the x -location of the propeller. The largest of these distances is the maximum dimension of the aircraft.

The penalty functions associated with the constraints of lift, stall, trim, and longitudinal stability are then added to the objective function after being scaled by appropriate penalty function multipliers. It is this objective function value that is to be optimized by the genetic algorithm code.

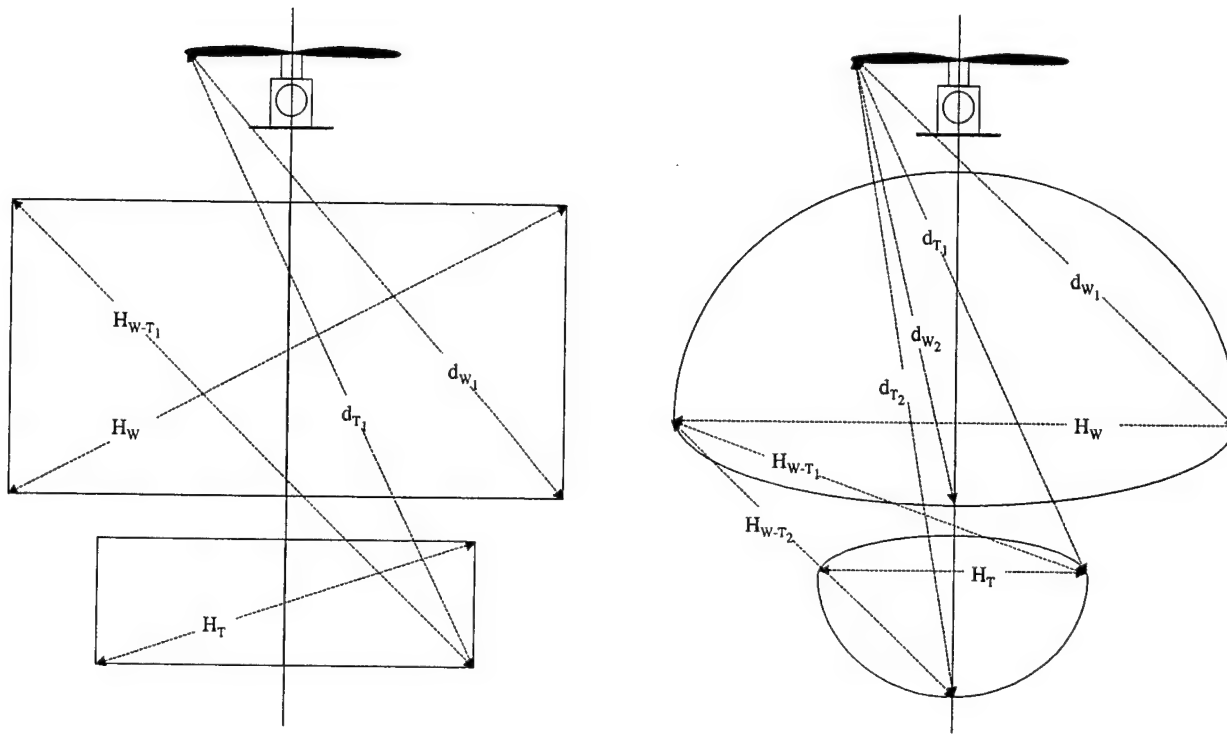


Figure 5.17: Dimensions of MAV

5.6 Conclusions for Aerodynamic Analysis Procedure

In this chapter, the procedure used to determine the objective function of a given set of MAV design variables was presented. The procedure incorporates wind tunnel data of LAR wings at low Re within an interpolation scheme in order to calculate lift and drag coefficients as a function of planform, aspect ratio, and angle of incidence. This chapter also presents the procedure used to determine the cruise speed, calculate the pitching moment about the center of gravity, and perform a check for longitudinal stability.

All of these aerodynamic performance characteristics are incorporated into penalty functions (constraints). The maximum dimension of a given MAV design (a purely geometric performance measure) is then combined with the penalty functions to arrive at a final value of the objective function of a particular design. This value of the objective function is then passed to the genetic algorithm code, which attempts to optimize the design while remaining within constraints.

Chapter 6

Overall Conclusions and Recommendations

The aerodynamic characteristics of wings of aspect ratio between 0.5 and 2.0 were experimentally determined at Reynolds numbers below 200,000. Of primary interest to this study were the effects of wing planform and aspect ratio on the forces and moments of LAR wings at low Re . Results showed large nonlinearities in the lift curves, specially for aspect ratios below 1.25. Definite differences in the performance of wings were seen between the different planforms, with the inverse Zimmerman and rectangular planforms being the most efficient of the planforms studied. Analysis of the wind tunnel data included the following: effects of Reynolds number, camber, and leading edge shape, location of the aerodynamic center, and stall angle of attack and maximum lift coefficient.

The experimental data was incorporated within an aerodynamic analysis procedure that used both empirical and analytical techniques to determine the performance of an aircraft design. This analysis procedure was made part of a design-optimization code based on a genetic algorithm optimization technique. The design-optimization procedure was used to optimize an aircraft given an example design problem. The design problem required the minimization of the maximum dimension of a MAV subject to specific constraints on the lift required, trim conditions, and longitudinal stability conditions. The genetic algorithm code applied to this problem, in conjunction with the aerodynamic analysis procedure based on wind tunnel data, yielded optimum MAV designs that satisfied all design requirements.

Some areas where further research would be warranted have become clear as a result of the present study. One such area would focus on interference effects of lifting surfaces and streamlined bodies for LAR wings at low Re . This particularly refers to a more detailed study of the effects of fuselage bodies on the drag and pitching moment of MAVs. Also suggested is a study of the interaction of the wing and horizontal tail, effects of the vertical locations of the two, and effects of flow separation near the trailing edge of wings and tails, specially in the cases when the control surfaces are located beyond the point of separation. A more thorough understanding of these aerodynamic effects would greatly aid in the design of more efficient MAVs and small UAVs.

Another topic which may be of interest is a more comprehensive study of effects of leading edge shape on the lift and (perhaps more importantly) pitching moment of LAR wings. Preliminary results presented within this report have shown that the leading edge has a dramatic influence on the pitching moment. Furthermore, this influence is highly Reynolds-number-dependent. A study of leading edge geometries would not only provide insight into the most efficient leading edge shapes for LAR wings, but would also be invaluable as a measure of how much care must be taken in the manufacturing of MAV wings.

References

- [1] M. A. Dornheim. Tiny drones may be soldier's new tool. *Aviation Week & Space Technology*, 148(23):42–48, June 8, 1998.
- [2] A. Pelletier and T. J. Mueller. Low Reynolds number aerodynamics of low-aspect-ratio, thin/flat/cambered-plate wings. *Journal of Aircraft*, 37(5):825–832, 2000.
- [3] C. H. Zimmerman. Characteristics of Clark Y airfoils of small aspect ratios. Technical Report TR 431, NACA, 1932.
- [4] G. E. Bartlett and R. J. Vidal. Experimental investigation of influence of edge shape on the aerodynamic characteristics of low aspect ratio wings at low speeds. *Journal of the Aeronautical Sciences*, 22(8):517–533, 1955.
- [5] K. L. Wadlin et al. The hydrodynamic characteristics of modified rectangular flat plates having aspect ratios of 1.00, 0.25, and 0.125 and operating near a free water surface. Technical Report TR 1246, NACA, 1955.
- [6] W. Bollay. A non-linear wing theory and its application to rectangular wings of small aspect ratio. *Zeitschrift Fur Angewandte Mathematik und Mechanik*, 19:21–35, 1939.
- [7] F. Weinig. Lift and drag of wings with small span. Technical Report TM 1151, NACA, 1947.
- [8] R. K. Bera and G. Suresh. Comments on the Lawrence equation for low-aspect-ratio wings. *J. of Aircraft*, 26(9):883–885, 1989.
- [9] E. C. Polhamus. A concept of the vortex lift of sharp-edge delta wings based on a leading-edge-suction analogy. Technical Report TN D-3767, NASA, 1966.
- [10] E. C. Polhamus. Predictions of vortex-lift characteristics by a leading-edge suction analogy. *J. of Aircraft*, 8(4):193–199, 1971.
- [11] S. C. Rajan and S. Shashidhar. Exact leading-term solution for low aspect ratio wings. *J. of Aircraft*, 34(4):571–573, 1997.
- [12] S. F. Hoerner. *Fluid-dynamic drag*. Hoerner Fluid Dynamics, Brick Town, NJ, 1965.
- [13] S. F. Hoerner and H. V. Borst. *Fluid-dynamic lift*. Hoerner Fluid Dynamics, Brick Town, NJ, 1975.

- [14] M. J. Hemsch and J. M. Luckring. Connection between leading-edge sweep, vortex lift, and vortex strength for delta wings. *J. of Aircraft*, 7(5):473–475, 1990.
- [15] C. H. Zimmerman. Aerodynamic characteristics of several airfoils of low aspect ratio. Technical Report TN 539, NACA, 1935.
- [16] T. J. Mueller. Aerodynamic measurements at low Reynolds numbers for fixed wing micro-air vehicles. In *Development and operation of UAVs for military and civil applications*, RTO Educational Note 9, chapter 8. NATO, April 2000.
- [17] R. C. Pankhurst and D. W. Holder. *Wind-tunnel technique*. Sir Isaac Pitman & Sons, Ltd., London, 1952.
- [18] W. H. Jr. Rae and A. Pope. *Low-speed wind tunnel testing*. John Wiley & Sons, New York, 1984.
- [19] S. J. Kline and F. A. McClintock. Describing uncertainties in single-sample experiments. *Mechanical Engineering*, 75(1):3–8, 1953.
- [20] Torres G. E. and T. J. Mueller. Aerodynamic characteristics of low aspect ratio wings at low Reynolds numbers. In T. J. Mueller, editor, *Fixed and flapping wing aerodynamics for micro air vehicle applications*, volume 195 of *Progress in Astronautics and Aeronautics*, pages 115–141. AIAA, Reston, Virginia, 2001.
- [21] C. A. Brown. The effect of camber on thin plate low aspect ratio wings at low Reynolds numbers. Master's thesis, University of Notre Dame, Notre Dame, IN, USA, April 2001.
- [22] A. D. Belegundu and T. R. Chandrupatla. *Optimization concepts and applications in engineering*. Prentice Hall, New Jersey, 1999.
- [23] B. Etkin and L. D. Reid. *Dynamics of flight: stability and control*. John Wiley & Sons, New York, 1996.

Appendix A

Aerodynamic Results

A.1 Aerodynamic Results: Constant Aspect Ratio

This section shows plots of experimental results for constant aspect ratio. That is, each plot contains curves corresponding to each of the four wing planforms at a given aspect ratio. These graphs are useful to compare different planforms while holding AR constant. The curves plotted are:

1. C_L versus α at $Re = 100,000$
2. C_D versus α at $Re = 100,000$
3. C_L versus C_D at $Re = 100,000$
4. L/D versus α at $Re = 100,000$
5. C_M versus α at $Re = 140,000$
6. h_{AC} versus α at $Re = 140,000$

Figure Numbers	Page Number	Description
AR = 0.50		
A.1 to A.4	78	C_L vs. α , C_D vs. α , C_L vs. C_D , and L/D vs. α All four wing planforms at $Re = 100,000$
AR = 0.75		
A.5 to A.8	80	C_L vs. α , C_D vs. α , C_L vs. C_D , and L/D vs. α All four wing planforms at $Re = 100,000$
A.9 and A.10	82	C_M vs. α and h_{AC} vs. α All four wing planforms at $Re = 140,000$
AR = 1.00		
A.11 to A.14	83	C_L vs. α , C_D vs. α , C_L vs. C_D , and L/D vs. α All four wing planforms at $Re = 100,000$
A.15 and A.16	85	C_M vs. α and h_{AC} vs. α All four wing planforms at $Re = 140,000$
AR = 1.25		
A.17 to A.20	86	C_L vs. α , C_D vs. α , C_L vs. C_D , and L/D vs. α All four wing planforms at $Re = 100,000$
A.21 and A.22	88	C_M vs. α and h_{AC} vs. α All four wing planforms at $Re = 140,000$
AR = 1.50		
A.23 to A.26	89	C_L vs. α , C_D vs. α , C_L vs. C_D , and L/D vs. α All four wing planforms at $Re = 100,000$
A.27 and A.28	91	C_M vs. α and h_{AC} vs. α All four wing planforms at $Re = 140,000$
AR = 1.75		
A.29 to A.32	92	C_L vs. α , C_D vs. α , C_L vs. C_D , and L/D vs. α All four wing planforms at $Re = 100,000$
A.33 and A.34	94	C_M vs. α and h_{AC} vs. α All four wing planforms at $Re = 140,000$
AR = 2.00		
A.35 to A.38	95	C_L vs. α , C_D vs. α , C_L vs. C_D , and L/D vs. α All four wing planforms at $Re = 100,000$
A.39 and A.40	97	C_M vs. α and h_{AC} vs. α All four wing planforms at $Re = 140,000$

Table A.1: Summary of Plots for Constant AR

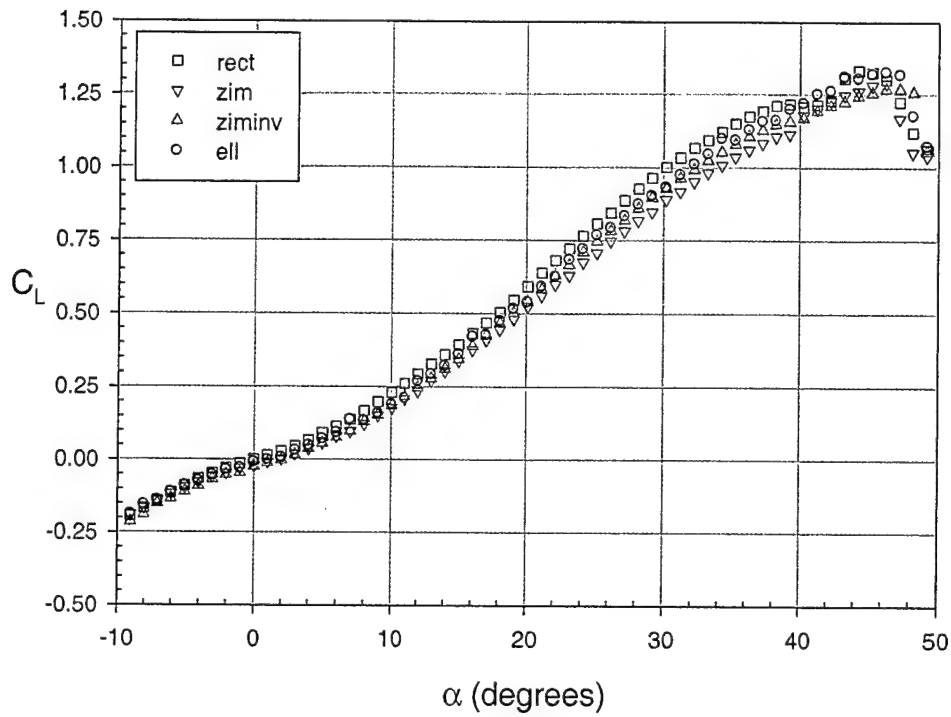


Figure A.1: C_L vs. α , $AR=0.50$, $Re_c=100,000$

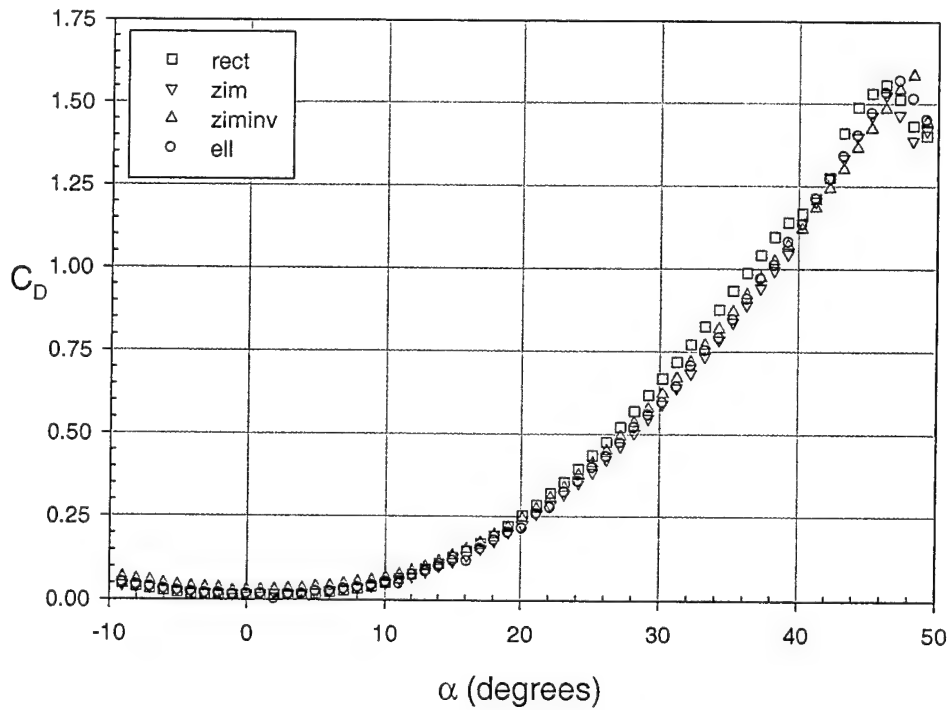


Figure A.2: C_D vs. α , $AR=0.50$, $Re_c=100,000$

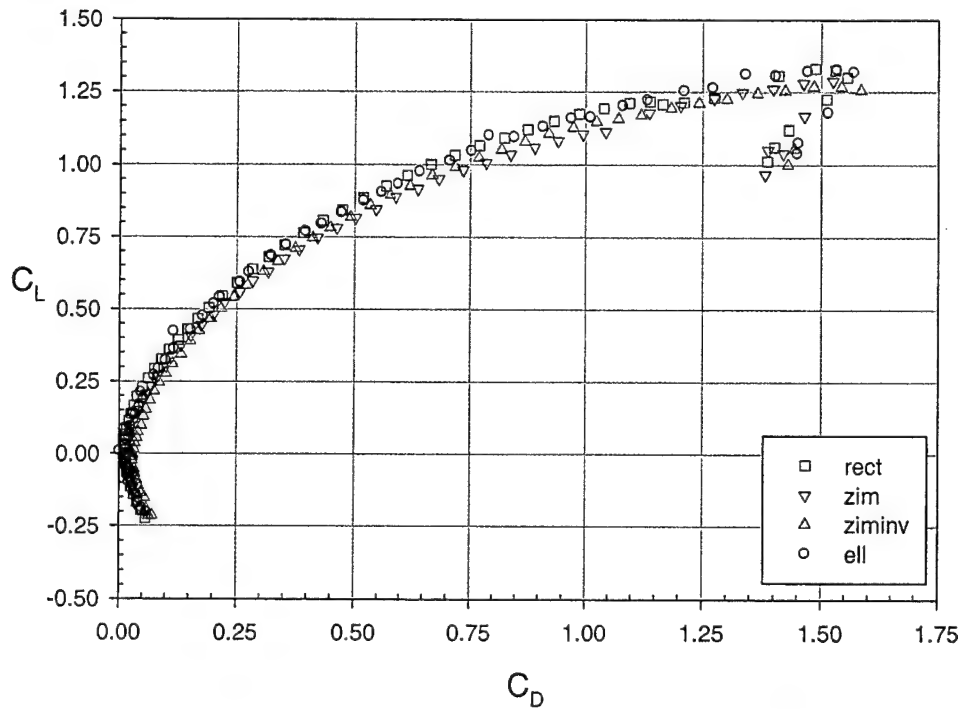


Figure A.3: C_L vs. C_D , $AR=0.50$, $Re_c=100,000$

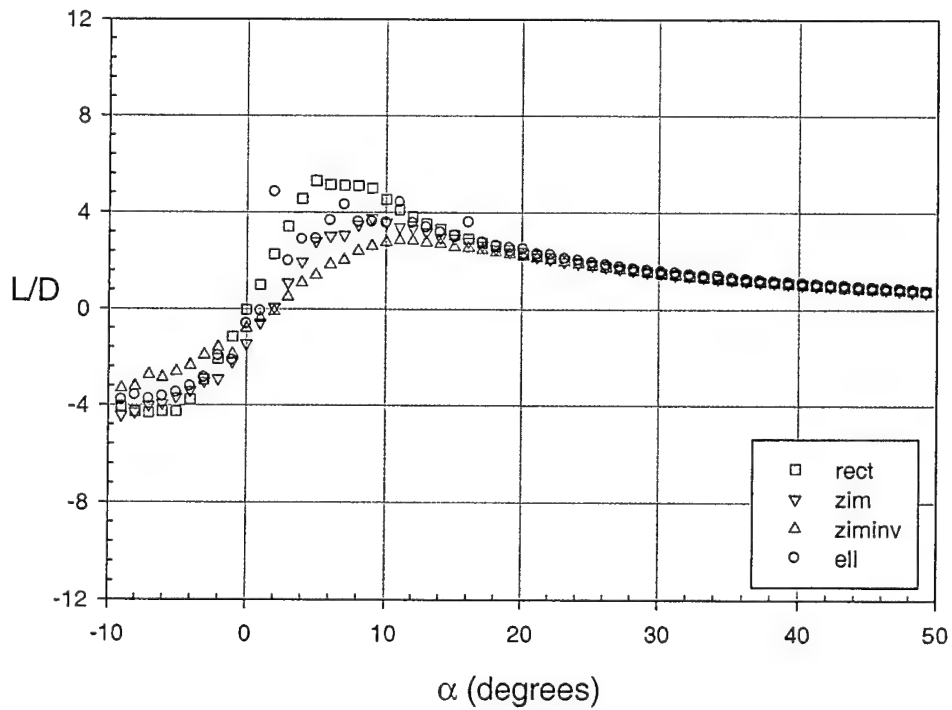


Figure A.4: L/D vs. α , $AR=0.50$, $Re_c=100,000$

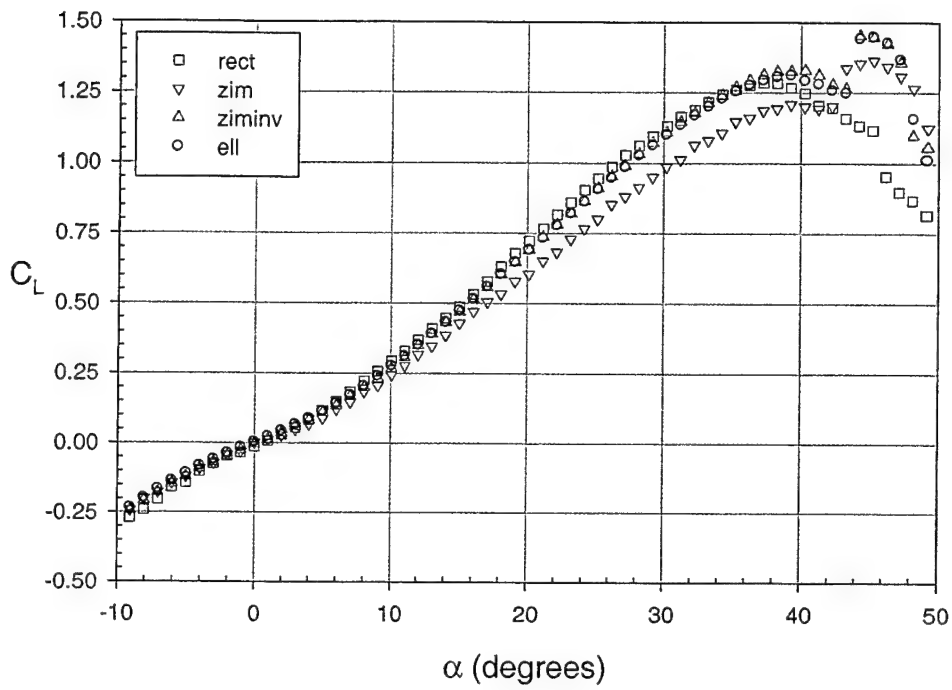


Figure A.5: C_L vs. α , $AR=0.75$, $Re_c=100,000$

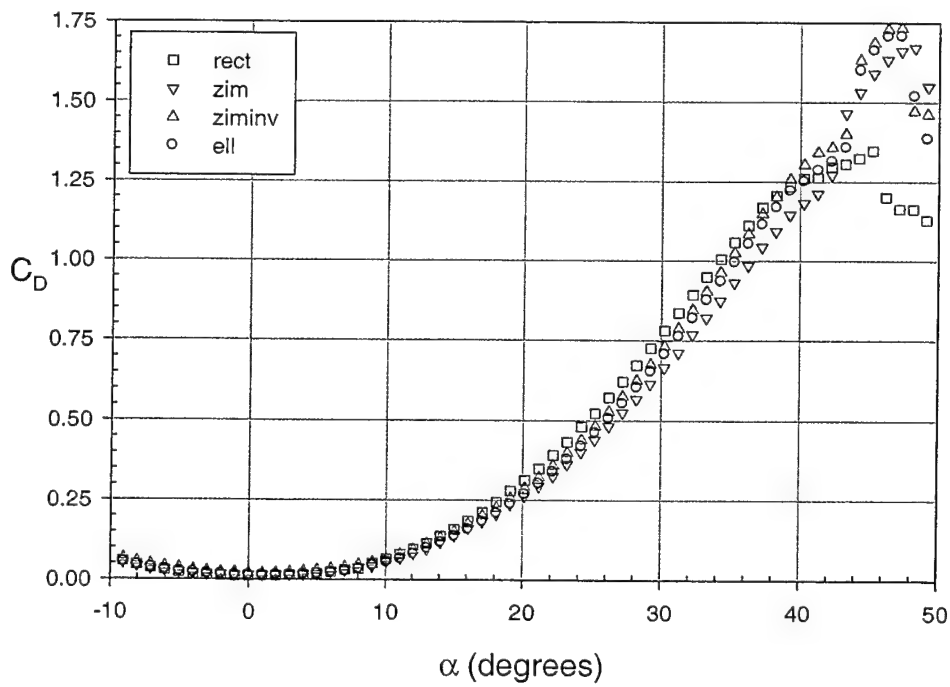


Figure A.6: C_D vs. α , $AR=0.75$, $Re_c=100,000$

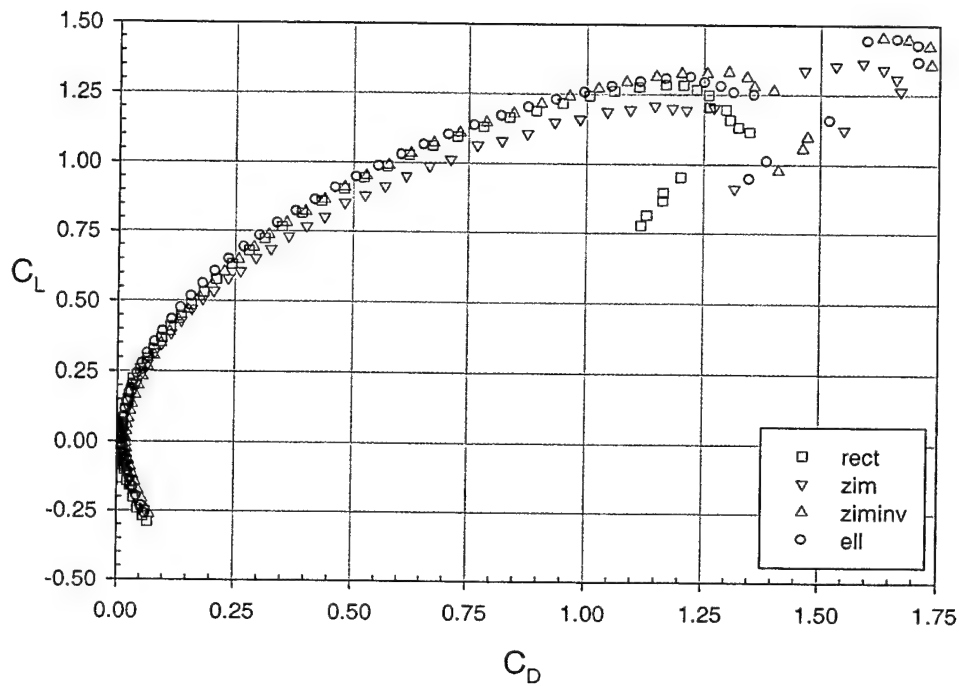


Figure A.7: C_L vs. C_D , $AR=0.75$, $Re_c=100,000$

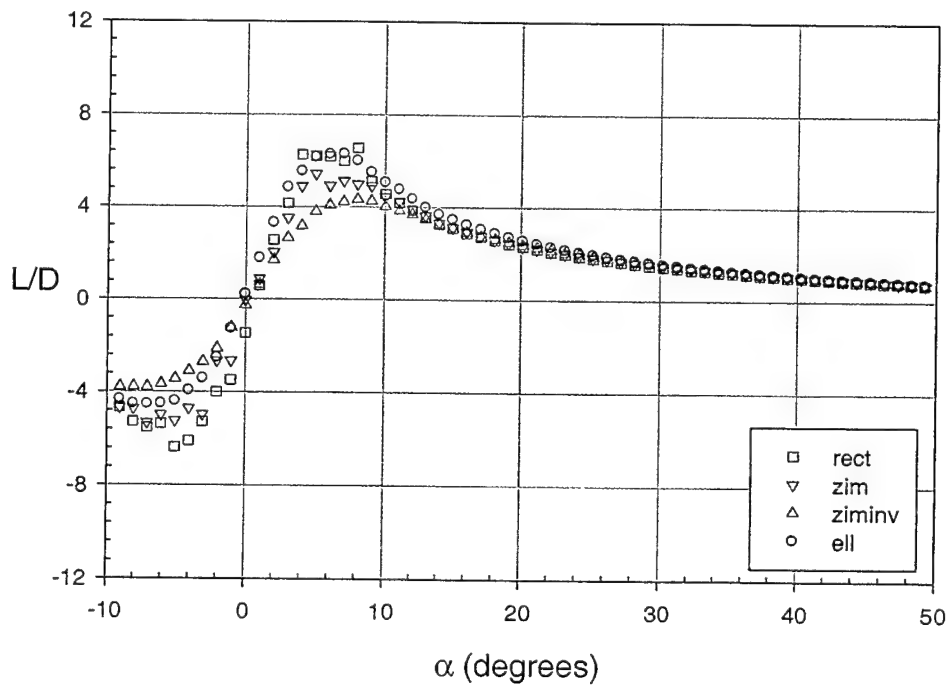


Figure A.8: L/D vs. α , $AR=0.75$, $Re_c=100,000$

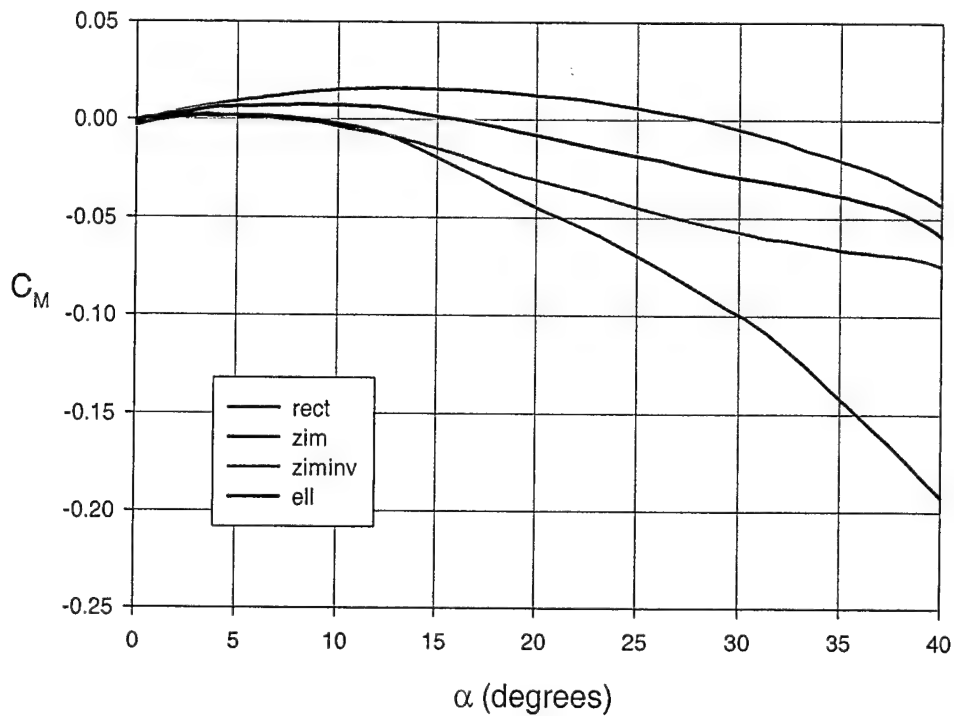


Figure A.9: C_M vs. α , $AR=0.75$, $Re_c=140,000$

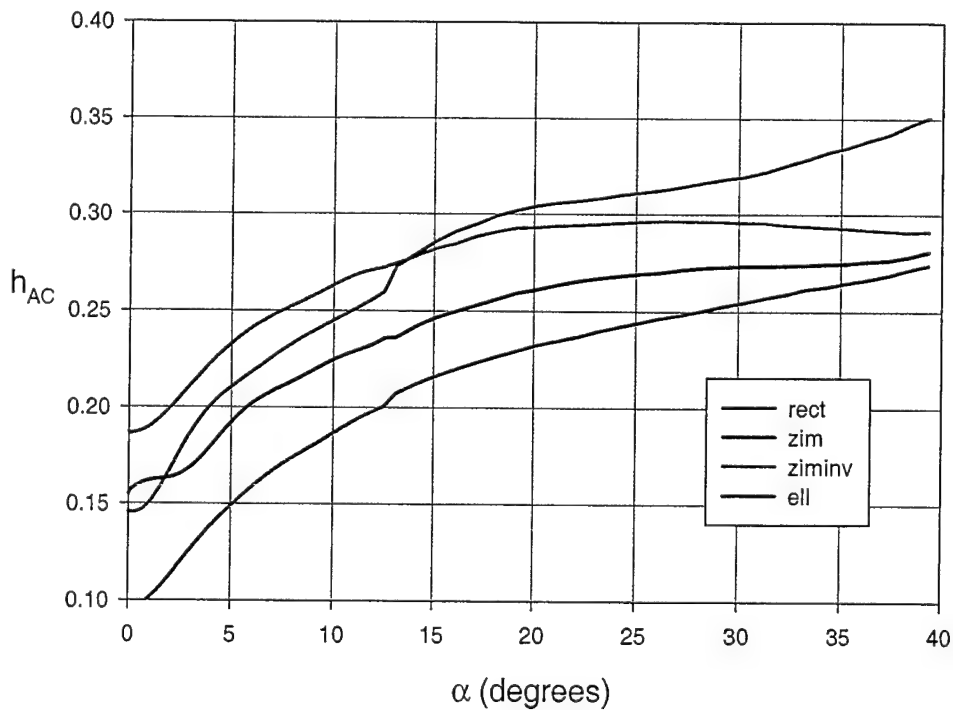


Figure A.10: h_{AC} vs. α , $AR=0.75$, $Re_c=140,000$

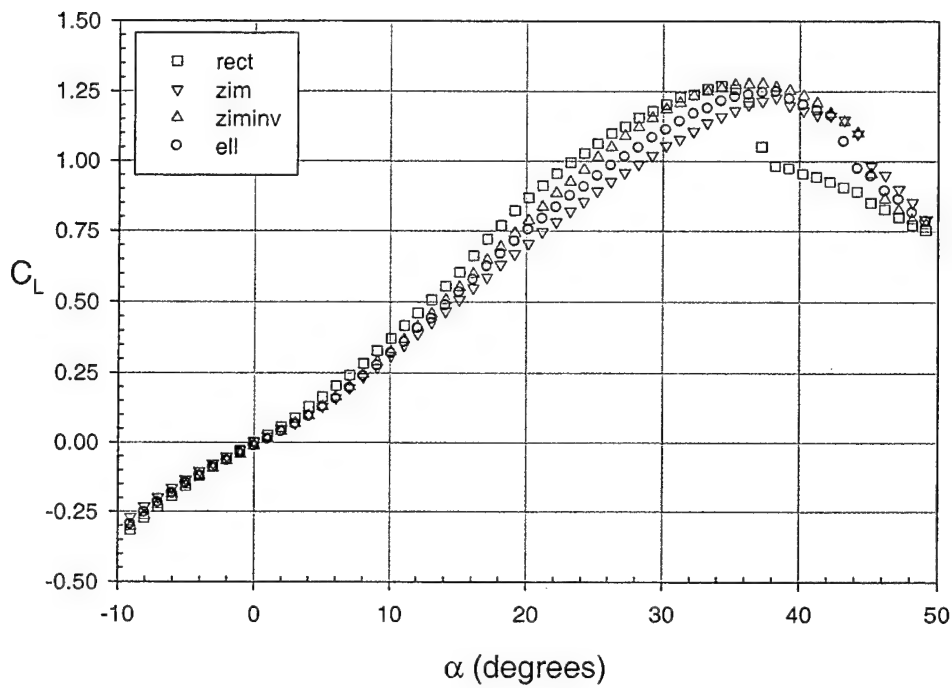


Figure A.11: C_L vs. α , $AR=1.00$, $Re_c=100,000$

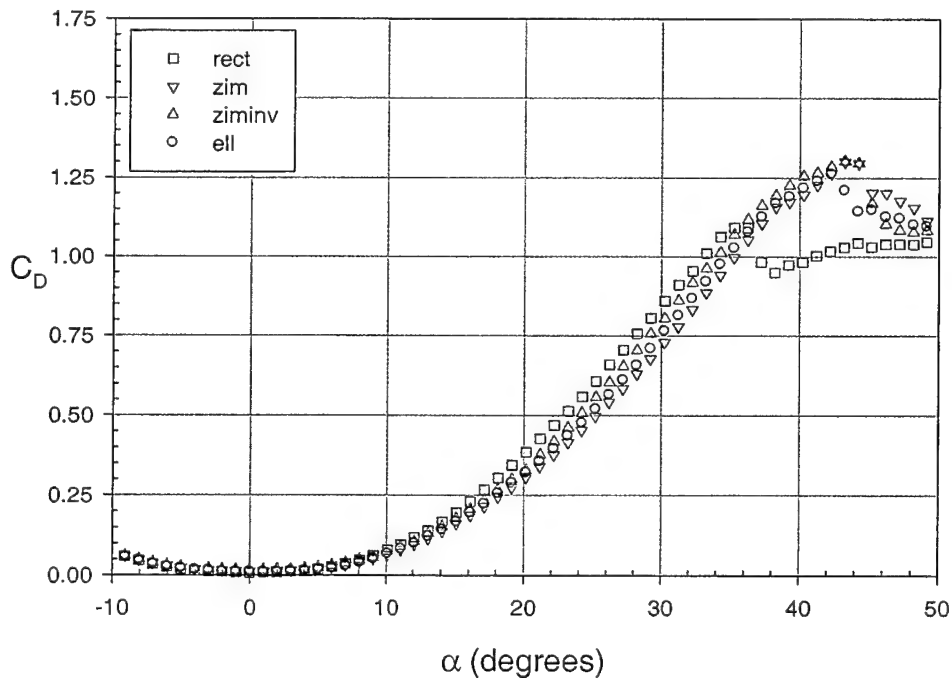


Figure A.12: C_D vs. α , $AR=1.00$, $Re_c=100,000$

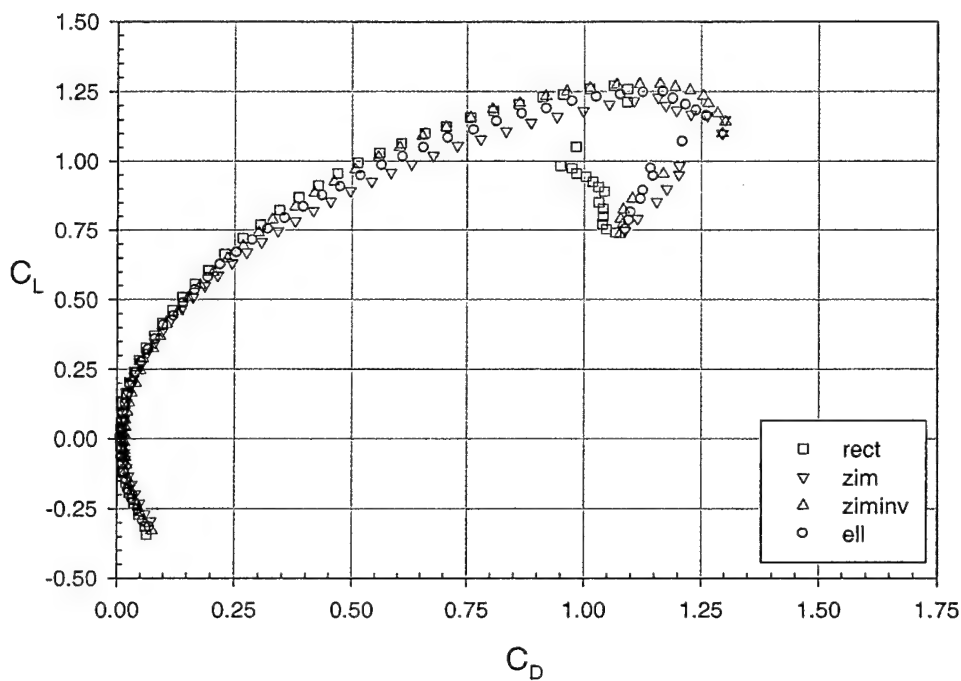


Figure A.13: C_L vs. C_D , $AR = 1.00$, $Re_c = 100,000$

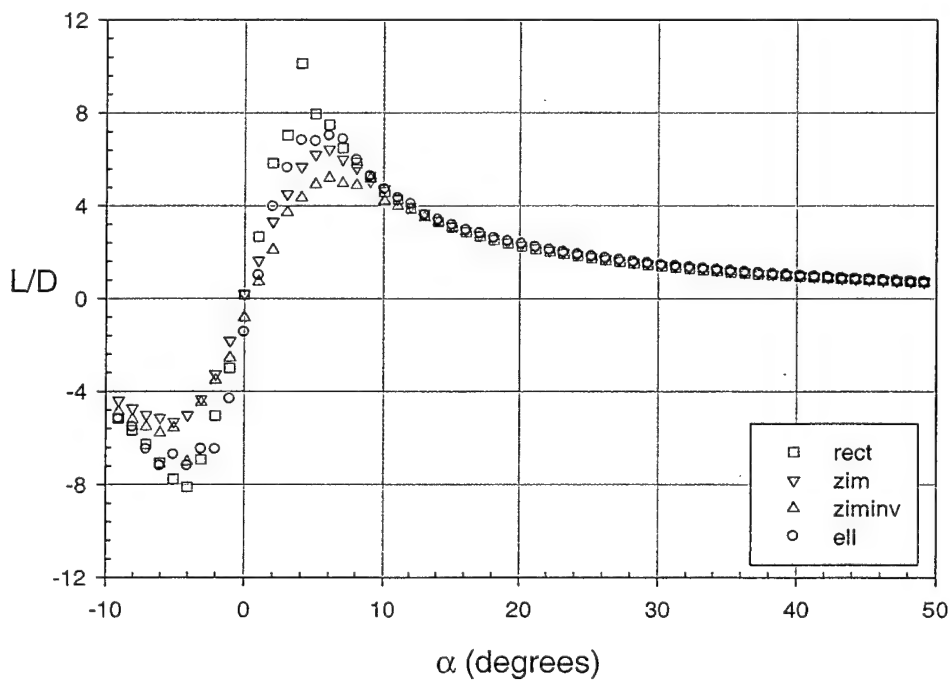


Figure A.14: L/D vs. α , $AR = 1.00$, $Re_c = 100,000$

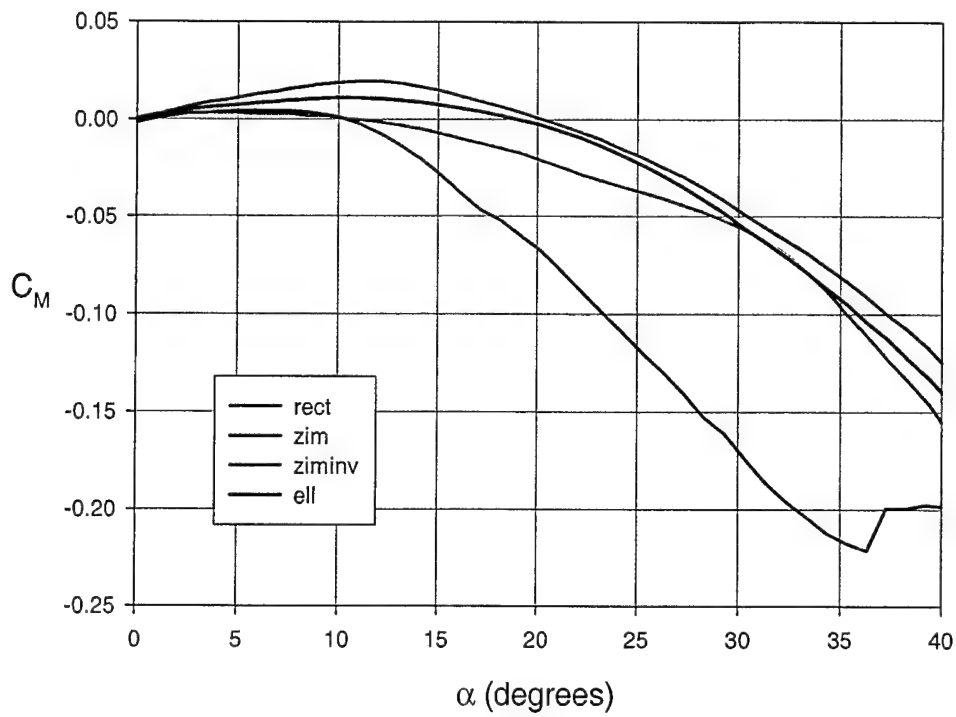


Figure A.15: C_M vs. α , $AR=1.00$, $Re_c=140,000$

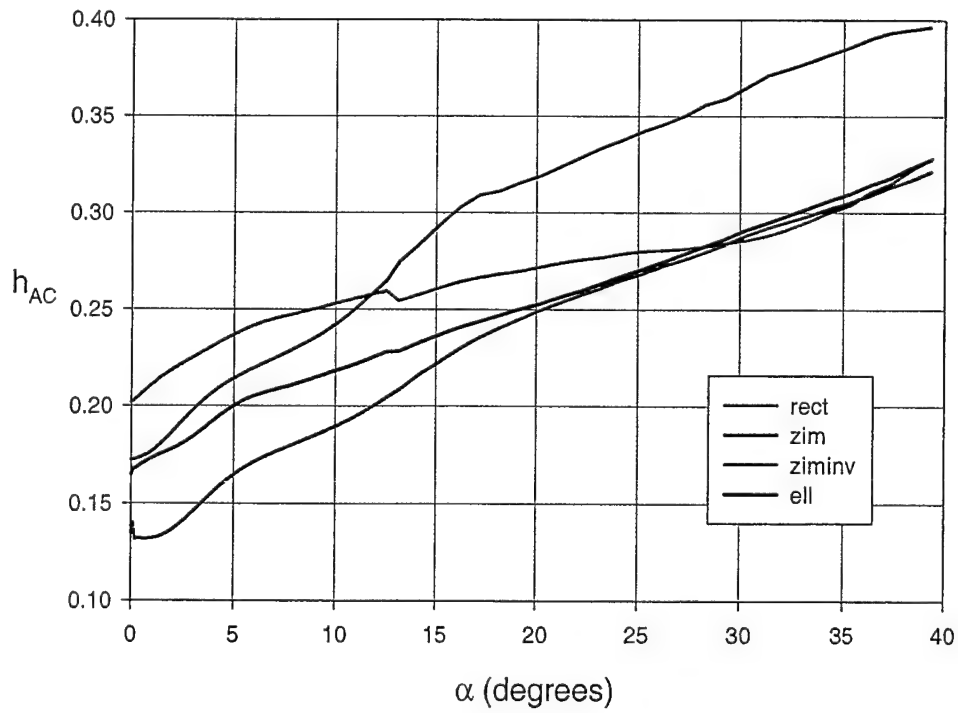


Figure A.16: h_{AC} vs. α , $AR=1.00$, $Re_c=140,000$

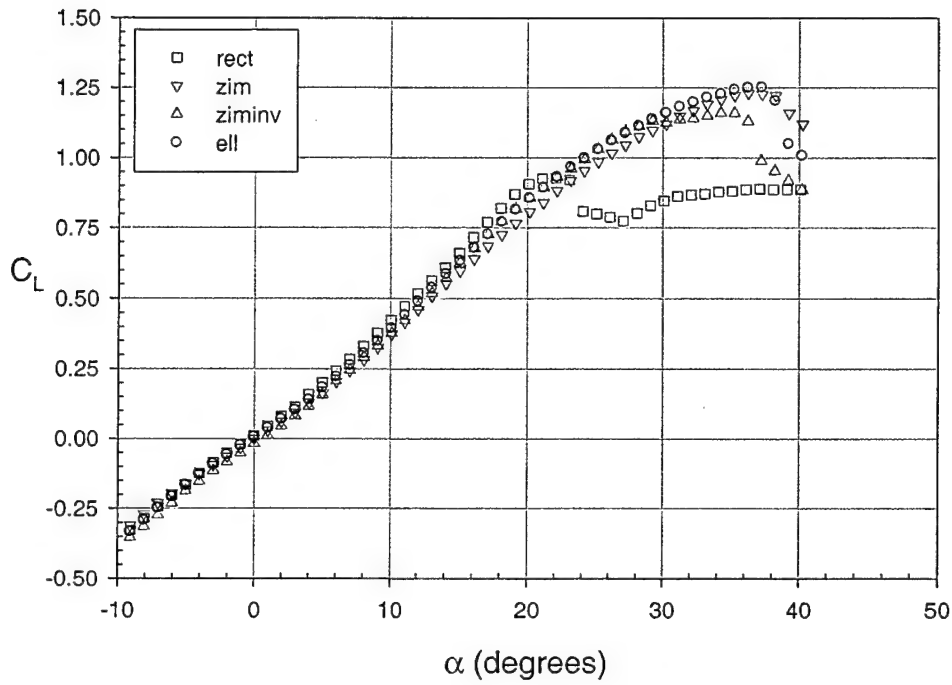


Figure A.17: C_L vs. α , $AR=1.25$, $Re_c=100,000$

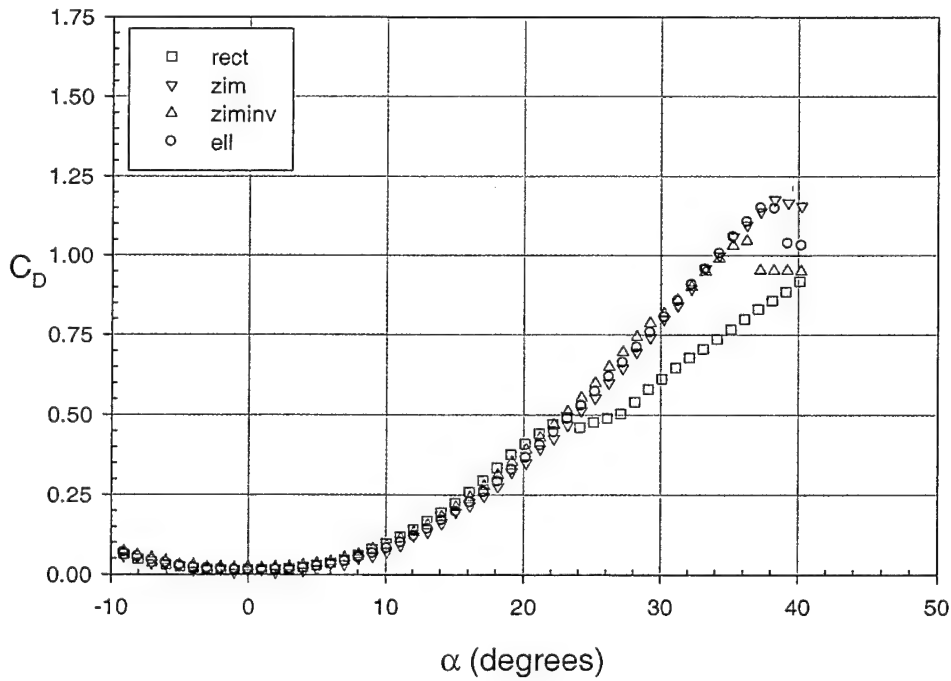


Figure A.18: C_D vs. α , $AR=1.25$, $Re_c=100,000$

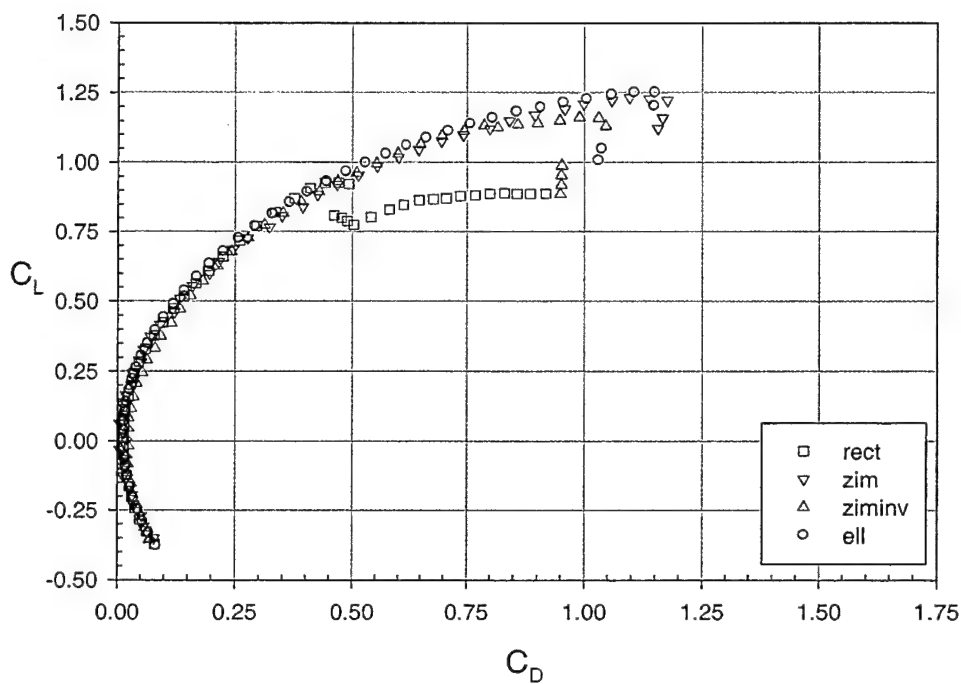


Figure A.19: C_L vs. C_D , $AR = 1.25$, $Re_c = 100,000$

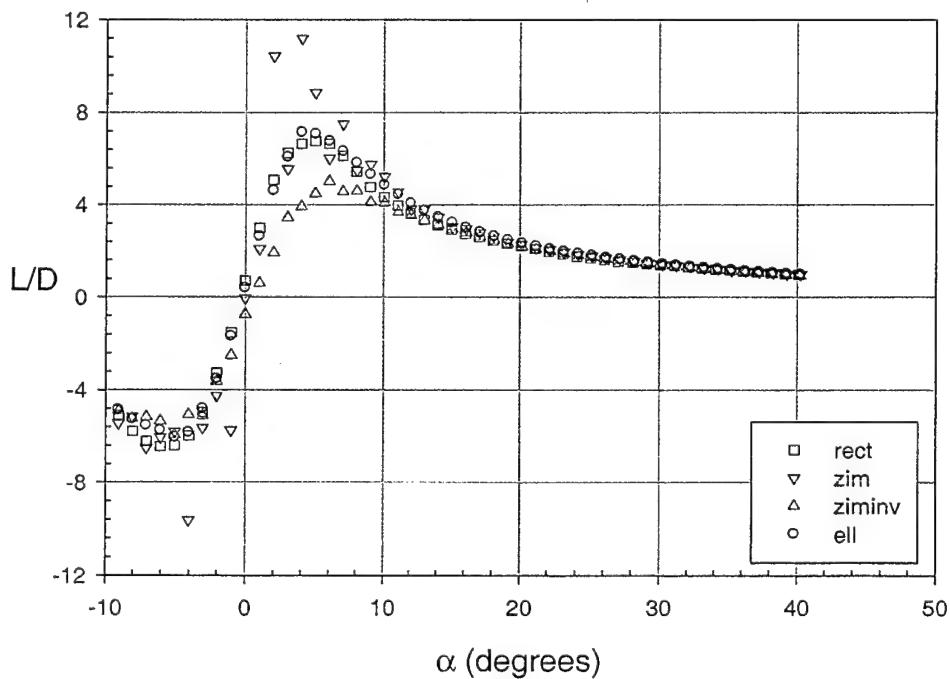


Figure A.20: L/D vs. α , $AR = 1.25$, $Re_c = 100,000$

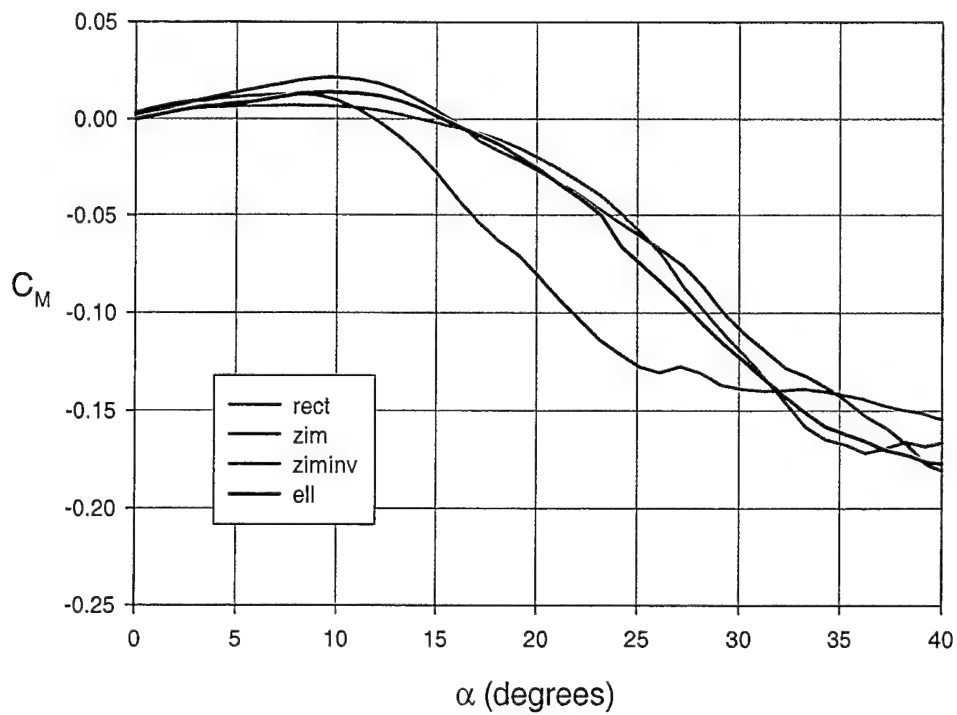


Figure A.21: C_M vs. α , $AR = 1.25$, $Re_c = 140,000$

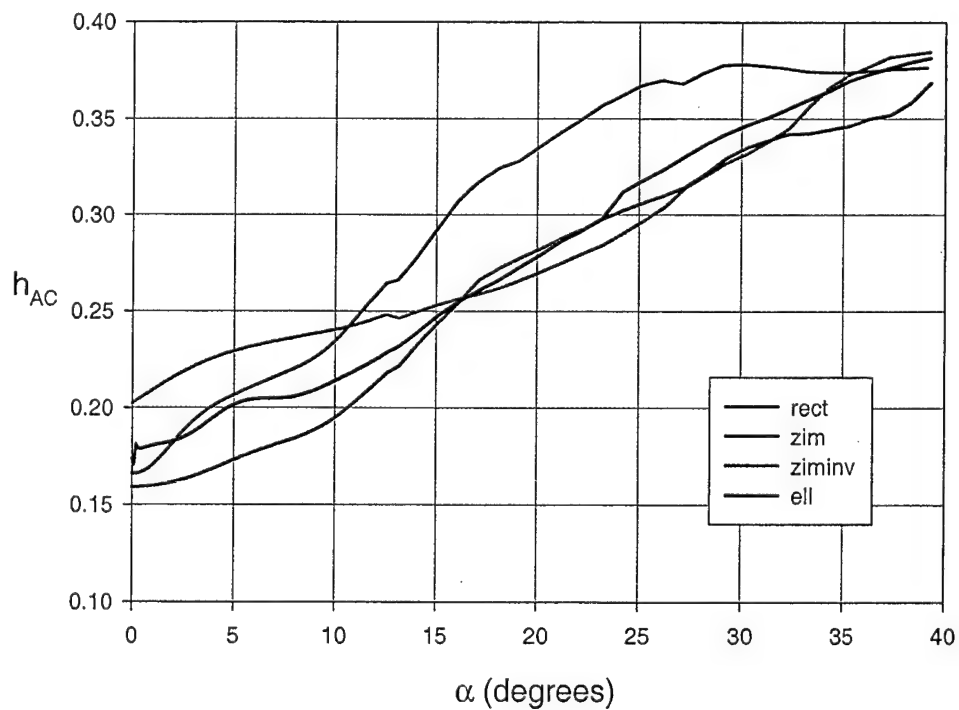


Figure A.22: h_{AC} vs. α , $AR = 1.25$, $Re_c = 140,000$

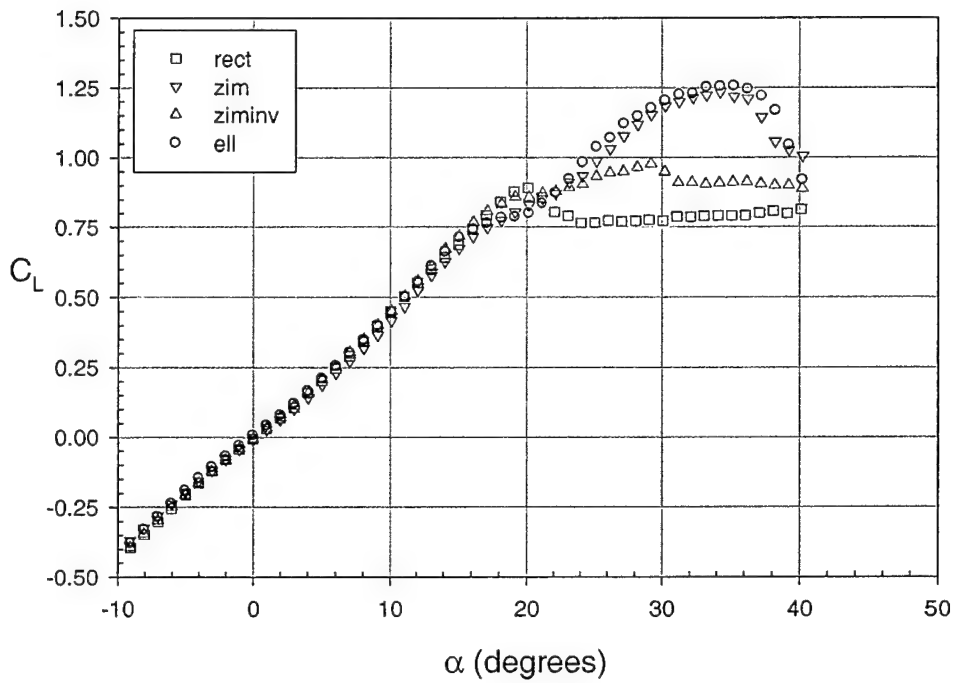


Figure A.23: C_L vs. α , $AR=1.50$, $Re_c=100,000$

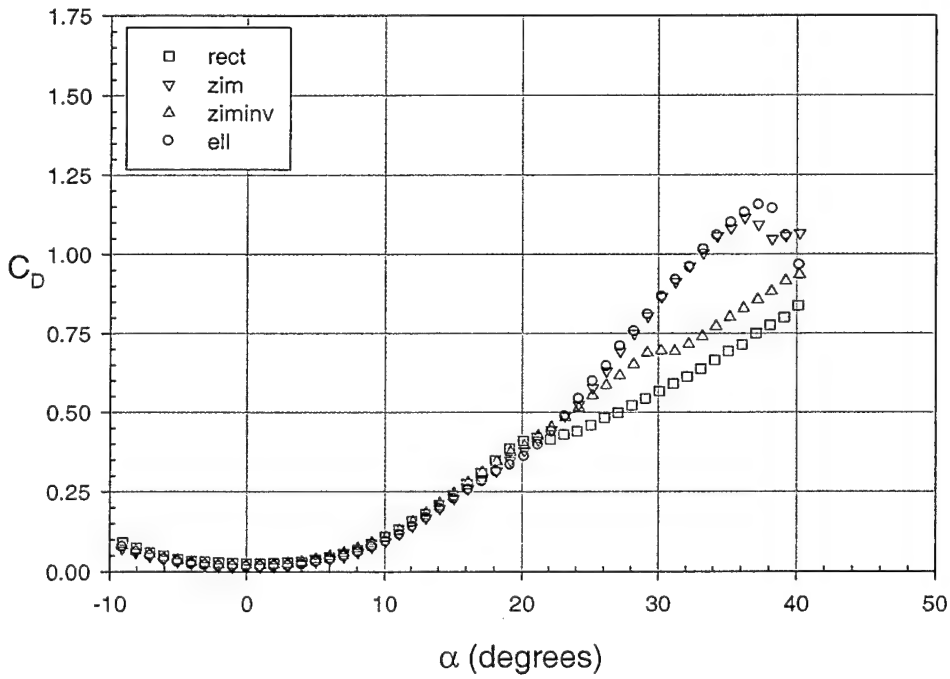


Figure A.24: C_D vs. α , $AR=1.50$, $Re_c=100,000$

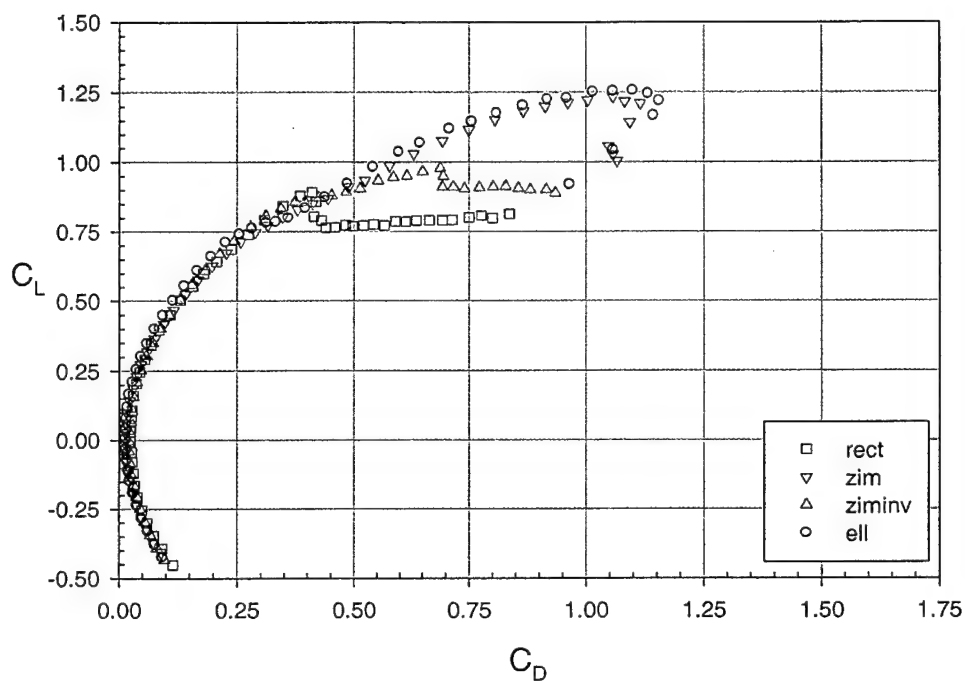


Figure A.25: C_L vs. C_D , $AR=1.50$, $Re_c=100,000$

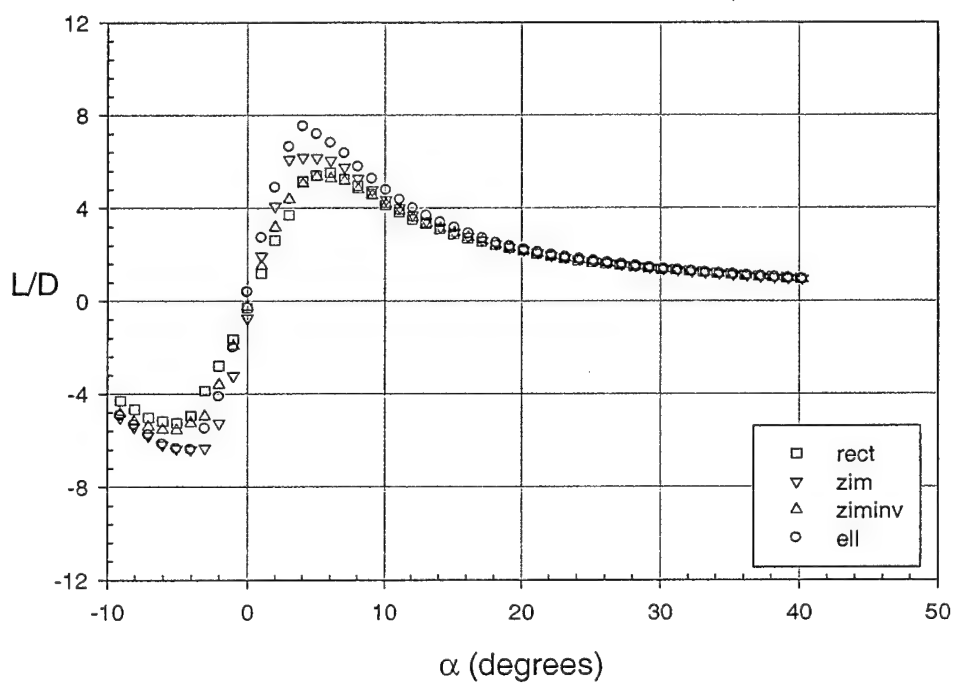


Figure A.26: L/D vs. α , $AR=1.50$, $Re_c=100,000$

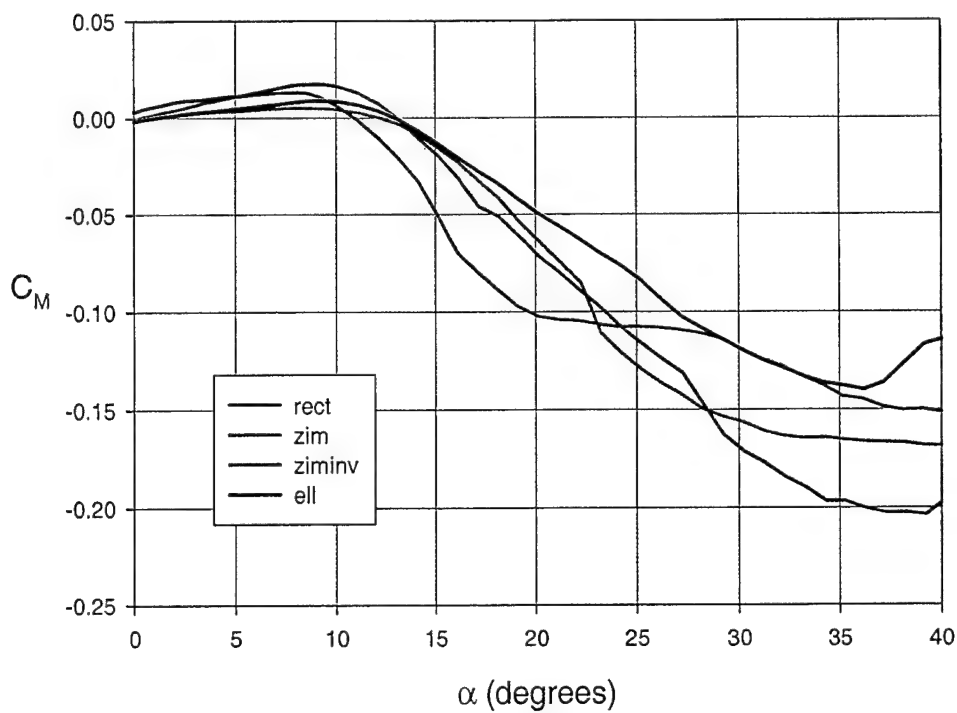


Figure A.27: C_M vs. α , $AR = 1.50$, $Re_c = 140,000$

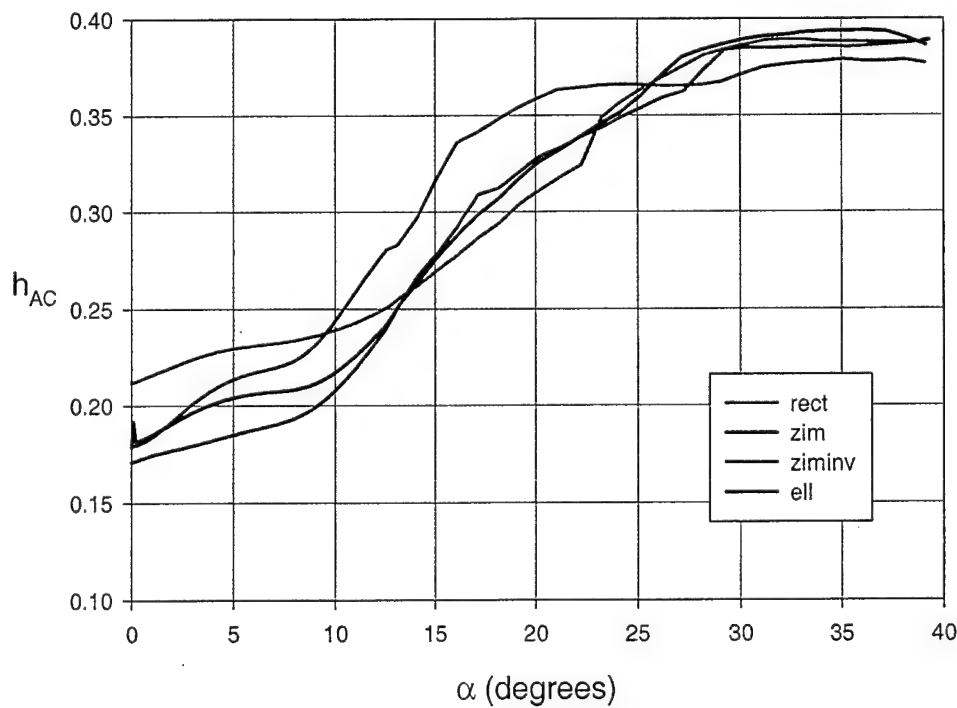


Figure A.28: h_{AC} vs. α , $AR = 1.50$, $Re_c = 140,000$

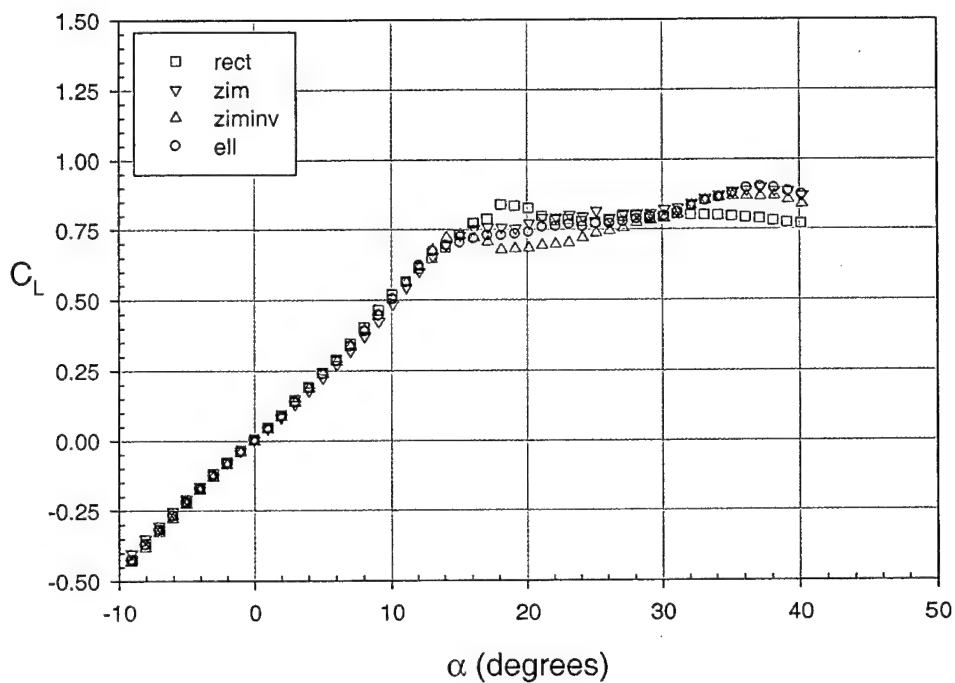


Figure A.29: C_L vs. α , $AR=1.75$, $Re_c=100,000$

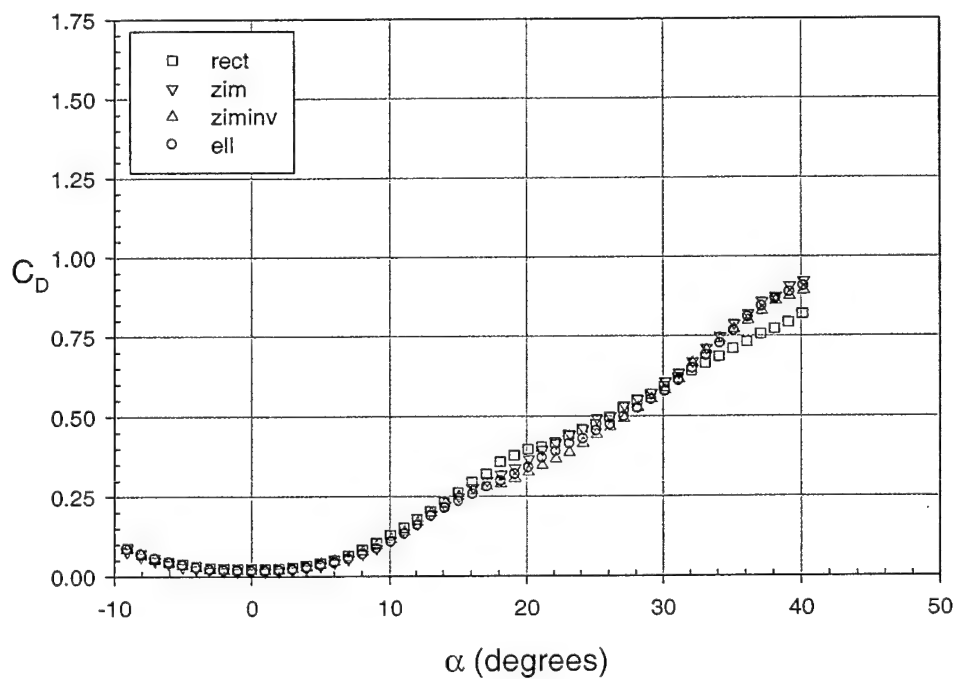


Figure A.30: C_D vs. α , $AR=1.75$, $Re_c=100,000$

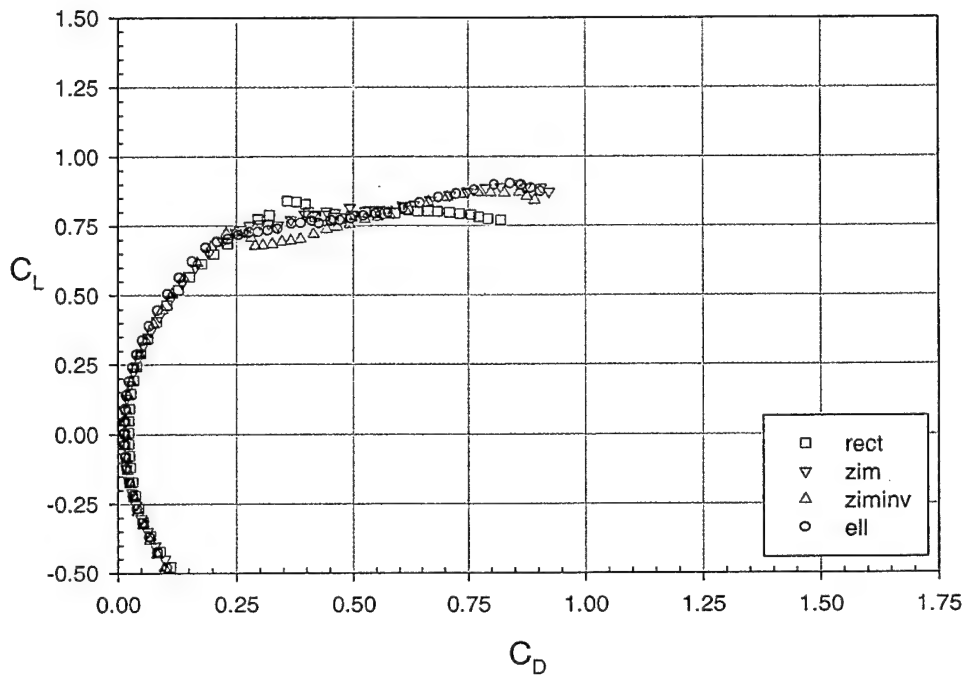


Figure A.31: C_L vs. C_D , $AR=1.75$, $Re_c=100,000$

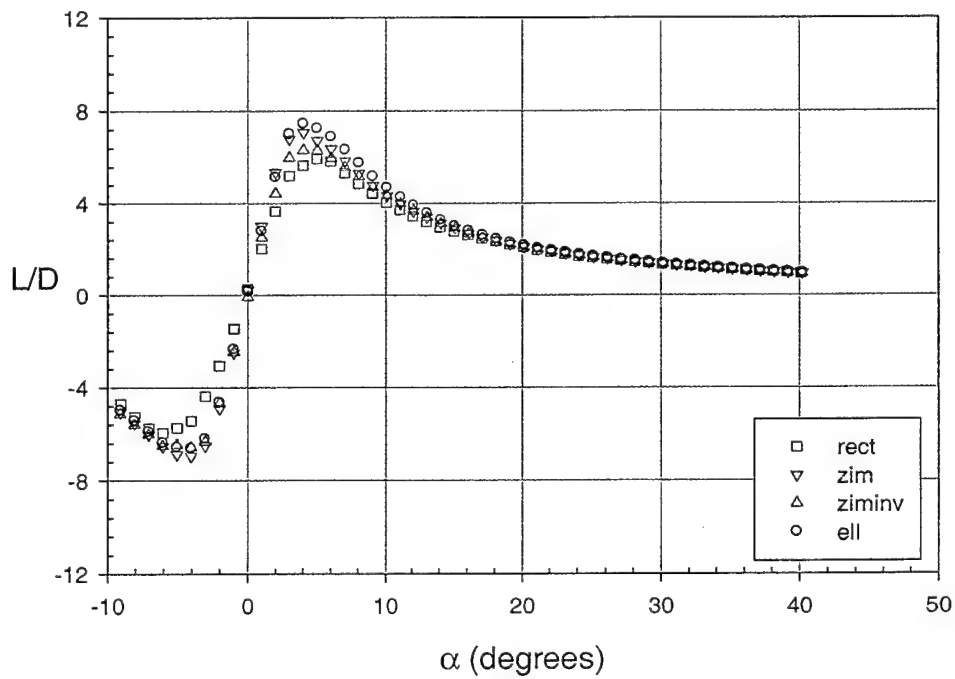


Figure A.32: L/D vs. α , $AR=1.75$, $Re_c=100,000$

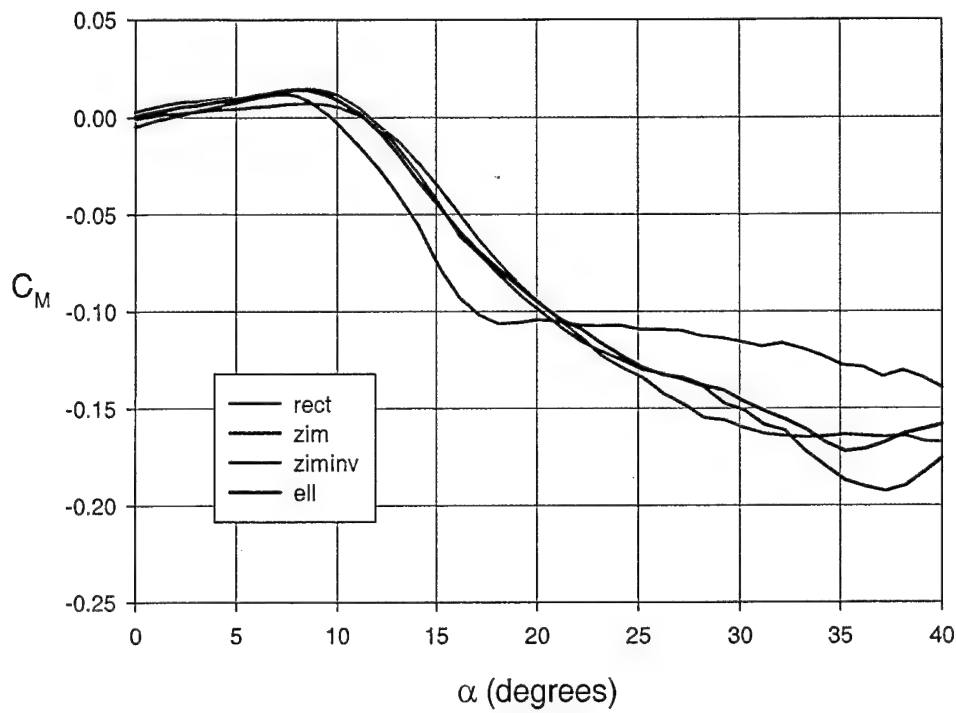


Figure A.33: C_M vs. α , $AR = 1.75$, $Re_c = 140,000$

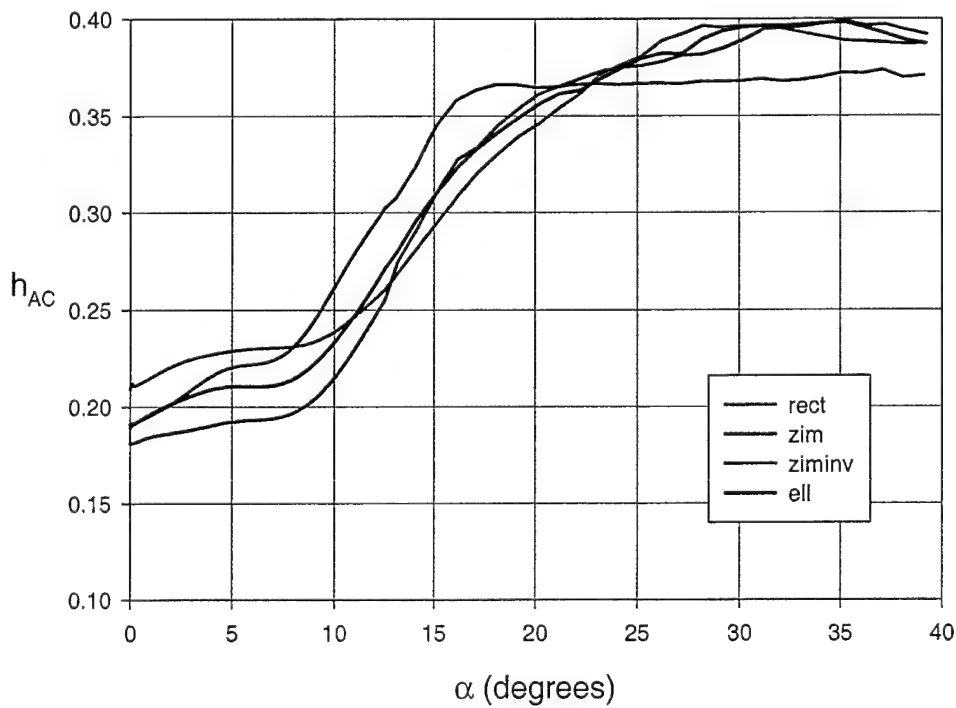


Figure A.34: h_{AC} vs. α , $AR = 1.75$, $Re_c = 140,000$

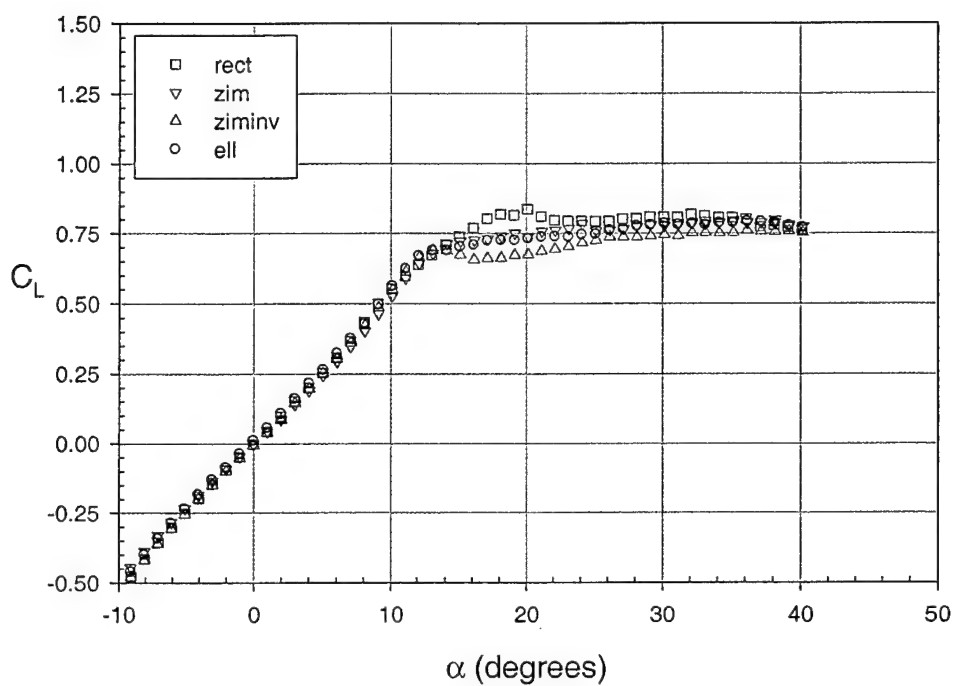


Figure A.35: C_L vs. α , $AR = 2.00$, $Re_c = 100,000$

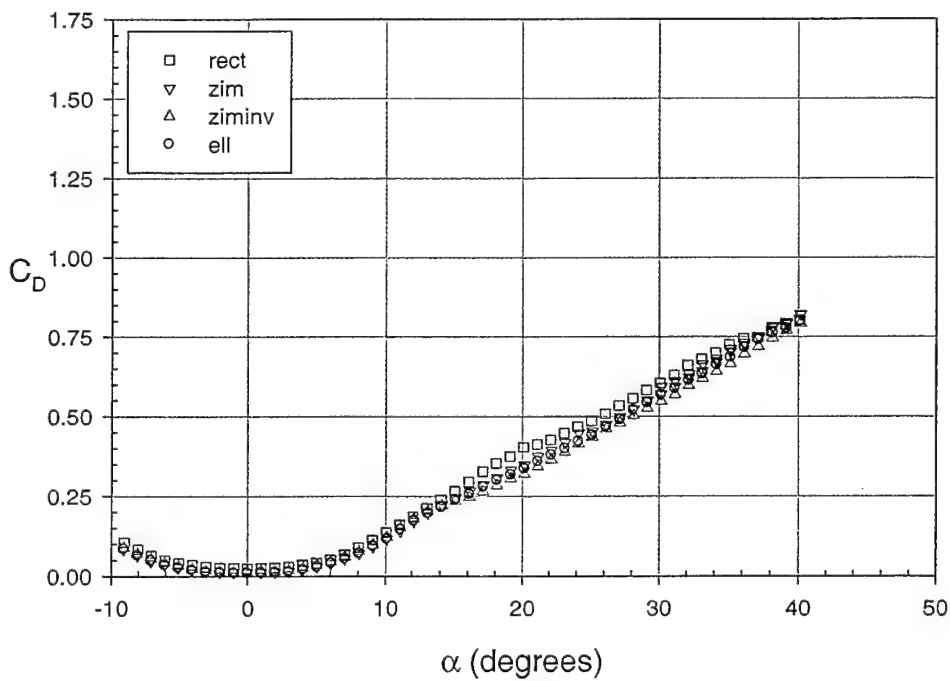


Figure A.36: C_D vs. α , $AR = 2.00$, $Re_c = 100,000$

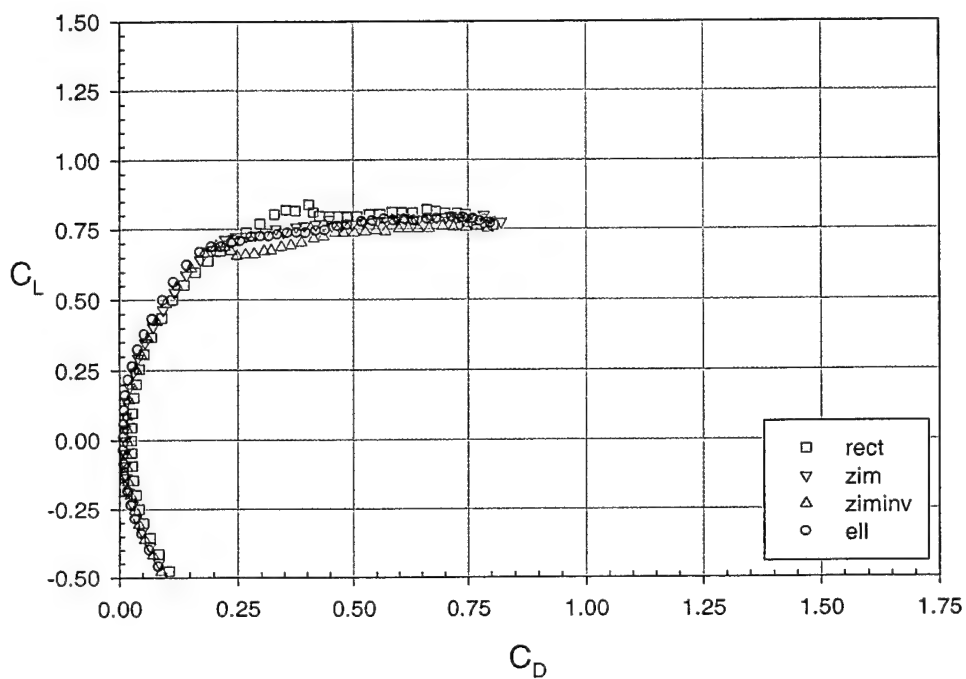


Figure A.37: C_L vs. C_D , $AR = 2.00$, $Re_c = 100,000$

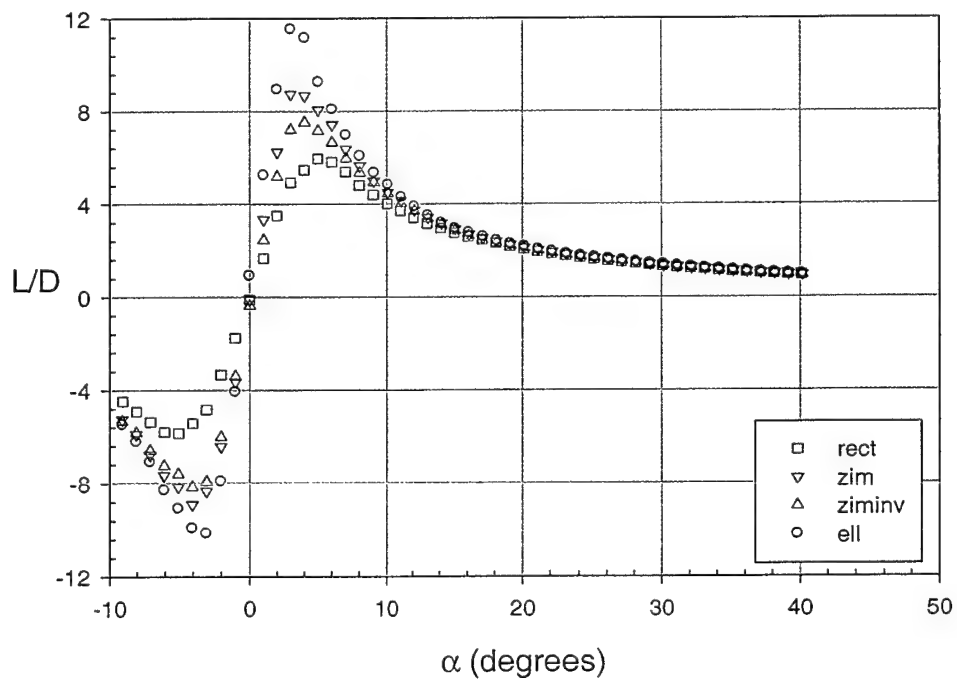


Figure A.38: L/D vs. α , $AR = 2.00$, $Re_c = 100,000$

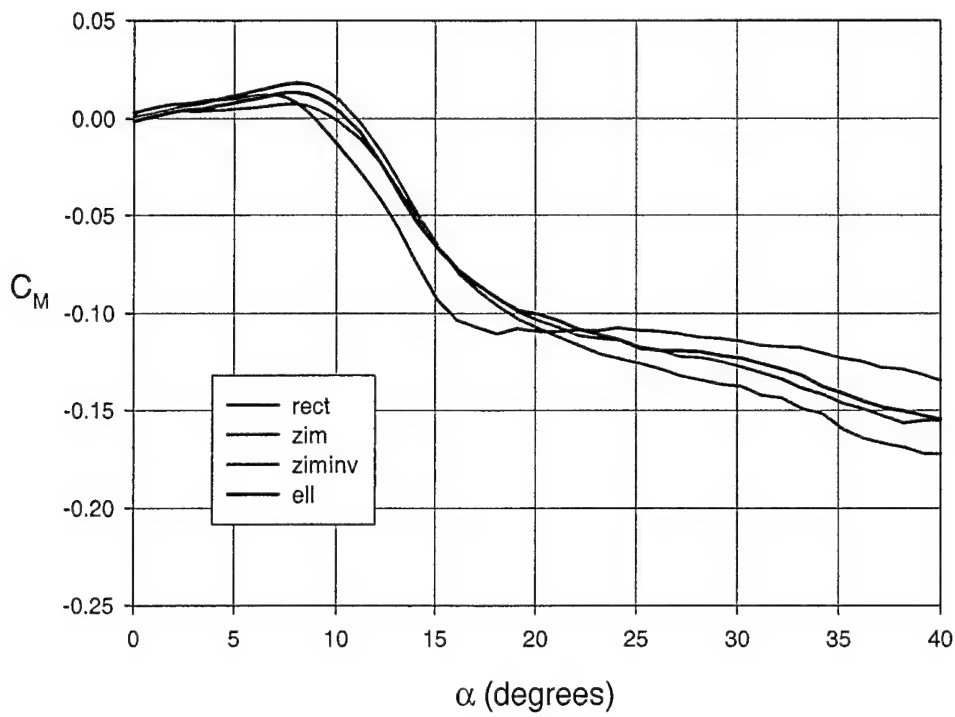


Figure A.39: C_M vs. α , $AR=2.00$, $Re_c=140,000$

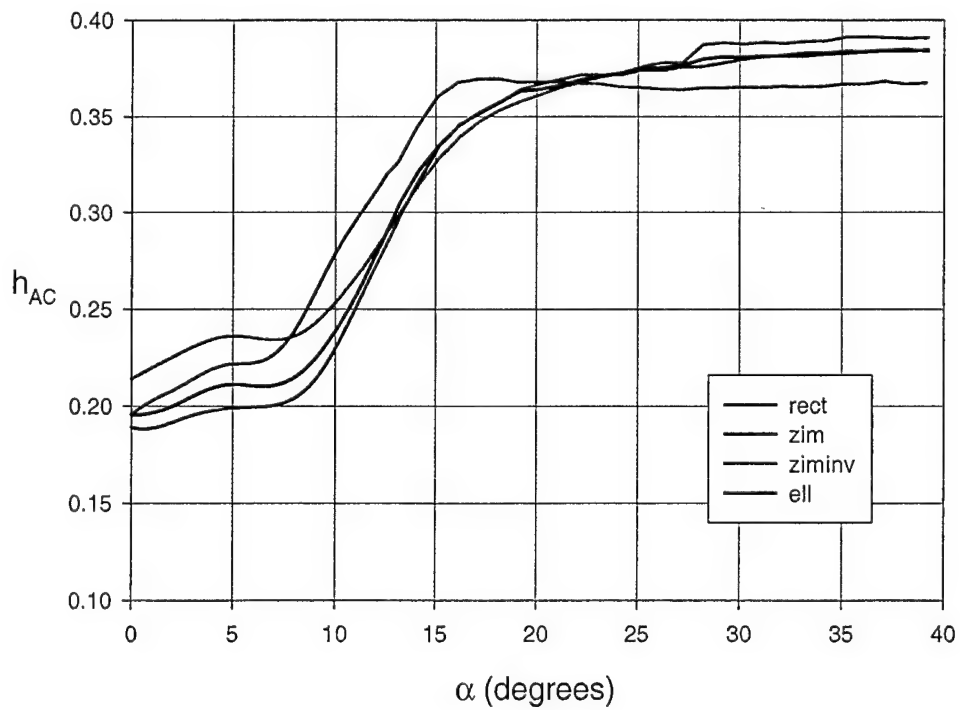


Figure A.40: h_{AC} vs. α , $AR=2.00$, $Re_c=140,000$

A.2 Aerodynamic Results: Constant Wing Planform

This section shows plots of experimental results for constant planform. Each plot contains curves corresponding to each of the seven aspect ratios for a given wing planform. These graphs are useful to determine the effect of varying aspect ratio. The curves plotted are:

1. C_L versus α at $Re = 100,000$
2. C_D versus α at $Re = 100,000$
3. C_L versus C_D at $Re = 100,000$
4. L/D versus α at $Re = 100,000$
5. C_M versus α at $Re = 140,000$
6. h_{AC} versus α at $Re = 140,000$

Figure Numbers	Page Number	Description
Rectangular Planform		
A.41 to A.44	99	C_L vs. α , C_D vs. α , C_L vs. C_D , and L/D vs. α All seven aspect ratios ($0.50 \leq AR \leq 2.00$) at $Re = 100,000$
A.45 and A.46	101	C_M vs. α and h_{AC} vs. α Six aspect ratios ($0.75 \leq AR \leq 2.00$) at $Re = 140,000$
Zimmerman Planform		
A.47 to A.50	102	C_L vs. α , C_D vs. α , C_L vs. C_D , and L/D vs. α All seven aspect ratios ($0.50 \leq AR \leq 2.00$) at $Re = 100,000$
A.51 and A.52	104	C_M vs. α and h_{AC} vs. α Six aspect ratios ($0.75 \leq AR \leq 2.00$) at $Re = 140,000$
Inverse Zimmerman Planform		
A.53 to A.56	105	C_L vs. α , C_D vs. α , C_L vs. C_D , and L/D vs. α All seven aspect ratios ($0.50 \leq AR \leq 2.00$) at $Re = 100,000$
A.57 and A.58	107	C_M vs. α and h_{AC} vs. α Six aspect ratios ($0.75 \leq AR \leq 2.00$) at $Re = 140,000$
Elliptical Planform		
A.59 to A.62	108	C_L vs. α , C_D vs. α , C_L vs. C_D , and L/D vs. α All seven aspect ratios ($0.50 \leq AR \leq 2.00$) at $Re = 100,000$
A.63 and A.64	110	C_M vs. α and h_{AC} vs. α Six aspect ratios ($0.75 \leq AR \leq 2.00$) at $Re = 140,000$

Table A.2: Summary of Plots for Constant Wing Planform

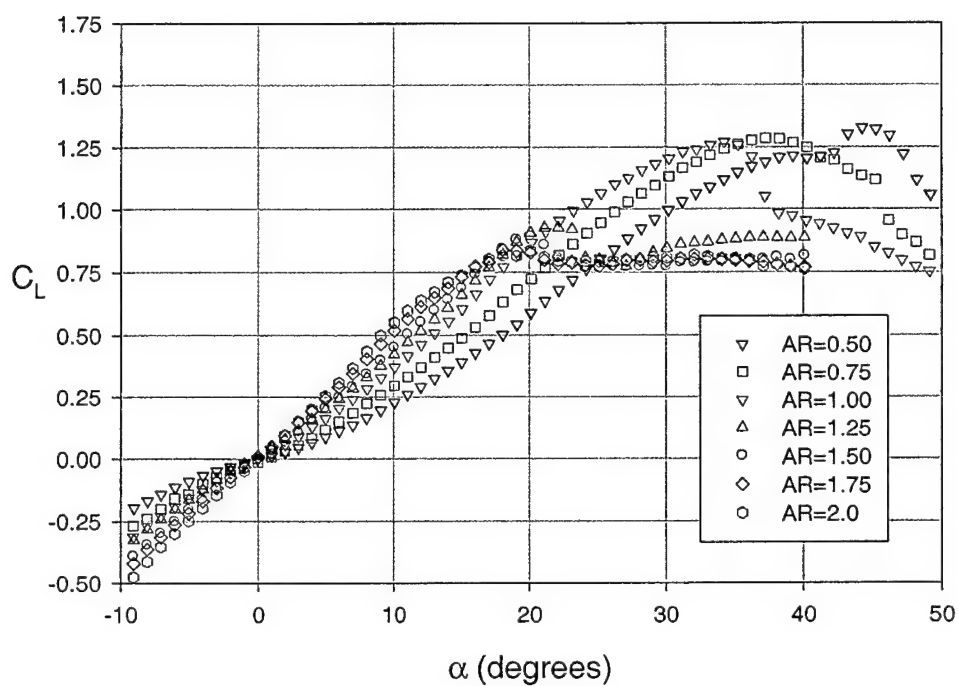


Figure A.41: C_L vs. α , rectangular planform, $Re_c = 100,000$

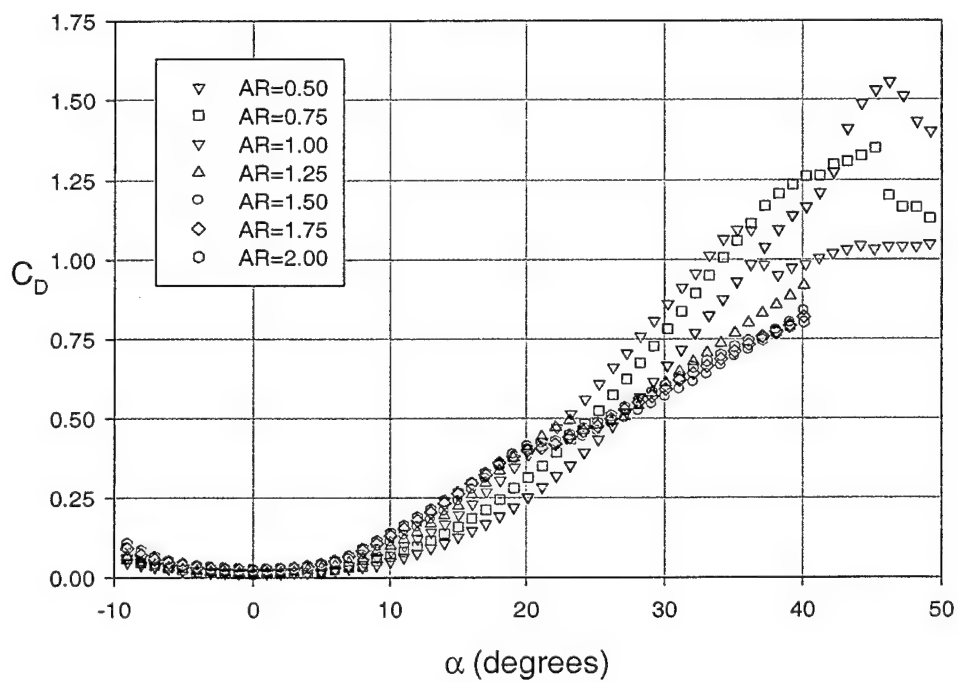


Figure A.42: C_D vs. α , rectangular planform, $Re_c = 100,000$

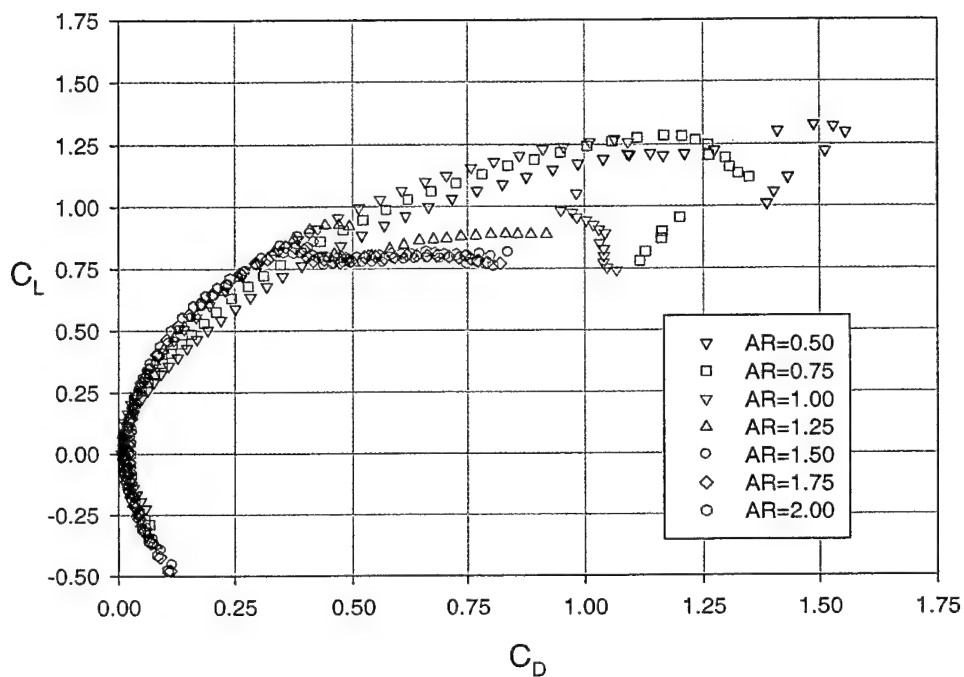


Figure A.43: C_L vs. C_D , rectangular planform, $Re_c = 100,000$

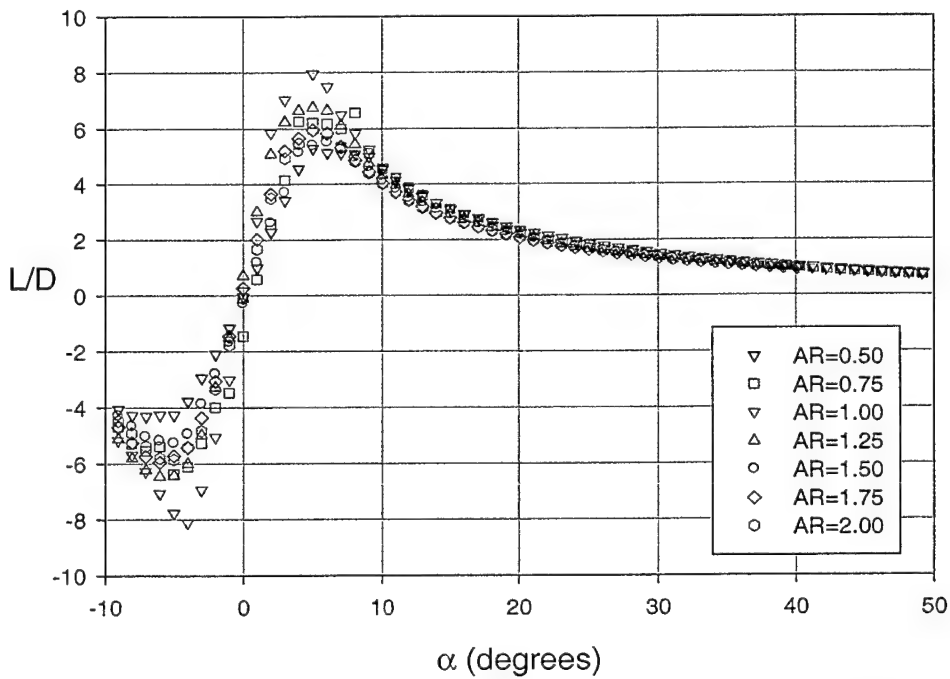


Figure A.44: L/D vs. α , rectangular planform, $Re_c = 100,000$

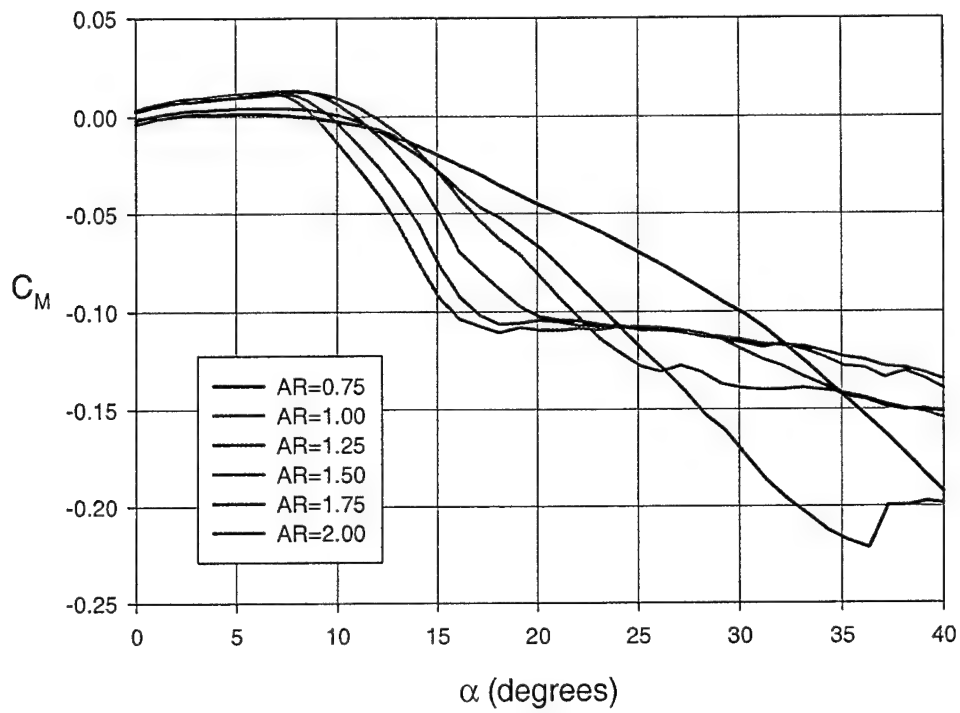


Figure A.45: C_M vs. α , rectangular planform, $Re_c = 140,000$

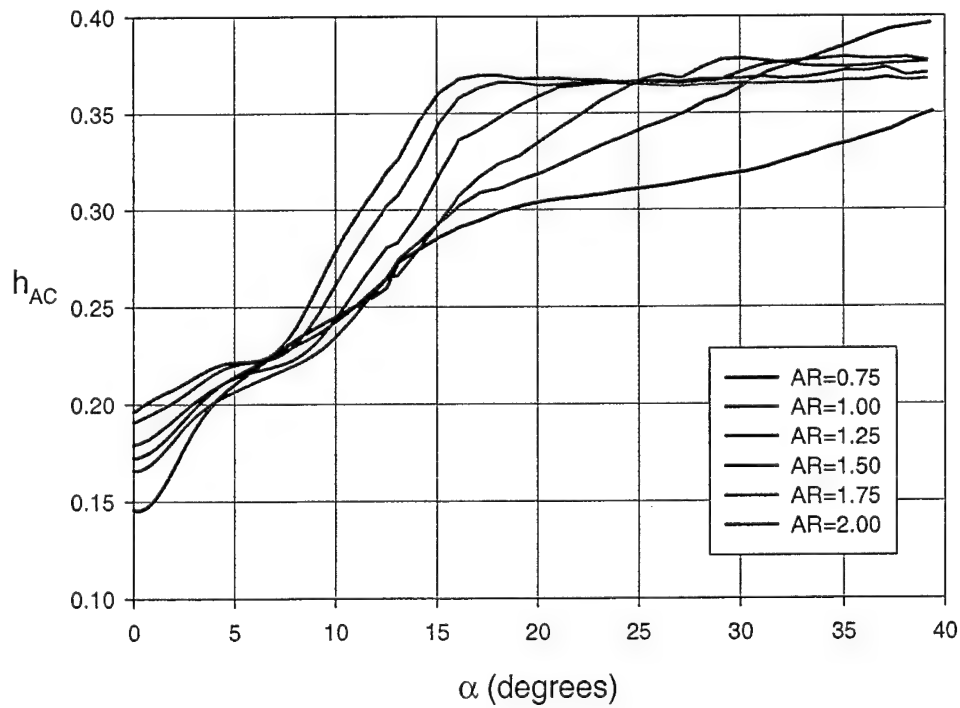


Figure A.46: h_{AC} vs. α , rectangular planform, $Re_c = 140,000$

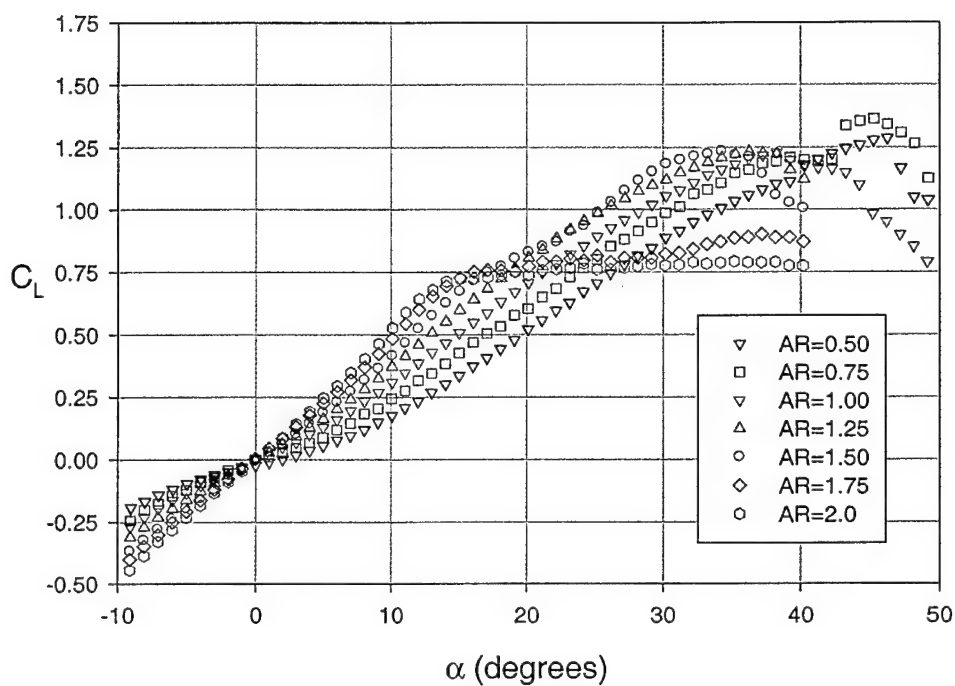


Figure A.47: C_L vs. α , Zimmerman planform, $Re_c = 100,000$

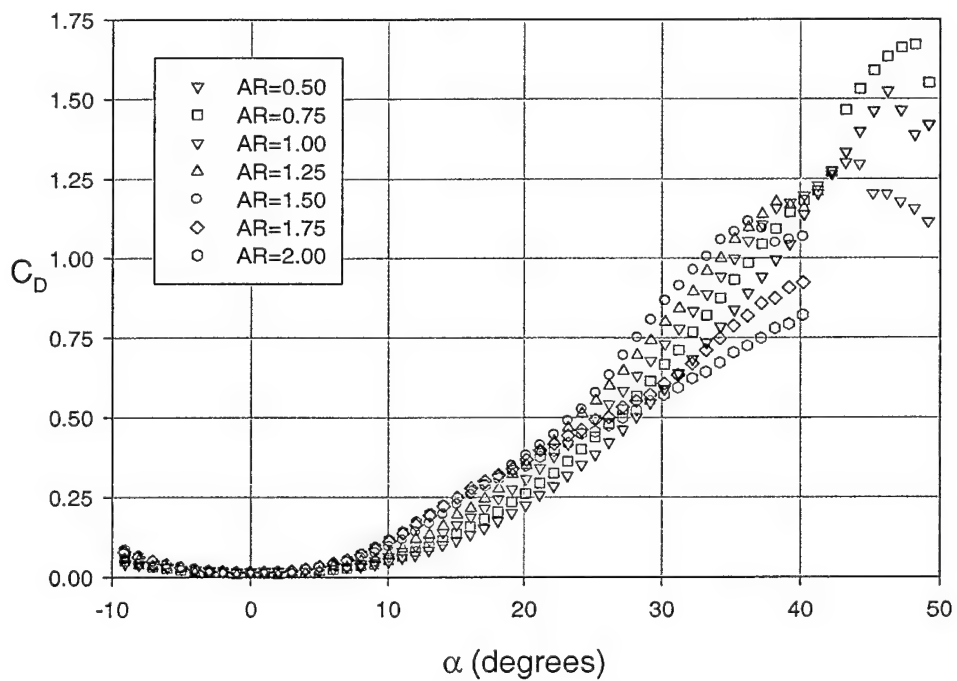


Figure A.48: C_D vs. α , Zimmerman planform, $Re_c = 100,000$

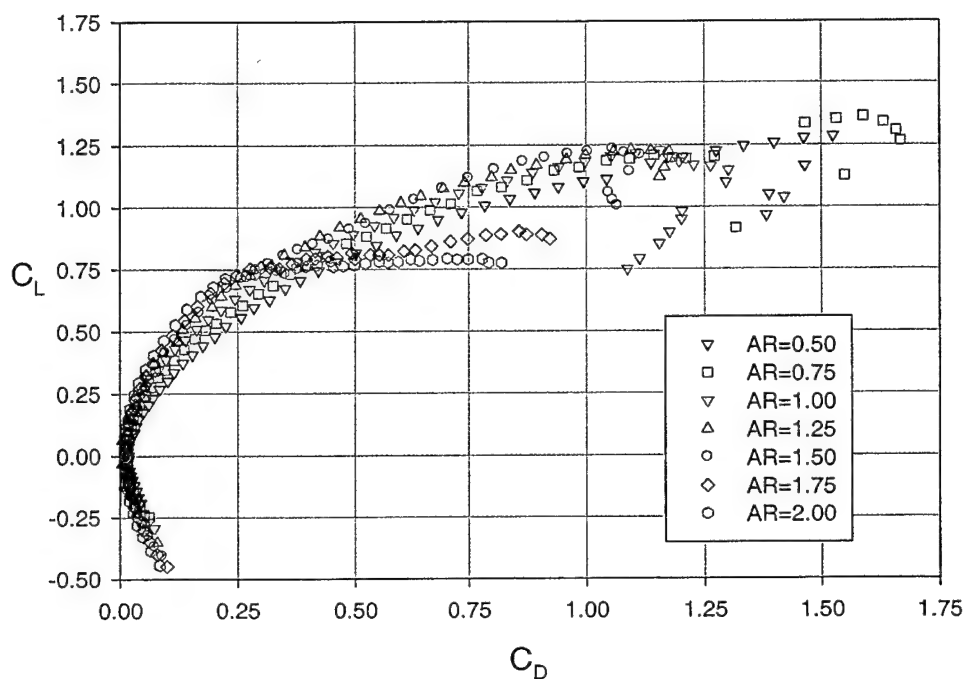


Figure A.49: C_L vs. C_D , Zimmerman planform, $Re_c = 100,000$

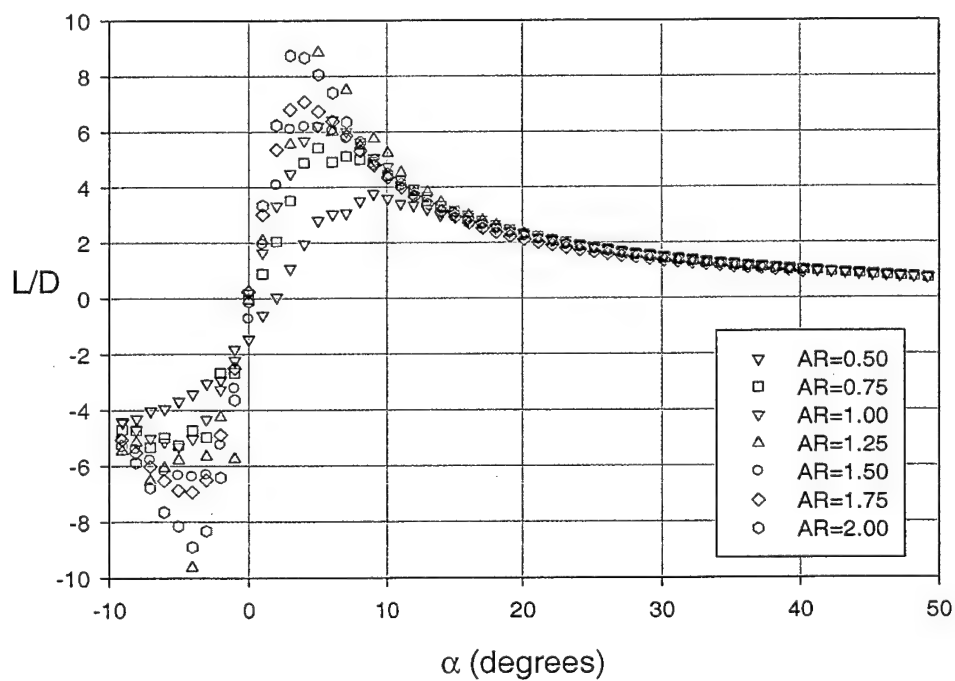


Figure A.50: L/D vs. α , Zimmerman planform, $Re_c = 100,000$

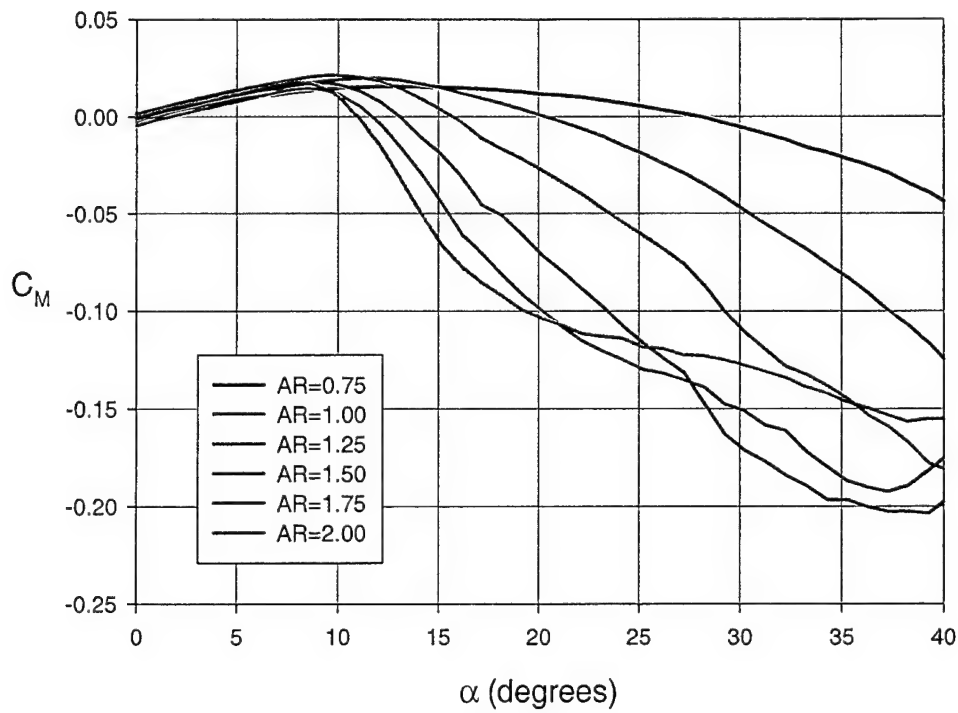


Figure A.51: C_M vs. α , Zimmerman planform, $Re_c = 140,000$

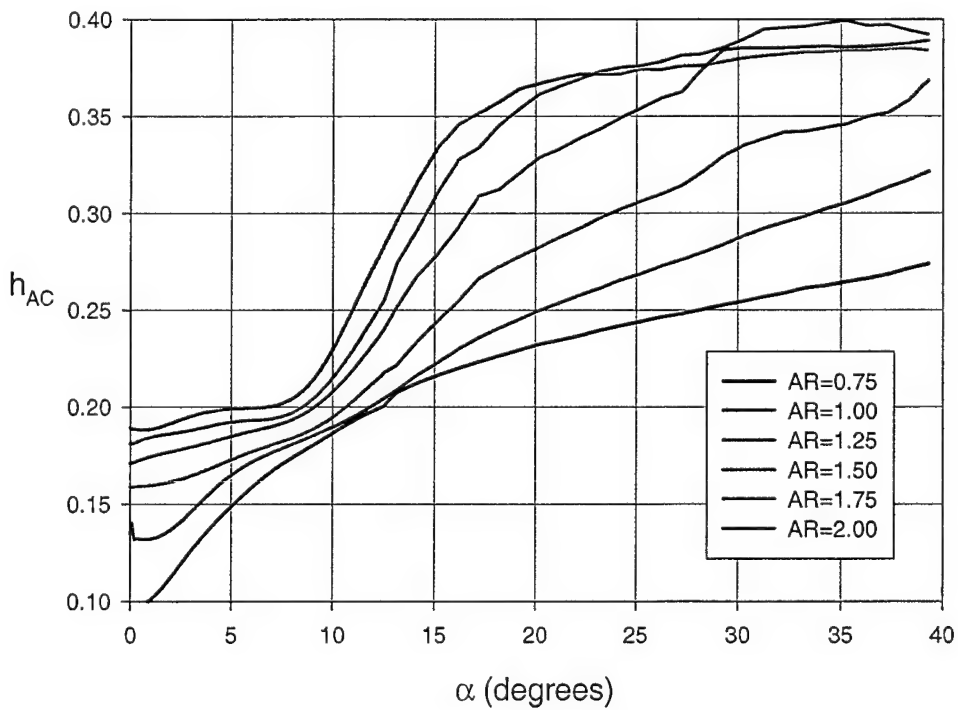


Figure A.52: h_{AC} vs. α , Zimmerman planform, $Re_c = 140,000$

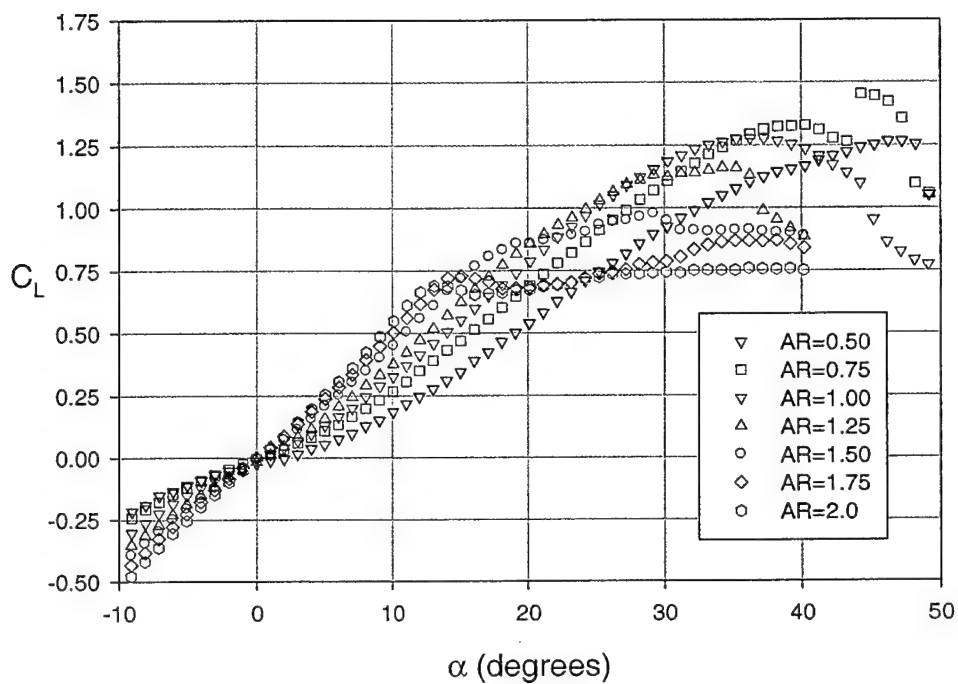


Figure A.53: C_L vs. α , inverse Zimmerman planform, $Re_c = 100,000$

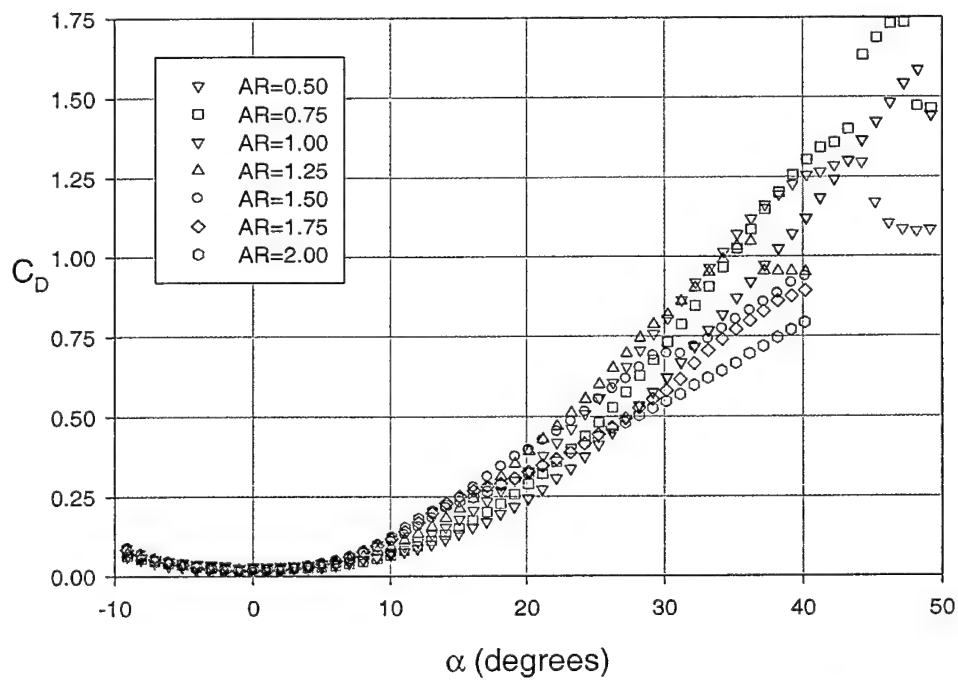


Figure A.54: C_D vs. α , inverse Zimmerman planform, $Re_c = 100,000$

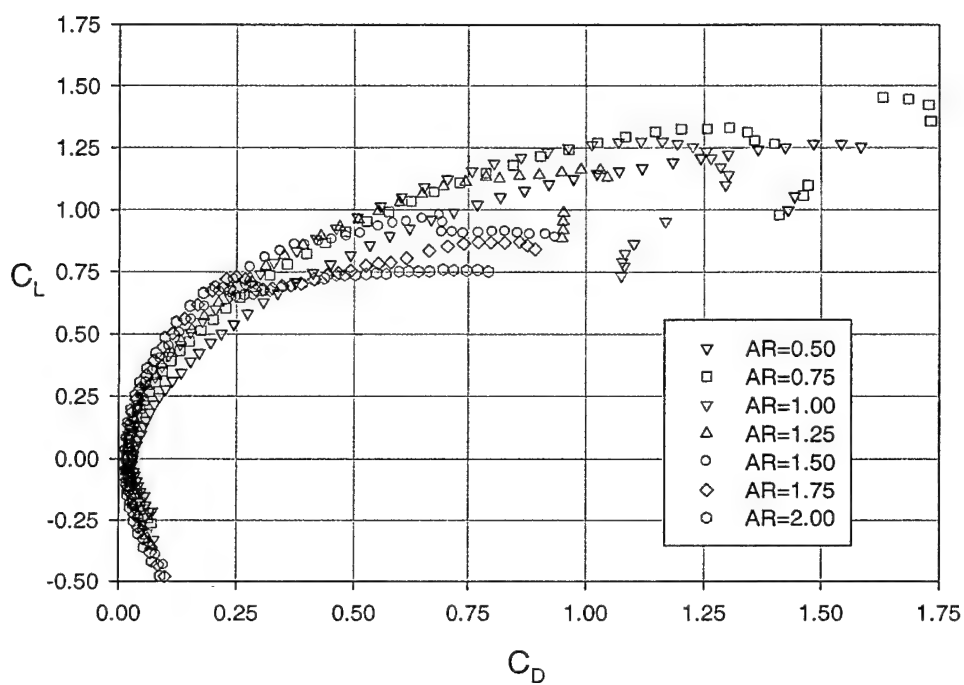


Figure A.55: C_L vs. C_D , inverse Zimmerman planform, $Re_c = 100,000$

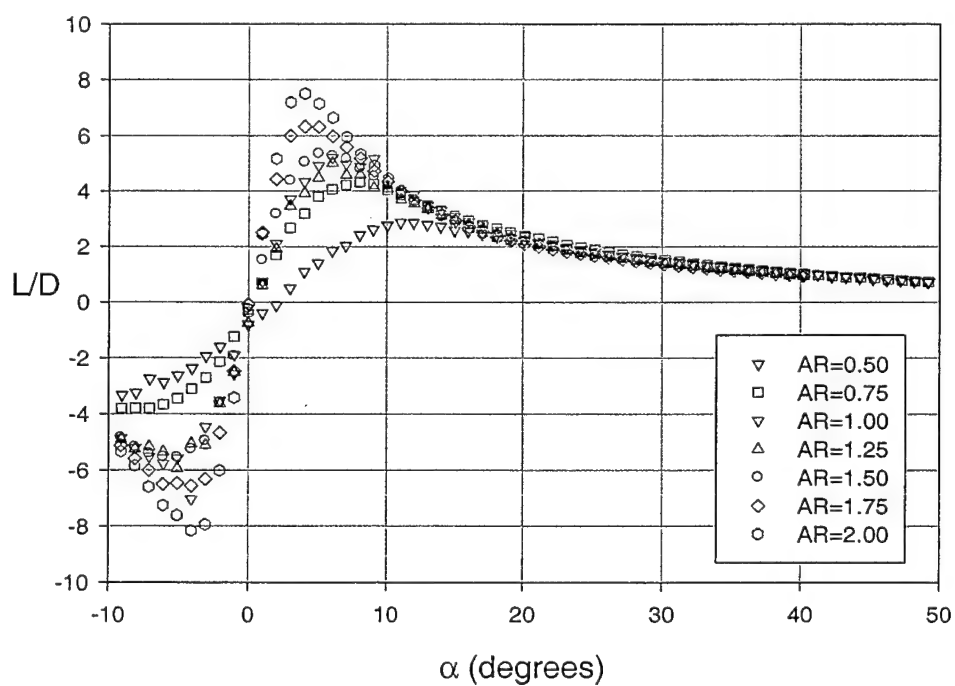


Figure A.56: L/D vs. α , inverse Zimmerman planform, $Re_c = 100,000$

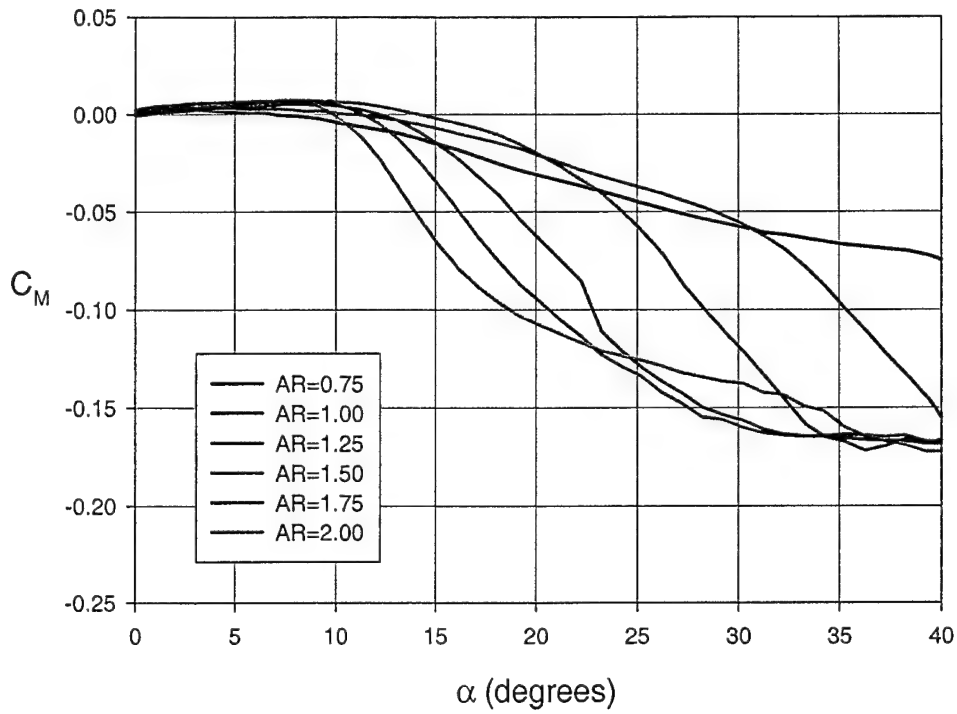


Figure A.57: C_M vs. α , inverse Zimmerman planform, $Re_c = 140,000$

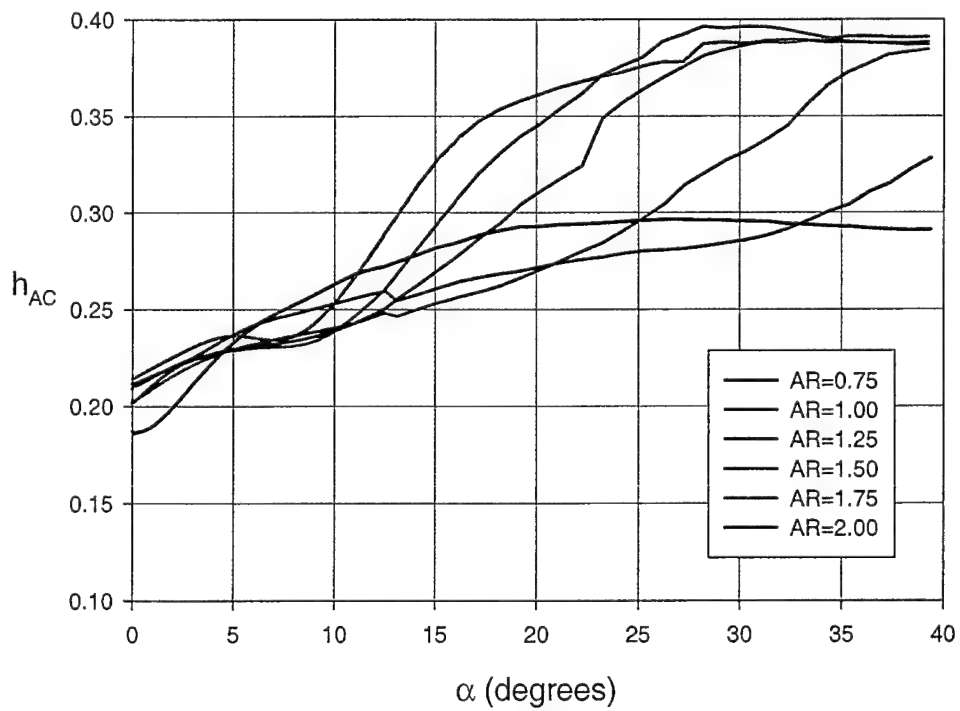


Figure A.58: h_{AC} vs. α , inverse Zimmerman planform, $Re_c = 140,000$

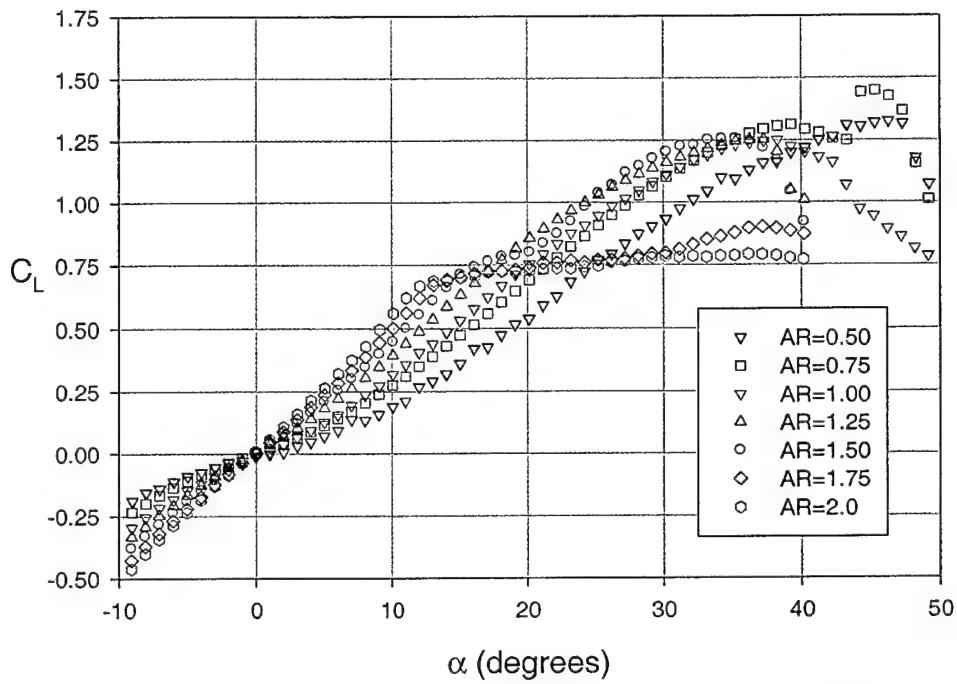


Figure A.59: C_L vs. α , elliptical planform, $Re_c = 100,000$

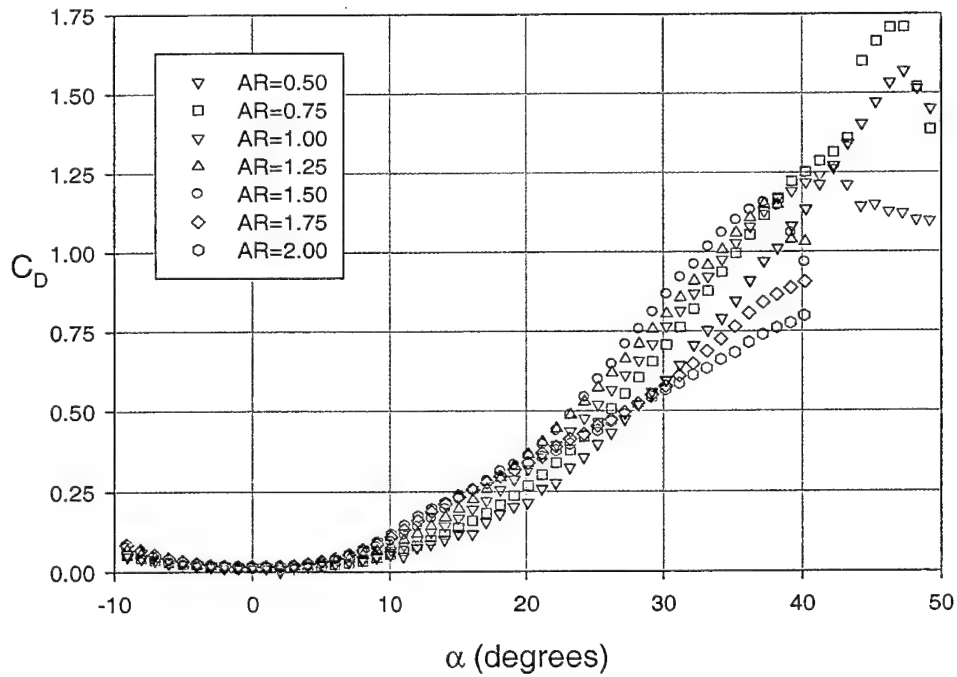


Figure A.60: C_D vs. α , elliptical planform, $Re_c = 100,000$

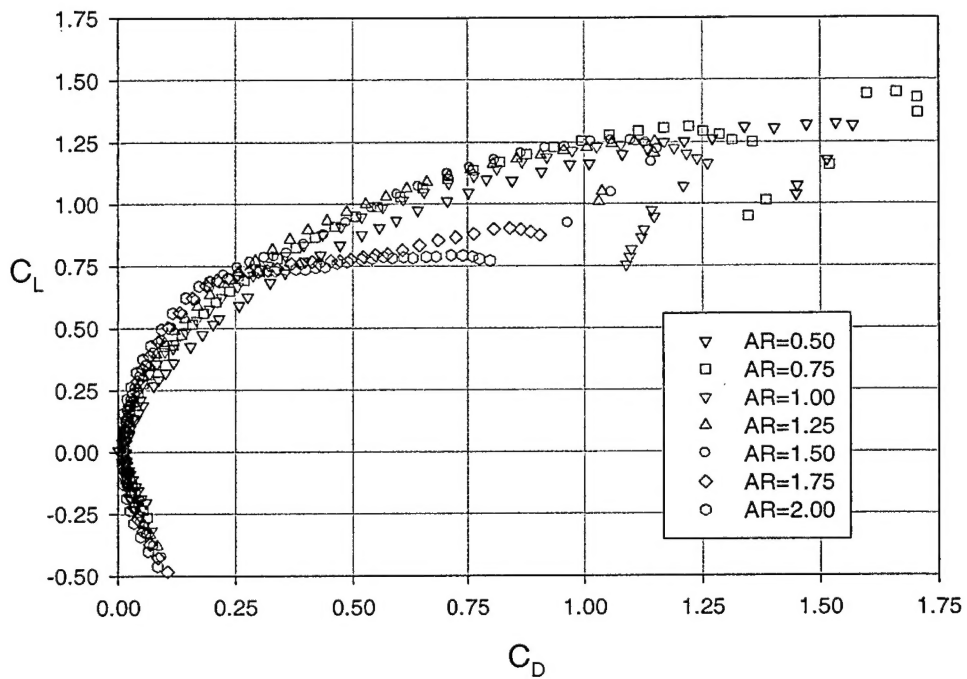


Figure A.61: C_L vs. C_D , elliptical planform, $Re_c = 100,000$

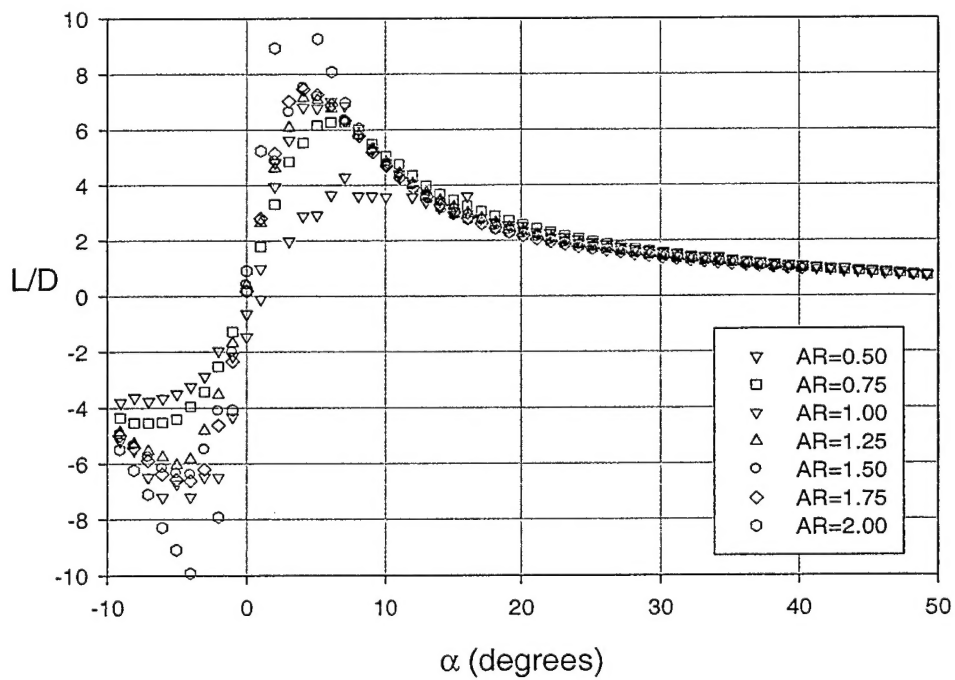


Figure A.62: L/D vs. α , elliptical planform, $Re_c = 100,000$

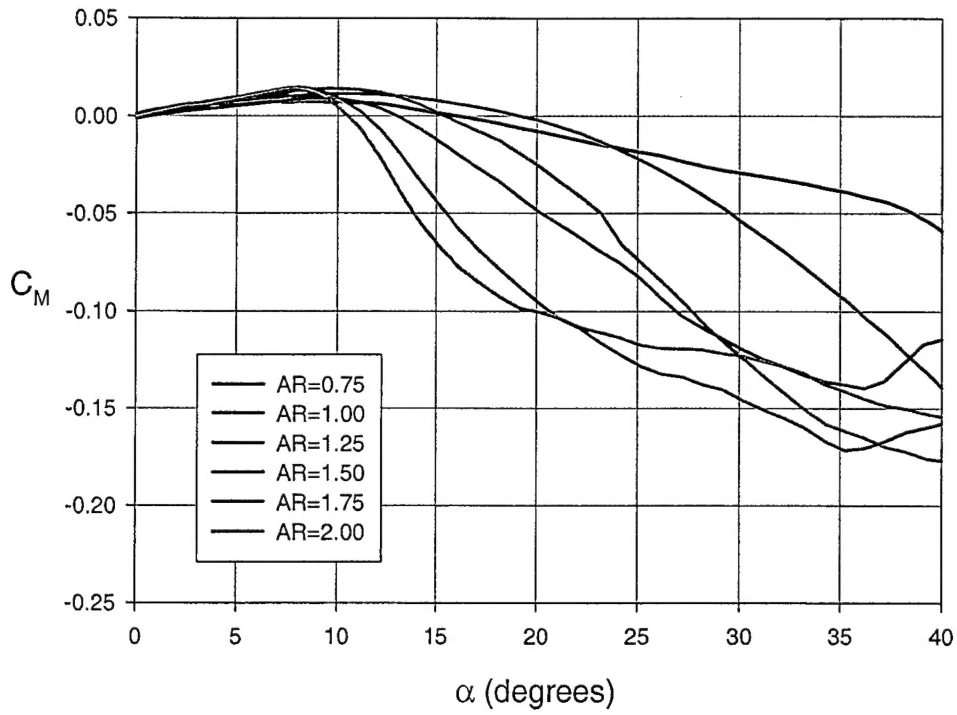


Figure A.63: C_M vs. α , elliptical planform, $Re_c = 140,000$

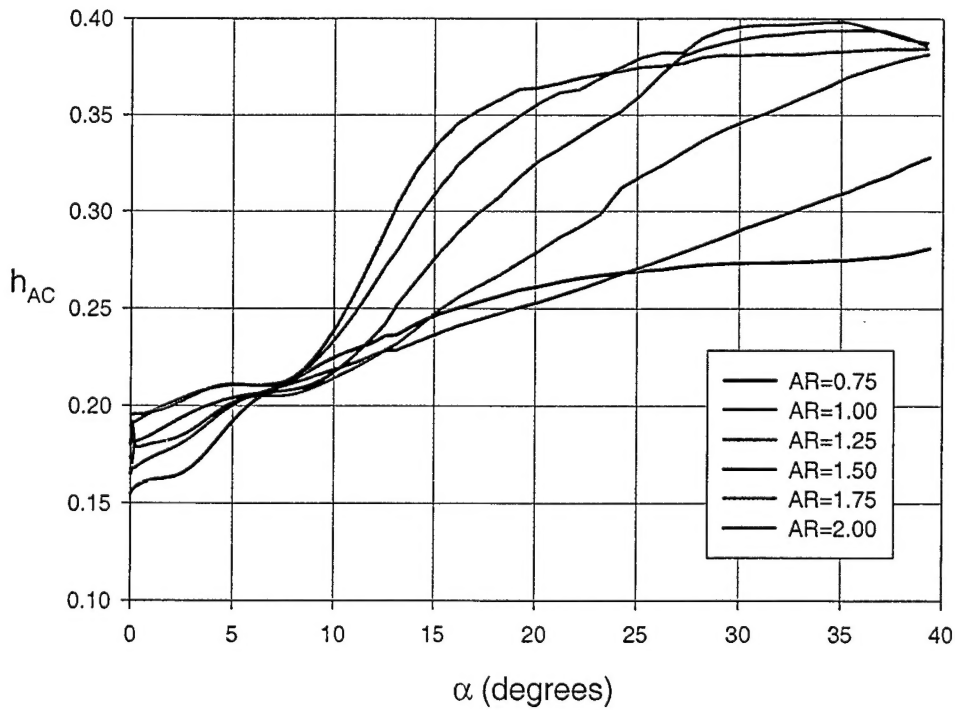


Figure A.64: h_{AC} vs. α , elliptical planform, $Re_c = 140,000$

Appendix B

Components

This section discusses the components chosen for the MAV design problem considered in this report. The components listed here are the smallest and lightest off-the-shelf components available at the time of this writing. In the dimension specifications that follow, the “length” is taken to be in the x direction, the “width” is taken to be in the y direction, and the “height” is taken to be in the z direction.

1. **Engine and Propeller:** The engine chosen for the MAV is a Cox glow engine with a displacement of 0.164 cubic centimeters (0.010 cubic inches). It uses a 7.62 *cm* (3 *in*) propeller. It runs at full throttle for the entire flight as it does not have a carburetor.

Dimensions	3.0 <i>cm</i> long x 1.5 <i>cm</i> wide x 3.5 <i>cm</i> high
Mass	13.6 grams
Center of Gravity	(0.50×length) <i>cm</i> from front edge

2. **Fuel Tank:** The fuel tank can hold a maximum of 6 cubic centimeters of fuel (9 grams of fuel). This allows the engine to run for approximately 10 minutes.

Dimensions	4.3 <i>cm</i> long x 1.7 <i>cm</i> wide x 1.7 <i>cm</i> high
Mass	11.0 grams
Center of Gravity	(0.50×length) <i>cm</i> from front edge

3. **Video Transmitter:** The video transmitter chosen is a 2.4 GHz FM transmitter with an output power of 80 mW. It is capable of transmitting a color video image up to two miles away.

Dimensions	5.5 <i>cm</i> long x 2.0 <i>cm</i> wide x 0.75 <i>cm</i> high
Mass	7.4 grams
Center of Gravity	(0.50×length) <i>cm</i> from front edge

4. **Video Camera:** The video camera is a color CMOS camera with a pinhole lens.

Dimensions	1.5 <i>cm</i> long x 2.3 <i>cm</i> wide x 1.5 <i>cm</i> high
Mass	7.0 grams
Center of Gravity	(0.50×length) <i>cm</i> from front edge

5. **Radio Control Receiver:** The RC receiver is a micro 6-channel receiver (FMA Extreme).

Dimensions	4.7 <i>cm</i> long x 2.3 <i>cm</i> wide x 1.5 <i>cm</i> high
Mass	10.6 grams
Center of Gravity	(0.50×length) <i>cm</i> from front edge

6. **Radio Control Servos:** The servos are sub-micro servos (Hitec HS-50).

Dimensions	2.0 <i>cm</i> long x 1.2 <i>cm</i> wide x 2.5 <i>cm</i> high
Mass	5.6 grams
Center of Gravity	(0.50×length) <i>cm</i> from front edge

7. **Batteries:** The batteries power both the video equipment and the radio control equipment. Two lithium cells are used wired in series. They have a capacity of 300 mAh and could run the electronics in the MAV for a duration of approximately 30 minutes.

Dimensions	3.0 <i>cm</i> long x 0.5 <i>cm</i> wide x 2.5 <i>cm</i> high
Mass	7.5 grams each
Center of Gravity	(0.50×length) <i>cm</i> from front edge